NORTHWESTERN UNIVERSITY

Dominance and Spatiotemporal Behavior in Cyclic Ecological Systems

A DISSERTATION

SUBMITTED TO THE GRADUATE SCHOOL

IN PARTIAL FULFILLMENT OF THE REQUIREMENTS

for the degree

DOCTOR OF PHILOSOPHY

Field of Applied Mathematics

By

Thomas Isaac Stiadle

EVANSTON, ILLINOIS

December 2022

ABSTRACT

Dominance and Spatiotemporal Behavior in Cyclic Ecological Systems

Thomas Isaac Stiadle

Deterministic models are used to explain and predict the dynamics of ecosystems featuring cyclic competition schemes. The models are systems of reaction-diffusion partial differential equations that account for species mobility via Fickian diffusion and interspecies interactions according to the competition scheme. Length and temporal scales are chosen to be appropriate for an experimental bacterial community, qualitatively modeling observed *E. coli* bacterial systems, and behaviors reported from relevant experiments are reproduced by the models. Systems of two, three, and four species are examined and it is shown that direct interspecies competition, mobility, and initial spatial structure are relevant factors in the determination of the dominant species and long-term dynamics of cyclic systems. One- and two-dimensional domains are considered, modeling a community confined to a thin annulus and a petri dish, respectively.

For three-species symmetric systems, when coexistence of all three species is unstable and interspecies competition is relatively weak, spatiotemporal chaotic behavior generally occurs. A mechanism for the development of chaos, patch splitting, is proposed. On the

other hand, when interspecies competition is sufficiently strong, ordered patterns are often found. In 1D, traveling arrays of single-species patches, as well as modulated traveling waves, consisting of patches which periodically expand and contract (breather modes), can be found. In 2D, spirals, as well as localized patches that chase each other, can occur. In three-species asymmetric systems, the "survival of the weakest" phenomenon is often reproduced by the model.

In three- and four-species systems with an exceptionally strong or weak competitor, behavior is dominated by transcritical bifurcations between (i) the coexistence state and (ii) partial alliance states involving competing species. Although the three- and four-species models admit very different solutions when all species are strong competitors, these transcritical bifurcations unify the behavior of the two systems in the case of a strong or weak exceptional species. The displacement of one state by another is discussed in the context of an invasion. For the displacement of unstable states, speeds of displacement are computed and compared to analytical estimates for pulled fronts. Finally, it is shown that for a one-dimensional three-species system involving a species that is less mobile than the others, the dynamics of the system become more complicated as the mobility of the exceptional species decreases.

Acknowledgements

I am grateful to the Department of Engineering Sciences and Applied Mathematics and Northwestern University for giving me the opportunity to learn, teach, and contribute. I personally thank Professors Alvin Bayliss and Vladimir Volpert for their time, effort, and support. They have both gone above and beyond anything I could have asked for in an advisor. Thank you also to Prof. Chopp for agreeing to serve on my committee and keeping the department running smoothly since I got here.

Finally, thank you to my friends and colleagues who weathered the storm with me, especially Jithin George, Julie Nguyen, and April Zhou.

Dedication

To B.A.D., P.R.D., B.I.S., B.L.S., K.E.S., K.S.S., L.A.S., C.T., and V.T.

Table of Contents

List of Tables

List of Figures

CHAPTER 1

Introduction

Cyclic competition networks are considered to be important contributors to natural biodiversity [**1**]. The term "cyclic competition" refers to a scheme by which N species u_i, where $1 \leq i \leq N$, compete such that u_2 has a competitive advantage over u_1, u_3 has an advantage over u_2, and so on, with u_N having an advantage over u_1 to complete the cycle. Thus, each species wins exactly one competition and loses exactly one competition. In ecological communities governed by such a scheme, there is no a-priori winner (unlike in a transitive system, where, say, the advantages of u_3 over u_2 and u_2 over u_1 would imply that u_3 has an advantage over u_1). Cyclic competition schemes with three species are sometimes referred to as "rock-paper-scissors" (RPS) schemes, due to the obvious analogy with the classic game. Ecosystems governed by these schemes (cyclic ecosystems) have been observed naturally and experimentally, though detailed observations of the population dynamics are difficult.

Cyclic ecosystems can be modeled by systems of reaction-diffusion partial differential equations (PDEs). These systems, though relatively straightforward to write down, can give rise to a variety of complex spatiotemporal behaviors. Studying these models analytically and numerically can give insight to the mechanisms driving the dynamics of physical ecosystems. Indeed, some behaviors predicted by such models have been directly observed in real ecosystems, while others may be helpful in inferring dynamics that have not yet been observed.

CHAPTER 2

Background

2.1. Ecological Literature

2.1.1. *E. Coli* Ecosystems

Escherichia coli (*E. coli*) is a bacterial species commonly found in the intestines of warm-blooded animals. Its availability, simplicity, and rapid growth rate make it an excellent candidate for ecological and biochemical research [**2**]. Natural or artificial variants of these bacteria can form cyclically competitive ecosystems, and such systems have been observed in laboratory settings.

One such ecosystem is formed among toxin-producing, toxin-resistant, and toxin-sensitive variants. In particular, colicinogenic *E. coli* produce the toxin colicin, which is released via stress-induced cell lysis. These bacteria are also immune to colicin. Bacteria that are not colicinogenic are generally killed by colicin, though certain mutations (commonly those that inhibit the ability of the cell membrane to bind the toxin) grant resistance. Calling the colicinogenic variant C, the sensitive variant S, and the resistant variant R, C has a competitive advantage over S (since C kills S), S has a competitive advantage over R (since S has an advantage in nutrient uptake, due to R having an altered protein in its cell membrane), and R has a competitive advantage over C (since C pays an energy cost in synthesizing the toxin and also kills itself upon releasing it) [**3, 4**]. Thus,

C "wins" over S, S wins over R, and R wins over C, such that the ecosystem exhibits a rock-paper-scissors competition scheme.

In [**3**], liquid suspensions of the three variants were prepared and maintained in a flask such that the environment within the flask was essentially spatially homogeneous. The abundance of each strain was determined approximately once per day. It was found that C quickly killed off S and was subsequently driven to extinction by R, so that at the end of the week, only R remained in the flask. Thus, the three variants were not able to coexist; rather, one variant was selected over the others. On the other hand, when single-variant patches were placed randomly on an agar plate (so that the environment was not spatially homogeneous), the patches were observed chasing each other (C chased S, S chased R, and R chased C). Over the observation period, no variant was driven to extinction and, in fact, the abundance of each variant remained relatively unchanged. Therefore, in this case, diversity was maintained, even though the three species were not observed coexisting in any localized region of the plate. In [**5**], similar experiments were conducted, with the variants initially placed at the center of the plate and the growth rates of the variants genetically controlled, so that expansion of the territory occupied by each of the variants could be studied. For these experiments, transient coexistence of the C and R variants was reported.

In [**4**], mice were orally inoculated with one of the three variants and the bacteria were allowed to colonize over a four-week period. Following this, the mice were permitted to interact with each other and the bacterial populations present in each mouse were monitored over twelve weeks. It was found that C tended to displace S, R displaced C, and S displaced R, as hypothesized. Moreover, each mouse was nearly always dominated by a

singular variant at any given time; mixed populations were rarely seen. For each mouse, the identity of the dominant variant changed several times throughout the experiment.

In [**6**], three strains of *E. coli* were engineered such that each strain was able to synthesize a unique toxin. Each strain was immune to its own toxin. Each strain also received immunity to one of the other toxins, so that it controlled exactly one strain and was controlled by the other strain, forming a cyclic ecosystem. The strains were added to culture medium and the abundance of each strain was determined periodically. Fresh cells were occasionally introduced to limit the effect of mutations on the system dynamics. Similarly to the observations in [**4**], it was found that the strains took turns dominating the culture, with each strain taken over by its controlling strain.

2.1.2. Other Ecosystems

Cyclic competition schemes can be found in non-bacterial ecosystems as well. In [**7**], male reproductive strategies among side-blotched lizards are analyzed. Males with orange throats (variant O) take an aggressive approach, preferring to defend large territories. Those with blue throats (variant B) are less aggressive and generally choose to defend small territories. Finally, those with yellow throats (variant Y) do not defend territories at all and, in fact, look very similar to female side-blotched lizards. A population of these lizards was observed over a period of six years. The identity of the dominant variant changed three times over the observation period, with O replacing B, Y replacing O, and B replacing Y, indicating, for example, that the aggressive strategy of O was effective over the less aggressive strategy of B, but not over the alternative strategy of Y (similar statements can be made for the other strategies). Populations of side-blotched lizards can

thus be considered cyclic ecosystems, with changes in dominance analogous to those seen in cyclic bacterial ecosystems.

Finally, cyclic competition has been observed among aquatic invertebrates [**8**] and grasses [**9, 10**], with several of these ecosystems consisting of more than three species.

2.2. Model Development

For an ecosystem containing only a single species U, the logistic equation,

$$\frac{du}{dt} = \frac{ru(M-u)}{M}, \tag{2.1}$$

may be used to model the population $u \geq 0$ of the species, where M is the carrying capacity of the species (i.e., the maximum population that can be supported by the ecosystem) and r is its natural birthrate (the reciprocal of the doubling time). It is clear that the equation has two fixed points: $u = 0$ (linearly unstable) and $u = M$ (linearly stable). Thus, as $t \to \infty$, $u \to M$, so the model predicts that, in the absence of external competition, a species will approach its carrying capacity over time, rather than go extinct, provided u is initally nonzero. For completeness, the general solution to (2.1) is

$$u(t) = \frac{M}{Ce^{-rt}+1}, \tag{2.2}$$

where C is a constant determined by the population u_0 at time $t = 0$ (specifically, $C = \frac{M}{u0} - 1$, assuming $u_0 > 0$).

Suppose now that the ecosystem contains two species, U_1 and U_2, with U_1 competing for resources with U_2. The populations of the species (u_1 and u_2, respectively) can be

modeled by a natural extension of the logistic equation (2.1); namely,

$$\frac{du_1}{dt} = \frac{r_1 u_1 (M_1 - u_1 - \alpha_{1,2} u_2)}{M_1}, \tag{2.3a}$$

$$\frac{du_2}{dt} = \frac{r_2 u_2 (M_2 - u_2 - \alpha_{2,1} u_1)}{M_2}, \tag{2.3b}$$

where $\alpha_{1,2}, \alpha_{2,1} \geq 0$ are interaction parameters quantifying the effects of interspecies competition. In keeping with the logistic equation, the fixed point $(u_1, u_2) = (0, 0)$ is unstable for all physical choices of the interaction parameters, so that extinction of both species will not occur, provided at least one of the initial populations is nonzero. The relationship between U_1 and U_2 is purely competitive; that is, the presence of U_1 does not benefit U_2, and vice versa. This is in contrast to the Lotka-Volterra predator-prey model, where the presence of, say, U_1 benefits U_2, while the presence of U_2 adversely affects U_1 (i.e., U_2 is a predator of U_1).

System (2.3) can be made spatially explicit by introducing the spatial variable x, with $-L \leq x \leq L$. This allows for incorporation of species motility, modeled as Fickian diffusion, resulting in the system

$$\frac{\partial u_1}{\partial t} = d_1 \frac{\partial^2 u_1}{\partial x^2} + \frac{r_1 u_1 (M_1 - u_1 - \alpha_{1,2} u_2)}{M_1}, \tag{2.4a}$$

$$\frac{\partial u_2}{\partial t} = d_2 \frac{\partial^2 u_2}{\partial x^2} + \frac{r_2 u_2 (M_2 - u_2 - \alpha_{2,1} u_1)}{M_2} \tag{2.4b}$$

on the domain $[-L, L]$, where $d_1, d_2 \geq 0$ are diffusivities (quantifying the capability of the species to spread with units of area over time). Introducing a second spatial variable y,

with $-L \leq y \leq L$, gives the 2D system

$$\frac{\partial u_1}{\partial t} = d_1 \left(\frac{\partial^2 u_1}{\partial x^2} + \frac{\partial^2 u_1}{\partial y^2} \right) + \frac{r_1 u_1 (M_1 - u_1 - \alpha_{1,2} u_2)}{M_1}, \tag{2.5a}$$

$$\frac{\partial u_2}{\partial t} = d_2 \left(\frac{\partial^2 u_2}{\partial x^2} + \frac{\partial^2 u_2}{\partial y^2} \right) + \frac{r_2 u_2 (M_2 - u_2 - \alpha_{2,1} u_1)}{M_2} \tag{2.5b}$$

on the square domain $[-L, L] \times [-L, L]$. This system can be nondimensionalized by taking

$$\tilde{t} = \frac{t}{t_{ref}}, \quad \tilde{x} = \frac{x}{x_{ref}}, \quad \tilde{y} = \frac{y}{y_{ref}}, \quad \tilde{u}_1 = \frac{u_1}{u_{1_{ref}}}, \quad \tilde{u}_2 = \frac{u_2}{u_{2_{ref}}}, \tag{2.6}$$

where t_{ref}, x_{ref}, y_{ref}, $u_{1_{ref}}$, and $u_{2_{ref}}$ are reference quantities. Plugging these into the system and rearranging yields

$$\frac{\partial \tilde{u}_1}{\partial \tilde{t}} = d_1 \left(\frac{t_{ref}}{x_{ref}^2} \frac{\partial^2 \tilde{u}_1}{\partial \tilde{x}^2} + \frac{t_{ref}}{y_{ref}^2} \frac{\partial^2 \tilde{u}_1}{\partial \tilde{y}^2} \right) + t_{ref} r_1 \tilde{u}_1 \left(1 - \frac{u_{1_{ref}} \tilde{u}_1}{M_1} - \frac{\alpha_{1,2} u_{2_{ref}} \tilde{u}_2}{M_1} \right), \tag{2.7a}$$

$$\frac{\partial \tilde{u}_2}{\partial \tilde{t}} = d_2 \left(\frac{t_{ref}}{x_{ref}^2} \frac{\partial^2 \tilde{u}_2}{\partial \tilde{x}^2} + \frac{t_{ref}}{y_{ref}^2} \frac{\partial^2 \tilde{u}_2}{\partial \tilde{y}^2} \right) + t_{ref} r_2 \tilde{u}_2 \left(1 - \frac{u_{2_{ref}} \tilde{u}_2}{M_2} - \frac{\alpha_{2,1} u_{1_{ref}} \tilde{u}_1}{M_2} \right). \tag{2.7b}$$

Setting

$$\begin{aligned} &t_{ref} = \frac{1}{r_1}, \quad x_{ref} = y_{ref} = \sqrt{\frac{d_1}{r_1}}, \quad u_{1_{ref}} = M_1, \quad u_{2_{ref}} = M_2, \\ &\tilde{d} = \frac{d_2}{d_1}, \quad K = \frac{r_2}{r_1}, \quad \tilde{\alpha}_{1,2} = \frac{\alpha_{1,2} M_2}{M_1}, \quad \tilde{\alpha}_{2,1} = \frac{\alpha_{2,1} M_1}{M_2}, \end{aligned} \tag{2.8}$$

leads to the nondimensional system

$$\frac{\partial \tilde{u}_1}{\partial \tilde{t}} = \nabla^2 \tilde{u}_1 + \tilde{u}_1 (1 - \tilde{u}_1 - \tilde{\alpha}_{1,2} \tilde{u}_2), \tag{2.9a}$$

$$\frac{\partial \tilde{u}_2}{\partial \tilde{t}} = \tilde{d} \nabla^2 \tilde{u}_2 + K \tilde{u}_2 (1 - \tilde{u}_2 - \tilde{\alpha}_{2,1} \tilde{u}_1) \tag{2.9b}$$

on the domain $[\tilde{L}, \tilde{L}]$ (for a 1D problem; the nondimesionalization of (2.4) clearly also leads to (2.9)) or $[-\tilde{L}, \tilde{L}] \times [-\tilde{L}, \tilde{L}]$ (2D), where ∇^2 is the Laplacian and

$$\tilde{L} = \frac{L}{x_{ref}} = L\sqrt{\frac{r_1}{d_1}}. \tag{2.10}$$

Nondimensionalized systems will be considered from this point forward, and the tildes will be dropped from all symbols.

Ecosystems with N species can be modeled by the generalized form of (2.9):

$$\frac{\partial u_1}{\partial t} = \nabla^2 u_1 + u_1(1 - u_1 - \alpha_{1,2}u_2 - \alpha_{1,3}u_3 - \cdots - \alpha_{1,N}u_N), \tag{2.11a}$$

$$\frac{\partial u_2}{\partial t} = d_2\nabla^2 u_2 + K_2 u_2(1 - u_2 - \alpha_{2,1}u_1 - \alpha_{2,3}u_3 - \cdots - \alpha_{2,N}u_N), \tag{2.11b}$$

$$\vdots$$

$$\frac{\partial u_N}{\partial t} = d_N\nabla^2 u_N + K_N u_N(1 - u_N - \alpha_{N,1}u_1 - \alpha_{N,2}u_2 - \cdots - \alpha_{N,N-1}u_{N-1}). \tag{2.11c}$$

If $N = 3$ and $K_2 = K_3 = 1$, then the May-Leonard model with diffusion is recovered (the original May-Leonard model [**11**] is a system of ordinary differential equations; i.e., there is no spatial dependence).

Since the present interest is in purely cyclic interspecies competition, as described in the ecological literature discussed in Section 2.1, the model is modified to enforce the criteria that each species (i) controls exactly one species and (ii) is controlled by exactly one species. It is also assumed that the natural birthrates of the species are the same. This is accomplished by setting $\alpha_{i,j} = 0$ for $j \neq (i \bmod N) + 1$ and $K_i = 1$ for $2 \leq i \leq N$:

$$\frac{\partial u_1}{\partial t} = \nabla^2 u_1 + u_1(1 - u_1 - \alpha_1 u_2), \tag{2.12a}$$

$$\frac{\partial u_2}{\partial t} = d_2 \nabla^2 u_2 + u_2(1 - u_2 - \alpha_2 u_3), \tag{2.12b}$$

$$\vdots$$

$$\frac{\partial u_N}{\partial t} = d_N \nabla^2 u_N + u_N(1 - u_N - \alpha_N u_1), \tag{2.12c}$$

where $\alpha_1 = \alpha_{1,2}$, $\alpha_2 = \alpha_{2,3}$, and $\alpha_N = \alpha_{N,1}$. For this system, it is straightforward to show that extinction of all species is linearly unstable, as was the case for Equation (2.1) and System (2.3).

2.2.1. Parameter Selection

One of the primary objectives in deriving (2.12) was to develop an appropriate model for cyclic ecosystems consisting of variants of *E. coli*, as previously discussed. When a model of such a system is desired, the domain half-length L must be chosen such that it reflects the properties of both *E. coli* and the physical domain. Recalling the relationship (2.10), the nondimensional half-length depends on the size of the physical domain, as well as the birthrate and diffusivity of the species U_1. For reference, the doubling time of *E. coli* is approximately 20 minutes in a laboratory setting (corresponding to a birthrate of $\frac{1}{1200}$ s^{-1}) [**12**] and the diffusivity of wild-type *E. coli* in liquid media is roughly 5×10^{-6} cm^2/s [**13**] (though differences in cell concentration can have marked effects on this parameter [**14**]). In agar, the diffusivity is decreased by a factor of about 30, subject to the concentration of the agar [**15**].

When considering an ecosystem confined to the walls of a petri dish, the domain can be thought of as a thin annulus and, provided this annulus is sufficiently thin, the system can be approximately described by the 1D model. In this case, the relevant physical half-length is half the circumference of the petri dish. Given that a typical petri dish has a diameter between 3 and 20 cm (so that half the circumference ranges from 1.5π to 10π cm), it is easy to see from (2.10) that the model domain's half-length should be between 60 and 410, provided the modeled system is a liquid suspension. If the *E. coli* are in agar instead (as in, e.g., [**3**]), the range should be multiplied by a factor of approximately 5.5 (i.e., the range should be roughly 330 to 2255).

If the species are allowed to spread across the entire petri dish, a two-dimensional domain is necessary. Although many (but not all) petri dishes are circular, the shape of the model domain need not be circular. If a square model domain is used, solutions near the boundary may be distorted, but this generally does not have an effect on the qualitative nature of the solution. For this reason, the domain $[-L, L] \times [-L, L]$ will be used for 2D models, as described above. Taking the radius of the petri dish as the relevant physical half-length gives a model half-length between 20 and 130 for a liquid suspension, with the range again multiplied by about 5.5 in the case of an agar environment.

CHAPTER 3

Fixed Points and Stability

3.1. Two Species

System (2.12) with two species can be written as

$$\frac{\partial u}{\partial t} = \nabla^2 u + u(1 - u - \alpha v), \tag{3.1a}$$

$$\frac{\partial v}{\partial t} = d_v \nabla^2 v + v(1 - v - \beta u). \tag{3.1b}$$

The associated ordinary differential equation (ODE) system is

$$\frac{du}{dt} = u(1 - u - \alpha v), \tag{3.2a}$$

$$\frac{dv}{dt} = v(1 - v - \beta u). \tag{3.2b}$$

The physicality and stability of the fixed points of the ODE system are unchanged by the introduction of diffusive terms (see, e.g., [**16**]); thus, the fixed points will be discussed in the context of the ODE system. This will also be the case for the three- and four-species systems discussed below. Clearly, System (3.2) has four fixed points (u, v):

- Extinction state $b_0 = (0, 0)$
- Single-species states $b_u = (1, 0)$ and $b_v = (0, 1)$
- Coexistence state $b_{uv} = (u_*, v_*)$

The components of the coexistence state satisfy the system of equations

$$u_* + \alpha v_* = 1, \tag{3.3a}$$

$$v_* + \beta u_* = 1, \tag{3.3b}$$

which, assuming $\alpha\beta \neq 1$, has the unique solution

$$u_* = \frac{1-\alpha}{1-\alpha\beta}, \quad v_* = \frac{1-\beta}{1-\alpha\beta}. \tag{3.4}$$

The extinction state b_0 and the single-species states b_u and b_v are physical for any selection of α and β. On the other hand, the coexistence state b_{uv} is not physical (i.e., u_* or v_* is negative) if either $\alpha < 1$ and $\beta > 1$ or $\alpha > 1$ and $\beta < 1$.

The linear stability of a fixed point of a system can be determined by analyzing the eigenvalues of the Jacobian matrix of the system evaluated at the fixed point. If the real parts of all eigenvalues are negative, then the fixed point is stable. On the other hand, if at least one eigenvalue has a positive real part, the fixed point is unstable. The Jacobian matrix of (3.2) is

$$J(u,v) = \begin{pmatrix} 1-2u-\alpha v & -\alpha u \\ -\beta v & 1-2v-\beta u \end{pmatrix}. \tag{3.5}$$

The matrix $J(0,0)$ has the repeated eigenvalue 1, meaning that the extinction state b_0 is an unstable node. $J(1,0)$ has eigenvalues -1 and $1-\beta$, so that b_u is stable if $\beta > 1$ and is unstable (specifically, it is a saddle point unstable to perturbations in v) if $\beta < 1$. Similarly, $J(0,1)$ has eigenvalues $1-\alpha$ and -1, so that it is stable if $\alpha > 1$ and is a saddle

point (unstable to perturbations in u) if $\alpha < 1$. Finally, $J(u_*, v_*)$ has eigenvalues -1 and $\frac{(\alpha-1)(\beta-1)}{\alpha\beta-1}$, so that the coexistence state b_{uv} is stable if $\alpha, \beta < 1$ and unstable if $\alpha, \beta > 1$ (recall that the state is not physically relevant otherwise; if either α or β is exactly 1, the state coincides with one of the single-species states).

Further analysis of the two-species model can be found in [**17**].

3.2. Three Species

System (2.12) with three species can be written as

$$\frac{\partial u}{\partial t} = \nabla^2 u + u(1 - u - \alpha v), \tag{3.6a}$$

$$\frac{\partial v}{\partial t} = d_v \nabla^2 v + v(1 - v - \beta w), \tag{3.6b}$$

$$\frac{\partial w}{\partial t} = d_w \nabla^2 w + w(1 - w - \gamma u). \tag{3.6c}$$

As previously mentioned, this system is sometimes referred to as a rock-paper-scissors (RPS) system. For reference, the associated ODE system is

$$\frac{du}{dt} = u(1 - u - \alpha v), \tag{3.7a}$$

$$\frac{dv}{dt} = v(1 - v - \beta w), \tag{3.7b}$$

$$\frac{dw}{dt} = w(1 - w - \gamma u). \tag{3.7c}$$

System (3.7) has eight fixed points (u, v, w):

- Extinction state $c_0 = (0, 0, 0)$
- Single-species states $c_u = (1, 0, 0)$, $c_v = (0, 1, 0)$, and $c_w = (0, 0, 1)$
- Two-species states $c_{uv} = (1 - \alpha, 1, 0)$, $c_{uw} = (1, 0, 1 - \gamma)$, and $c_{vw} = (0, 1 - \beta, 1)$

- Coexistence state $c_{uvw} = (u_*, v_*, w_*)$

The components of the coexistence state are given by

$$u_* = \frac{1+\alpha(\beta-1)}{1+\alpha\beta\gamma}, \quad v_* = \frac{1+\beta(\gamma-1)}{1+\alpha\beta\gamma}, \quad w_* = \frac{1+\gamma(\alpha-1)}{1+\alpha\beta\gamma}. \tag{3.8}$$

As in the two-species case, the extinction state c_0 and the single-species states c_u, c_v, and c_w are physical for any selection of α, β, and γ. The two-species state c_{uv} is not physical if $\alpha > 1$ (similarly, c_{uw} and c_{vw} are not physical if $\gamma > 1$ and $\beta > 1$, respectively). The coexistence state c_{uvw} is not physical if $\alpha < 1 - \frac{1}{\gamma}$, $\beta < 1 - \frac{1}{\alpha}$, or $\gamma < 1 - \frac{1}{\beta}$.

The Jacobian matrix of (3.7) is

$$J(u,v,w) = \begin{pmatrix} 1-2u-\alpha v & -\alpha u & 0 \\ 0 & 1-2v-\beta w & -\beta v \\ -\gamma w & 0 & 1-2w-\gamma u \end{pmatrix}. \tag{3.9}$$

As in the two-species case, the matrix $J(0,0,0)$ has the repeated eigenvalue 1, so that the extinction state c_0 is an unstable node. The single-species state c_u is a saddle, with the matrix $J(1,0,0)$ having eigenvalues -1, 1, and $1-\gamma$, so that the state is stable to perturbations in u, unstable to perturbations in v, and unstable to perturbations in w if $\gamma < 1$ (i.e., when c_{uw} is physical). Similarly, c_v is unstable to perturbations in w and unstable to perturbations in u if $\alpha < 1$, while c_w is unstable to perturbations in u and unstable to perturbations in v if $\beta < 1$. A heteroclinic cycle connects the single-species saddle points such that c_u is displaced by c_v, c_v by c_w, and c_w by c_u. It can be shown [**16, 18, 19**] that the heteroclinic cycle is asymptotically stable, and attracting for all

physical initial conditions, if

$$(\alpha - 1)(\beta - 1)(\gamma - 1) > 1. \tag{3.10}$$

The interaction coefficients α, β, and γ can be expressed in terms of the components of the coexistence state by manipulating the relationships (3.8):

$$\alpha = \frac{1 - u_*}{v_*}, \quad \beta\frac{1 - v_*}{w_*}, \quad \gamma = \frac{1 - w_*}{u_*}. \tag{3.11}$$

Plugging these expressions into (3.10) leads to an equivalent condition for the stability of the heteroclinic cycle; namely,

$$u_* + v_* + w_* < 1. \tag{3.12}$$

The matrix $J(1 - \alpha, 1, 0)$ has eigenvalues $\alpha - 1$, -1, and $1 + \gamma(\alpha - 1)$, so that the two-species state c_{uv} is stable if $\gamma > 1$ and $\alpha < 1 - \frac{1}{\gamma}$. Similarly, c_{uw} is stable if $\beta > 1$ and $\gamma < 1 - \frac{1}{\beta}$, while c_{vw} is stable if $\alpha > 1$ and $\beta < 1 - \frac{1}{\alpha}$. Finally, the coexistence state c_{uvw} is stable (see Appendix A; an alternative proof is given in [**16**]) if

$$u_* + v_* + w_* > 1, \tag{3.13}$$

which is equivalent to the condition

$$(\alpha - 1)(\beta - 1)(\gamma - 1) < 1. \tag{3.14}$$

It is thus clear that the heteroclinic cycle and the coexistence state cannot both be stable.

3.3. Four Species

The four-species version of System (2.12) where three species have identical properties and all species have identical diffusivities can be written as

$$\frac{\partial u}{\partial t} = \nabla^2 u + u(1 - u - \alpha v), \tag{3.15a}$$

$$\frac{\partial v}{\partial t} = d\nabla^2 v + v(1 - v - \beta w), \tag{3.15b}$$

$$\frac{\partial w}{\partial t} = \nabla^2 w + w(1 - w - \alpha z), \tag{3.15c}$$

$$\frac{\partial z}{\partial t} = \nabla^2 z + z(1 - z - \alpha u). \tag{3.15d}$$

The associated ODE system is

$$\frac{du}{dt} = u(1 - u - \alpha v), \tag{3.16a}$$

$$\frac{dv}{dt} = v(1 - v - \beta w), \tag{3.16b}$$

$$\frac{dw}{dt} = w(1 - w - \alpha z), \tag{3.16c}$$

$$\frac{dz}{dt} = z(1 - z - \alpha u). \tag{3.16d}$$

System (3.16) has sixteen fixed points (u, v, w, z):

- Extinction state $e_0 = (0, 0, 0, 0)$
- Single-species states $e_u = (1, 0, 0, 0)$, $e_v = (0, 1, 0, 0)$, $e_w = (0, 0, 1, 0)$, and $e_z = (0, 0, 0, 1)$
- Two-species competing states $e_{uv} = (1 - \alpha, 1, 0, 0)$, $e_{uz} = (1, 0, 0, 1 - \alpha)$, $e_{vw} = (0, 1 - \beta, 1, 0)$, and $e_{wz} = (0, 0, 1 - \alpha, 1)$
- Two-species non-competing states $e_{uw} = (1, 0, 1, 0)$ and $e_{vz} = (0, 1, 0, 1)$

- Three-species states $e_{uvw} = (1-\alpha(1-\beta), 1, 1-\beta, 0)$, $e_{uvz} = (1-\alpha, 1, 0, 1-\alpha(1-\alpha))$, $e_{uwz} = (1, 0, 1-\alpha(1-\alpha), 1-\alpha)$, and $e_{vwz} = (0, 1-\beta(1-\alpha), 1-\alpha, 1)$
- Coexistence state $e_{uvw} = (u_*, v_*, w_*, z_*)$

The components of the coexistence state are given by

$$u_* = \frac{(1-\alpha)+\alpha\beta(1-\alpha)}{1-\alpha^3\beta}, \quad v_* = \frac{(1-\beta)+\alpha\beta(1-\alpha)}{1-\alpha^3\beta}, \tag{3.17}$$
$$w_* = \frac{(1-\alpha)+\alpha^2(1-\alpha)}{1-\alpha^3\beta}, \quad z_* = \frac{(1-\alpha)+\alpha^2(1-\beta)}{1-\alpha^3\beta}.$$

As in the previous cases, the extinction state e_0 and the single-species states e_u, e_v, e_w, and e_z are physical for any selection of α and β. Moreover, the non-competing two-species states e_{uw} and e_{vz} are always physical. The two-species competing states e_{uv}, e_{uz}, and e_{wz} are not physical if $\alpha > 1$, while e_{vw} is not physical if $\beta > 1$.

The following summarizes the conditions for physicality of the three-species states:

- e_{uvw} is not physical if $\beta > 1$ or if $\alpha > 1$ and $\beta < 1 - \frac{1}{\alpha}$
- e_{uvz} and e_{uwz} are not physical if $\alpha > 1$
- e_{vwz} is not physical if $\alpha > 1$ or if $\beta > 1$ and $\alpha < 1 - \frac{1}{\beta}$

The coexistence state e_{uvwz} is not physical if one of the following is true:

- $\alpha < 1$ and $\beta > \frac{1}{1-\alpha+\alpha^2}$
- $\alpha > 1$ and $\beta < \frac{\alpha^2-\alpha+1}{\alpha^2}$

The Jacobian matrix of (3.16) is

$$J(u,v,w,z) = \begin{pmatrix} 1-2u-\alpha v & -\alpha u & 0 & 0 \\ 0 & 1-2v-\beta w & -\beta v & 0 \\ 0 & 0 & 1-2w-\alpha z & -\alpha w \\ -\alpha z & 0 & 0 & 1-2z-\alpha u \end{pmatrix}. \tag{3.18}$$

The matrix $J(0,0,0,0)$ has the repeated eigenvalue 1, so that the extinction state e_0 is unstable. The matrix $J(1,0,0,0)$ has eigenvalues -1, 1, 1, and $1-\alpha$, so that the single-species state e_u is unstable to perturbations in v and w and, if $\alpha < 1$, to perturbations in z. The other single-species states have analogous stability properties. The two-species competing states are also always unstable. On the other hand, the two-species non-competing state e_{uw} is stable if $\alpha, \beta > 1$, while e_{vz} is stable if $\alpha > 1$.

The stability properties of the three-species states are as follows:

- e_{uvw} is stable if $\alpha > 1$ and $\frac{1-a+a^2}{a^2} < \beta < 1$
- e_{uvz} and e_{vwz} are unstable when physical
- e_{uwz} is stable if $\alpha < 1$ and $\beta > \frac{1}{1-\alpha+\alpha^2}$

Finally, the coexistence state is stable if $\alpha^3\beta < 1$ and unstable if $\alpha^3\beta > 1$ [**20**].

CHAPTER 4

Analytical Methods and Previous Results

4.1. Fisher-KPP Equation

4.1.1. Existence of Traveling Wave Solutions

Taking (2.12) in one spatial dimension with $N = 1$ over $\mathbb{R}$ gives

$$\frac{\partial u}{\partial t} = d\frac{\partial^2 u}{\partial x^2} + Ku(1-u), \tag{4.1}$$

where $d, K > 0$ are constants (note that, as shown above, the equation describing the population of a single species can be nondimensionalized such that $d = K = 1$; however, the more general form of the equation will be considered here). This equation is known as Fisher's equation or the Kolmogorov-Petrovsky-Piskunov (KPP) equation, and it is well known that it admits a class of traveling wave solutions $u(z) = u(x - st)$ (where $s > 0$ is the speed of the wave) [**21**]. Making this transformation gives

$$\frac{\partial}{\partial t} = -s\frac{d}{dz}, \qquad \frac{\partial}{\partial r} = \frac{d}{dz}, \tag{4.2}$$

so that (4.1) can be written as

$$d\frac{d^2 u}{dz^2} + s\frac{du}{dz} + Ku(1-u) = 0, \tag{4.3}$$

or, as a first-order system,

$$\frac{du}{dz} = v, \tag{4.4a}$$

$$\frac{dv}{dz} = -\frac{s}{d}v - \frac{K}{d}u(1-u). \tag{4.4b}$$

It is easy to see that (4.4) has two fixed points: $(u, v) = (0, 0)$ and $(u, v) = (1, 0)$. Noting that the Jacobian matrix of (4.4) is

$$J(u,v) = \begin{pmatrix} 0 & 1 \\ -\frac{K}{d}(1-2u) & -\frac{s}{d} \end{pmatrix}, \tag{4.5}$$

it is readily found that the eigenvalues of $J(0, 0)$ are

$$\lambda_0^{\pm} = \frac{-s \pm \sqrt{s^2 - 4dK}}{2d} \tag{4.6}$$

and that the eigenvalues of $J(1, 0)$ are

$$\lambda_1^{\pm} = \frac{-s \pm \sqrt{s^2 + 4dK}}{2d}. \tag{4.7}$$

Recalling that $d, K, s > 0$, it is always true that λ_1^+ is positive and λ_1^- is negative, so that the point $(u, v) = (1, 0)$ is a saddle. On the other hand, λ_0^+ and λ_0^- are always negative, so that the point $(u, v) = (0, 0)$ is a stable spiral if $s^2 < 4dK$, and a stable node otherwise. Thus, there is a heteroclinic orbit from $(1, 0)$ to $(0, 0)$, corresponding to traveling wave solutions $u(z)$ such that $u \to 1$ as $z \to -\infty$ and $u \to 0$ as $z \to \infty$. If $s^2 < 4dK$, however, such a solution is unphysical with respect to a population, since, in this case, any approach to the point $(0, 0)$ in u-v space will always require that u is negative at some point on

the trajectory, given that $(0,0)$ is a spiral sink. For this reason, relevant traveling wave solutions of the Fisher-KPP equation have a minimum speed of $2\sqrt{dK}$. It has been shown that traveling wave solutions will have the minimum speed when the initial condition has compact support [**21**]. This is also the case when the initial interface between the areas where $u = 1$ and $u = 0$ is sufficiently steep (e.g., if the initial condition is a Heaviside function).

4.1.2. Approximation of Traveling Wave Solutions

Although there is only one known closed-form traveling wave solution to the Fisher-KPP equation [**21**], approximations to these solutions exist. Letting $\varepsilon = \frac{1}{s^2}$, $\xi = \frac{z}{\sqrt{\varepsilon}}$, and $u(z) = g(\xi)$, (4.3) may be rescaled [**22**] to give

$$\varepsilon d\frac{d^2g}{d\xi^2} + \frac{dg}{d\xi} + Kg(1-g) = 0, \tag{4.8}$$

where, for the reason discussed above, the conditions

$$g(\xi) \to 1, \quad \xi \to -\infty, \tag{4.9a}$$

$$g(\xi) \to 0, \quad \xi \to \infty \tag{4.9b}$$

are imposed. Furthermore, the point $\xi = \xi_0 = \frac{z_0}{\sqrt{\varepsilon}}$ is defined such that $g(\xi_0) = \frac{1}{2}$. For a continuous solution, such a point is guaranteed to exist. Expanding $g(\xi)$ such that $g(\xi) = g_0(\xi) + \varepsilon g_1(\xi) + \varepsilon^2 g_2(\xi) + \ldots$ results in the leading order problem

$$\frac{dg_0}{d\xi} = -Kg_0(1-g_0), \tag{4.10}$$

which has the general solution

$$g_0(\xi) = \frac{1}{1 + Ae^{K\xi}}, \tag{4.11}$$

where conditions (4.9) are automatically satisfied and the condition $g(z_0) = \frac{1}{2}$ requires $A = e^{-Kz_0/s}$. Thus,

$$u(z) \sim \frac{1}{1 + e^{K(z-z_0)/s}}. \tag{4.12}$$

Although this approximation is most accurate for large s, it turns out to still be a good approximation for $s \approx 2$. This is shown in Figure 4.1, where the approximation (with $K = 1$ and $z_0 = 0$) is compared to the exact solution for $s = \frac{5}{\sqrt{6}} \approx 2.04$, which is (for $K = 1$) [**21**]

$$u(z) = \frac{1}{(1 + (\sqrt{2} - 1)e^{z/\sqrt{6}})^2}. \tag{4.13}$$

4.1.3. Curvature-Speed Relationship

Consider the two-dimensional Fisher-KPP equation

$$\frac{\partial u}{\partial t} = d\left(\frac{\partial^2 u}{\partial x^2} + \frac{\partial^2 u}{\partial y^2}\right) + Ku(1 - u) \tag{4.14}$$

on $\mathbb{R}^2$. Suppose the initial condition is

$$u(x, y, 0) = \begin{cases} 1, & x \leq 0, \\ 0, & x > 0. \end{cases} \tag{4.15}$$

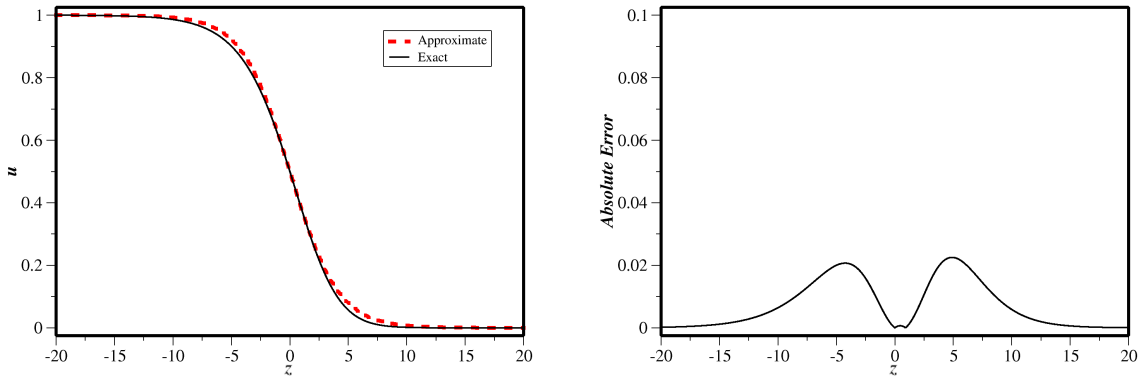

(a) (b)

Figure 4.1. a) Approximation (4.12) versus exact traveling wave solution with speed $5/\sqrt{6}$ to the Fisher-KPP equation with $K = 1$. b) Absolute error of the approximation.

It is clear that the solution will be independent of y; thus, the problem can be treated as a one-dimensional problem. Since the initial interface has a steep gradient (it is the Heaviside function H_0), the solution will be a traveling wave with speed $2\sqrt{dK}$. Solutions of this type are referred to as plane waves because the interface between the regions where $u = 1$ and $u = 0$ remains flat in x-y space (i.e., has zero curvature) for all time (see Figure 4.2).

It turns out, however, that curvature has an effect on wave speed. Transforming this equation into polar coordinates and assuming a solution independent of polar angle gives

$$\frac{\partial u}{\partial t} = d\left(\frac{\partial^2 u}{\partial r^2} + \frac{1}{r}\frac{\partial u}{\partial r}\right) + Ku(1-u), \tag{4.16}$$

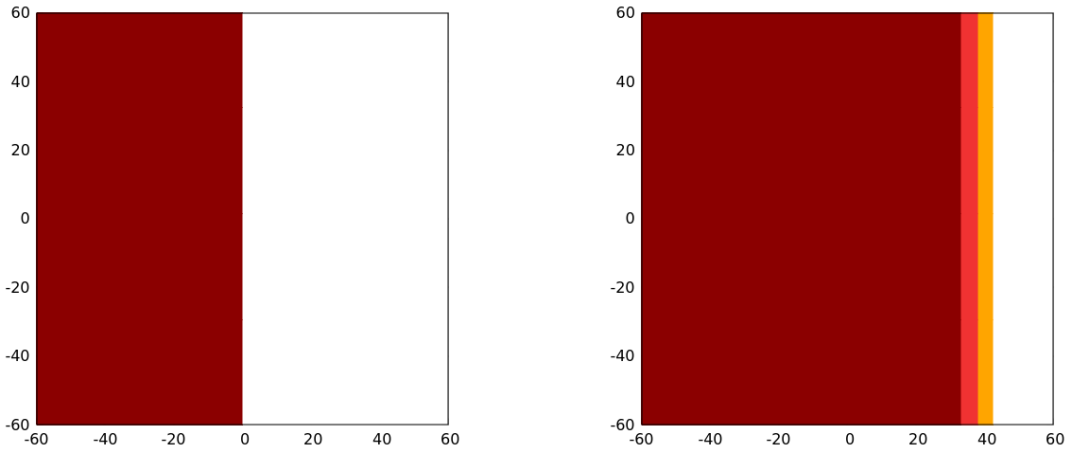

Figure 4.2. a) Initial condition (4.15). b) Solution to the 2D Fisher-KPP equation with $d = K = 1$ at $t = 20$ for this initial condition. Dark red regions mark where $u \geq 0.5$, light red where $u \geq 0.05$, and orange where $u \geq 0.01$.

where $r = \sqrt{x^2 + y^2}$. Suppose the initial condition is

$$u(r,0) = \begin{cases} 1, & r \leq R_0, \\ 0, & r > R_0; \end{cases} \tag{4.17}$$

i.e., a circular patch of radius R_0 where $u = 1$ surrounded by empty space (Figure 4.3a). It is intuitive that the patch should expand over time, but it is not obvious how quickly the expansion should happen. The dependence of the wave speed on the curvature of the interface can be found for small curvature (i.e., large R, with $R(t)$ the radius of the patch) by assuming a solution of the form $u(r,t) = u(z)$, where $z = r - S(R)t$. The analysis in [**23**] reveals that the speed of the traveling wave should be

$$S(R) \sim s_0 - \frac{d}{R(t)}, \tag{4.18}$$

valid for large R, with s_0 the speed of the corresponding planar wave (i.e., the speed that would be expected if there were no curvature). In this case, $s_0 = 2\sqrt{dK}$, since the initial interface has a steep gradient. Formula (4.18) is also valid, without restriction on R, for small diffusivities d [**21, 24, 25**].

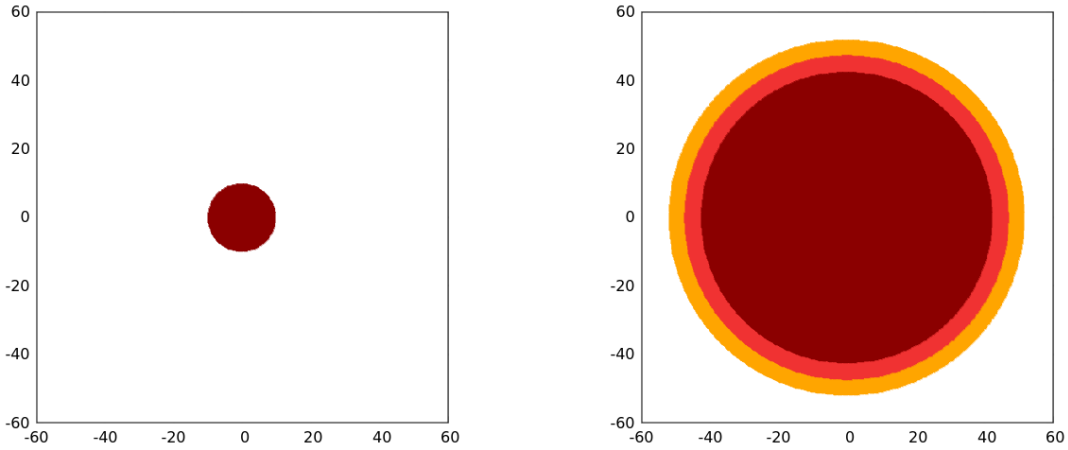

Figure 4.3. a) Initial condition (4.17) with $R_0 = 10$. b) Solution to the 2D Fisher-KPP equation with $d = K = 1$ at $t = 20$ for this initial condition. Color scheme is as in Figure 4.2.

4.2. Estimated Propagation Speed of a Pulled Front

4.2.1. Methodology

Consider the displacement of an unstable state p of the one-dimensional version of System (2.12) by some other state via propagation of a pulled front. The term "pulled" here means that propagation of the front is dictated by properties of the displaced state. A procedure for estimating the speed of such a front is described in great detail in [**26**] and is summarized below.

To find possible speeds, System (2.12) is linearized about the point p in state space and solutions of the form

$$\vec{u}(x,t) \approx e^{\Lambda t} e^{-kx} \tilde{u} = e^{-k\left(x - \frac{\Lambda}{k} t\right)} \tilde{u}, \tag{4.19}$$

are sought, where $\vec{u} = \begin{pmatrix} u_1, & u_2, & \ldots, & u_N \end{pmatrix}$. The speed of displacement is clearly given by $s = \frac{\Lambda}{k}$. Assuming the interface between the displacing and displaced states (i.e., the front) is sufficiently steep, the expected speed of the front is the minimal possible speed s_{min} [**27**]. Letting J be the Jacobian matrix of the spatially-homogeneous (ODE) version of System (2.12) evaluated for the state p and looking for solutions of the form (4.19) gives

$$\Lambda \tilde{u} = (k^2 D + J)\tilde{u}, \tag{4.20}$$

where D is the diagonal matrix containing the diffusivities of the species; i.e.,

$$D = \begin{pmatrix} 1 & & & \\ & d_2 & & \\ & & \ddots & \\ & & & d_N \end{pmatrix}. \tag{4.21}$$

This implies Λ is an eigenvalue of the matrix $k^2 D + J$. The minimal speed can then be obtained via simple calculus.

For the expansion of a two-dimensional circular patch (which is independent of the polar angle θ), an approximation to the minimal speed for large R (with $R(t)$ the radius of the patch) can be found by looking for a solution of the form

$$\vec{u}(r,\theta,t) \approx e^{\Lambda t} e^{-kr} \tilde{u} = e^{-k\left(r - \frac{\Lambda}{k} t\right)} \tilde{u} \tag{4.22}$$

to the system

$$\frac{\partial u_1}{\partial t} = \frac{\partial^2 u_1}{\partial r^2} + u_1(1 - u_1 - \alpha_1 u_2), \tag{4.23a}$$

$$\frac{\partial u_2}{\partial t} = d_2 \frac{\partial^2 u_2}{\partial r^2} + u_2(1 - u_2 - \alpha_2 u_3), \tag{4.23b}$$

$$\vdots$$

$$\frac{\partial u_N}{\partial t} = d_N \frac{\partial^2 u_N}{\partial r^2} + u_N(1 - u_N - \alpha_N u_1); \tag{4.23c}$$

i.e., the Laplacian $\nabla^2 u = \frac{\partial^2 u}{\partial r^2} + \frac{1}{r}\frac{\partial u}{\partial r}$ (the independence from θ implies $\frac{\partial^2 u}{\partial \theta^2}$ is zero everywhere) is approximated by $\frac{\partial^2 u}{\partial r^2}$. Note that this is just the one-dimensional problem with the spatial variable x replaced by r. The approximate minimal speed s_p is then determined via the procedure described above. Supposing that all the diffusivities are identical (i.e., equal to 1), a trivial extension of the analysis in [**23**] reveals that the correction to the minimal speed due to curvature is just $-\frac{1}{R(t)}$, so that the estimated minimal speed is $s_{min} = s_p - \frac{1}{R(t)}$. For a contraction of a circular patch, the minimal speed is then approximately $s_{min} = s_p + \frac{1}{R(t)}$ (see also Section 6.1.2).

4.2.2. Examples

Below are two simple examples of the application of the above methodology to one-dimensional problems.

4.2.2.1. One Species. Consider System (2.12) with $N = 1$; i.e.,

$$\frac{\partial u}{\partial t} = \frac{\partial^2 u}{\partial x^2} + u(1 - u). \tag{4.24}$$

The speed of displacement of the unstable state $u = 0$ by the (stable) state $u = 1$ is of interest. The Jacobian "matrix" of the ODE version of (4.24) is $J = 1 - 2u$, so that at $u = 0$, $J = 1$. Moreover, $D = 1$ in this case, so that the eigenvalue Λ of $k^2D + J$ is $k^2 + 1$. Thus, possible speeds of displacement are given by the expression

$$s(k) = \frac{\Lambda}{k} = k + \frac{1}{k}, \tag{4.25}$$

which attains its minimum value at $k = 1$ (note that speed is required to be nonnegative). In this case, then, $s_{min} = 2$, which is consistent with the minimal speed of a traveling wave to the Fisher-KPP equation with $d = K = 1$ (see Section 4.1.1).

4.2.3. Two Species

Consider System (3.1) with $\alpha > 1$ and $\beta < 1$ so that the single-species state b_u is unstable, while b_v is stable. The speed of displacement of the unstable state b_u by b_v is of interest here. The Jacobian matrix of (3.2) evaluated for the b_u state is

$$J = \begin{pmatrix} -1 & -\alpha \\ 0 & 1-\beta \end{pmatrix}, \tag{4.26}$$

so that

$$k^2D + J = \begin{pmatrix} k^2 - 1 & -\alpha \\ 0 & k^2 d_v + 1 - \beta \end{pmatrix}, \tag{4.27}$$

whose eigenvalues are clearly $k^2 - 1$ and $k^2 d_v + 1 - \beta$. The first of these eigenvalues is not always positive, so it is irrelevant in determining the speed of displacement [**27**] (indeed,

it is clear that there is no finite minimum of the function $s(k) = k - \frac{a}{k}$, where $a > 0$). Thus, $\Lambda = k^2 d_v + 1 - \beta$, so that

$$s(k) = \frac{\Lambda}{k} = k d_v + \frac{1-\beta}{k}. \tag{4.28}$$

This function has a minimum at $k = \sqrt{\frac{1-\beta}{d_v}}$. Thus, the speed of propagation is expected to be $s_{min} = 2\sqrt{d_v(1-\beta)}$.

CHAPTER 5

Numerical Methods

5.1. One-Dimensional Problem

5.1.1. Discrete Fourier Transform (DFT)

Consider a real-valued function $f(x)$ periodic on the interval $0 \leq x \leq 2\pi$. The function can be approximated as a sum of N Fourier modes; i.e.,

$$f(x) \approx \sum_{k=0}^{N-1} A_k e^{ikx}, \tag{5.1}$$

where N is assumed to be even and the coefficients A_k are given by

$$A_k = \frac{1}{2\pi} \int_0^{2\pi} f(x) e^{-ikx}\, dx. \tag{5.2}$$

Since $f(x)$ is real-valued, it must be true that

$$A_{N-k} = \bar{A}_k \tag{5.3}$$

for $1 \leq k \leq N-1$. If the values of $f(x)$ are known at the discrete points (nodes) $X_j = \frac{2\pi j}{N}$, $0 \leq j \leq N-1$, the Fourier coefficients A_k can be approximated via Riemann sums; i.e.,

$$A_k \approx \frac{1}{2\pi} \left[\sum_{j=0}^{N-1} f(X_j) e^{-ikX_j} \right] \left(\frac{2\pi}{N} \right), \tag{5.4}$$

which reduces to

$$A_k \approx \frac{1}{N}\left[f(0) + \sum_{j=1}^{N-1} f\left(\frac{2\pi j}{N}\right) e^{-2\pi i j k/N}\right]. \tag{5.5}$$

This is the discrete Fourier transform (DFT) of $f(x)$, with the inverse (IDFT) given by (5.1) at the nodes X_j:

$$f(X_j) \approx \sum_{k=0}^{N-1} A_k e^{2\pi i j k/N}. \tag{5.6}$$

Using the relationship (5.3) and the facts that $e^{ikx} = \cos(kx) + i\sin(kx)$ and $e^{2\pi i j(N-k)/N} = e^{-2\pi i j k/N}$ reduces the IDFT to

$$f(X_j) \approx A_0 + (-1)^j A_{N/2} + 2\sum_{k=1}^{N/2-1} \Re(A_k)\cos\left(\frac{2\pi j k}{N}\right) - \Im(A_k)\sin\left(\frac{2\pi j k}{N}\right), \tag{5.7}$$

so that it is only necessary to compute $N/2+1$ coefficients A_k. Note that the formulation of the IDFT enforces the condition $f(0) = f(2\pi)$, making the DFT a natural tool for solving problems with periodic boundary conditions.

The transform (5.5) can be split into two transforms of size $N/2$:

$$A_k = \sum_{m=0}^{N/2-1} f(X_{2m}) e^{-2\pi(2m)ki/N} + \sum_{m=0}^{N/2-1} f(X_{2m+1}) e^{-2\pi(2m+1)ki/N} \tag{5.8}$$

$$= \sum_{m=0}^{N/2-1} f(X_{2m}) e^{-2\pi mki/(N/2)} + e^{-2\pi ki/N} \sum_{m=0}^{N/2-1} f(X_{2m+1}) e^{-2\pi mki/(N/2)}. \tag{5.9}$$

The advantage of doing this is that since the complex exponentials in both sums are identical, the computational cost of the transform is lowered. The transforms of size $N/2$ can then be further split into transforms of size $N/4$, and so on. Algorithms that reuse

parts of previous computations to calculate a DFT are known as fast Fourier transforms (FFT) (this case is the radix-2 FFT), which reduce the cost of the computation of the DFT from $O(N^2)$ to $O(N \log(N))$ [**28**]. A similar procedure can be used to calculate the IDFT.

5.1.2. Derivatives and Scaling

If the domain of interest is not $[0, 2\pi]$ (i.e., if a function is not 2π-periodic), the formulation of the DFT can be rescaled. The change of variable

$$\tilde{x} = \frac{L}{\pi}(x - \pi) \tag{5.10}$$

transforms the domain from $[0, 2\pi]$ to $[-L, L]$. The series (5.1) becomes

$$\tilde{f}(\tilde{x}) \approx \sum_{k=0}^{N-1} \tilde{A}_k e^{\pi i k(1+\tilde{x}/L)}, \tag{5.11}$$

with

$$\tilde{A}_k = \frac{1}{2L} \int_{-L}^{L} \tilde{f}(\tilde{x}) e^{-\pi i k(1+\tilde{x}/L)} \, d\tilde{x}. \tag{5.12}$$

Additionally, the new nodes are $\tilde{X}_j = L\left(\frac{2j}{N} - 1\right)$. Note that the complex exponentials are therefore exactly the same as before, since

$$e^{\pi i k(1+\tilde{X}_j)/L)} = e^{\pi i k\left(1+L\left(\frac{2j}{N}-1\right)/L\right)} = e^{2\pi i j k/N}. \tag{5.13}$$

Thus, the DFT is now

$$\tilde{A}_k \approx \frac{1}{N}\left[\tilde{f}(-L) + \sum_{j=1}^{N-1} \tilde{f}\left(L\left(\frac{2j}{N} - 1\right)\right) e^{-2\pi ijk/N}\right], \tag{5.14}$$

while the IDFT is just

$$\tilde{f}(\tilde{X}_j) \approx \tilde{A}_0 + (-1)^j \tilde{A}_{N/2} + 2\sum_{k=1}^{N/2-1} \Re(\tilde{A}_k)\cos\left(\frac{2\pi jk}{N}\right) - \Im(\tilde{A}_k)\sin\left(\frac{2\pi jk}{N}\right). \tag{5.15}$$

From (5.11), the second derivative of the function $\tilde{f}(\tilde{x})$ is

$$\tilde{f}''(\tilde{x}) \approx \sum_{k=0}^{N-1} -\frac{\pi^2 k^2}{L^2}\tilde{A}_k e^{\pi ik(1+\tilde{x}/L)}, \tag{5.16}$$

so that the second derivative of the function $\tilde{f}$ can be evaluated from the DFT of $\tilde{f}$. Letting $\tilde{A}_k$ be defined as in (5.14),

(5.17)

$$\tilde{f}''(\tilde{X}_j) \approx s_x^2\left[-\left(\frac{N}{2}\right)^2 (-1)^j \tilde{A}_{N/2} + 2\sum_{k=1}^{N/2-1} -k^2\Re(\tilde{A}_k)\cos\left(\frac{2\pi jk}{N}\right) + k^2\Im(\tilde{A}_k)\sin\left(\frac{2\pi jk}{N}\right)\right],$$

where $s_x = \frac{\pi}{L}$. It is also straightforward to show that $\frac{d^2\tilde{A}_k}{d\tilde{x}^2} \approx -k^2 s_x^2 \tilde{A}_k$, so that it is possible (and sometimes more convenient) to introduce the factors s_x^2 and $-k^2$ in the coefficients $\tilde{A}_k$ themselves (see Section 5.1.3.1).

5.1.3. 1D Solver

For concreteness, consider the one-dimensional version of System (3.1). The numerical method for solving the system consists of two stages: a predictor stage and a corrector stage. The solution is advanced by half of a time step in the predictor stage and then

advanced the full time step in the corrector stage. To begin, N nodes (with N even) X_j are chosen such that $X_j = L\left(\frac{2j}{N} - 1\right)$, with $0 \leq j \leq N-1$. Thus, the leftmost node X_0 corresponds to the point $x = -L$, whereas the rightmost node X_{N-1} corresponds to the point $x = L - \frac{2L}{N}$. The node $X_{N/2}$ corresponds to the point $x = 0$. At each time, the values of v at the nodes, $V_j = v(X_j)$, can be grouped into a vector $\mathbf{V}$. Obviously, the same can be done for u (grouped into the vector $\mathbf{U}$).

5.1.3.1. Predictor. The derivative of v with respect to time at time step n can be approximated as

$$\frac{\partial \mathbf{V}^n}{\partial t} \approx \frac{\mathbf{V}^{n+1} - \mathbf{V}^n}{\Delta t}, \tag{5.18}$$

where Δt is the time step size and the notation $\mathbf{V}^n$ means "$\mathbf{V}$ at time step n." For this method, the time steps are fixed, so Δt is a constant. In the predictor stage, the solution is advanced by only half a time step, so

$$\frac{\partial \mathbf{V}^n}{\partial t} \approx \frac{\mathbf{V}^{n+1/2} - \mathbf{V}^n}{\Delta t/2}. \tag{5.19}$$

Plugging this into the second equation in System (3.1) gives

$$\frac{\mathbf{V}^{n+1/2} - \mathbf{V}^n}{\Delta t/2} \approx d_v \frac{\partial^2 \mathbf{V}^{n+1/2}}{\partial x^2} + \mathbf{V}^n \cdot (\mathbf{1} - \mathbf{V}^n - \beta \mathbf{U}^n), \tag{5.20}$$

where the spatial second derivative is computed at time step $n + 1/2$ for stability. Transforming the equation into Fourier space gives

$$\frac{\mathcal{F}(\mathbf{V}^{n+1/2})_k - \mathcal{F}(\mathbf{V}^n)_k}{\Delta t/2} \approx d_v \frac{\partial^2 \mathcal{F}(\mathbf{V}^{n+1/2})_k}{\partial x^2} + \mathcal{F}(\mathbf{NLV}^n)_k, \tag{5.21}$$

where $\mathcal{F}(\mathbf{V}^n)_k$ denotes the k^{th} component of the DFT of v at time step n (i.e., the coefficient $\tilde{A}_k$ in (5.14)) and

$$\mathbf{NLV}^n = \mathbf{V}^n \cdot (\mathbf{1} - \mathbf{V}^n - \beta \mathbf{U}^n). \tag{5.22}$$

As discussed in 5.1.2,

$$\frac{\partial^2 \mathcal{F}(\mathbf{V}^{n+1/2})_k}{\partial x^2} = -s_x^2 k^2 \mathcal{F}(\mathbf{V}^{n+1/2})_k, \tag{5.23}$$

where $s_x = \frac{\pi}{L}$, so that (5.21) can be written as

$$\frac{\mathcal{F}(\mathbf{V}^{n+1/2})_k - \mathcal{F}(\mathbf{V}^n)_k}{\Delta t/2} \approx -d_v s_x^2 k^2 \mathcal{F}(\mathbf{V}^{n+1/2})_k + \mathcal{F}(\mathbf{NLV}^n)_k. \tag{5.24}$$

Solving for $\mathcal{F}(\mathbf{V}^{n+1/2})$ gives

$$\mathcal{F}(\mathbf{V}^{n+1/2})_k \approx \frac{\mathcal{F}(\mathbf{V}^n)_k + \frac{\Delta t}{2}\mathcal{F}(\mathbf{NLV}^n)_k}{1 + \frac{\Delta t}{2} d_v s_x^2 k^2}. \tag{5.25}$$

In a similar way,

$$\mathcal{F}(\mathbf{U}^{n+1/2})_k \approx \frac{\mathcal{F}(\mathbf{U}^n)_k + \frac{\Delta t}{2}\mathcal{F}(\mathbf{NLU}^n)_k}{1 + \frac{\Delta t}{2} s_x^2 k^2}, \tag{5.26}$$

where

$$\mathbf{NLU}^n = \mathbf{U}^n \cdot (\mathbf{1} - \mathbf{U}^n - \alpha \mathbf{V}^n). \tag{5.27}$$

The physical solutions $\mathbf{V}^{n+1/2}$ and $\mathbf{U}^{n+1/2}$ are then found simply by taking the IDFT of $\mathcal{F}(\mathbf{V}^{n+1/2})$ and $\mathcal{F}(\mathbf{U}^{n+1/2})$, respectively.

5.1.3.2. Corrector. In the corrector stage, the solution at time step $n+1/2$ is used to evaluate the nonlinear terms and the diffusion operator is split into implicit and explicit components. The second equation of System (3.1) is then

$$\frac{\mathbf{V}^{n+1}-\mathbf{V}^{n}}{\Delta t} \approx \frac{d_v}{2}\left[\frac{\partial^2 \mathbf{V}^{n+1}}{\partial x^2}+\frac{\partial^2 \mathbf{V}^{n}}{\partial x^2}\right]+\mathbf{V}^{n+1/2}\cdot(\mathbf{1}-\mathbf{V}^{n+1/2}-\beta\mathbf{U}^{n+1/2}). \tag{5.28}$$

Transforming into Fourier space and evaluating the spatial derivative gives

$$\frac{\mathcal{F}(\mathbf{V}^{n+1})_k-\mathcal{F}(\mathbf{V}^{n})_k}{\Delta t} \approx \frac{-d_v s_x^2 k^2}{2}\left[\mathcal{F}(\mathbf{V}^{n+1})_k+\mathcal{F}(\mathbf{V}^{n})_k\right]+\mathcal{F}(\mathbf{NLV}^{n+1/2}). \tag{5.29}$$

Solving for $\mathcal{F}(\mathbf{V}^{n+1})_k$ results in

$$\mathcal{F}(\mathbf{V}^{n+1})_k \approx \frac{(1-\frac{\Delta t}{2}d_v s_x^2 k^2)\mathcal{F}(\mathbf{V}^{n})_k+\Delta t\mathcal{F}(\mathbf{NLV}^{n+1/2})_k}{1+\frac{\Delta t}{2}d_v s_x^2 k^2}. \tag{5.30}$$

Similarly,

$$\mathcal{F}(\mathbf{U}^{n+1})_k \approx \frac{(1-\frac{\Delta t}{2}s_x^2 k^2)\mathcal{F}(\mathbf{U}^{n})_k+\Delta t\mathcal{F}(\mathbf{NLU}^{n+1/2})_k}{1+\frac{\Delta t}{2}s_x^2 k^2} \tag{5.31}$$

and the physical solutions $\mathbf{V}^{n+1}$ and $\mathbf{U}^{n+1}$ are found by taking the inverse IDFT of $\mathcal{F}(\mathbf{V}^{n+1})$ and $\mathcal{F}(\mathbf{U}^{n+1})$, respectively.

This method is second order in time. Time steps were chosen to be small enough that solution behavior was qualitatively unaffected by a doubling of the step size. The method was implemented in Fortran and routines from the free FFTW library [**29**] were sometimes used to compute the discrete Fourier transforms and the inverse transforms.

5.2. Two-Dimensional Problem

5.2.1. 1D Discrete Cosine Transform (DCT)

In Section 5.1.1, it was shown that a real-valued function $f(x)$ that is periodic on the interval $[0, 2\pi]$ can be represented by a series of Fourier modes. If $f(x)$ is also even with respect to the point $x = \pi$ (i.e., $f(x) = f(2\pi - x)$, then $f(X_j) = f(X_{N-j})$, where $X_j = \frac{2\pi j}{N}$, $0 \leq j \leq N - 1$. Thus,

$$f(X_{N-j})e^{-2\pi ik(N-j)/N} = f(X_j)e^{-2\pi i}e^{2\pi ijk/N} = f(X_j)e^{2\pi ijk/N}, \tag{5.32}$$

so that the approximation of the Fourier coefficients (5.5) becomes

$$A_k \approx \frac{1}{N}\left[f(0) + (-1)^k f(\pi) + 2\sum_{j=1}^{N/2-1} f(X_j)\cos\left(\frac{2\pi jk}{N}\right)\right]. \tag{5.33}$$

Note that all of the coefficients are real; thus,

$$f(X_j) \approx A_0 + (-1)^j A_{N/2} + 2\sum_{k=1}^{N/2-1} A_k \cos\left(\frac{2\pi jk}{N}\right). \tag{5.34}$$

The properties of f imply that its derivative vanishes at the points $x = 0$ and $x = \pi$. Thus, (5.33) can be used to transform a function $g(x)$ defined on the interval $[0, \pi]$ with $g'(0) = g'(\pi) = 0$ as follows:

$$A_k \approx \frac{1}{2(M-1)}\left[g(0) + (-1)^k g(\pi) + 2\sum_{j=1}^{M-2} g(X_j)\cos\left(\frac{\pi jk}{M-1}\right)\right], \tag{5.35}$$

where $M = N/2 + 1$ and the nodes thus $X_j = \frac{\pi j}{M-1}$, $0 \leq j \leq M-1$ (note that the locations of the nodes are unchanged). The values $g(X_j)$ can then be recovered by

$$g(X_j) \approx A_0 + (-1)^j A_{M-1} + 2\sum_{k=1}^{M-2} A_k \cos\left(\frac{\pi jk}{M-1}\right). \tag{5.36}$$

The transform (5.35) is known as a discrete cosine transform (DCT); specifically, it is the DCT-I. A useful feature of this transform is that it is nearly its own inverse; the form of the inverse (IDCT) (5.36) is identical to that of the DCT except for the absence of the scaling factor $\frac{1}{2(M-1)}$. Note that the formulation of the IDCT enforces the condition $g'(0) = g'(\pi) = 0$, making the DCT a natural tool for solving problems with no-flux boundary conditions.

5.2.2. 2D DCT

Consider first a function of two variables, $f(x, y)$, on the domain $[0, 2\pi] \times [0, 2\pi]$ with $f(0, y) = f(2\pi, y)$ and $f(x, 0) = f(x, 2\pi)$ (i.e., f is 2π-periodic in both x and y). Then f can be approximated by the nested series

$$f(x, y) \approx \sum_{k=0}^{N_x-1} \sum_{l=0}^{N_y-1} A_{k,l} e^{ikx} e^{ily}, \tag{5.37}$$

where

$$A_{k,l} = \left(\frac{1}{2\pi}\right)^2 \int_0^{2\pi} \int_0^{2\pi} f(x, y) e^{-ikx} e^{-iky}\, dydx. \tag{5.38}$$

As in the 1D case (see Section 5.1.1), the coefficients $A_{k,l}$ can be approximated by Riemann sums, which gives

$$
\begin{aligned}
A_{k,l} &\approx \frac{1}{4\pi^2} \int_0^{2\pi} \sum_{p=0}^{N_y-1} \left(f(x, Y_p) e^{-ilY_p} \right) \left(\frac{2\pi}{N_y} \right) dx \\
&\approx \frac{1}{4\pi^2} \sum_{j=0}^{N_x-1} \left[\sum_{p=0}^{N_y-1} \left(f(X_j, Y_p) e^{-ilY_p} \left(\frac{2\pi}{N_y} \right) \right) e^{-ikX_j} \left(\frac{2\pi}{N_x} \right) \right] \\
&= \frac{1}{N_x N_y} \sum_{j=0}^{N_x-1} \left[\sum_{p=0}^{N_y-1} \left(f(X_j, Y_p) e^{-ilY_p} \right) e^{-ikX_j} \right],
\end{aligned} \tag{5.39}
$$

where $X_j = \frac{2\pi j}{N_x}$ and $Y_p = \frac{2\pi p}{N_y}$. Requiring that f is real-valued and even with respect to the lines $x = \pi$ and $y = \pi$ and following the same procedures discussed in Sections 5.1.1 and 5.2.1 simplifies (5.39) and (5.37) to

$$
A_{k,l} \approx \frac{1}{N_x N_y} \left[B_{0,l} + (-1)^k B_{N_x/2,l} + 2 \sum_{j=1}^{N_x/2-1} B_{j,l} \cos\left(\frac{2\pi jk}{N_x} \right) \right], \tag{5.40}
$$

where

$$
B_{j,l} = f(X_j, 0) + (-1)^l f(X_j, \pi) + 2 \sum_{p=1}^{N_y/2-1} f(X_j, Y_p) \cos\left(\frac{2\pi pl}{N_y} \right) \tag{5.41}
$$

and

$$
f(X_j, Y_p) \approx C_{0,p} + (-1)^j C_{N_x/2,p} + 2 \sum_{k=1}^{N_x/2-1} B_{k,p} \cos\left(\frac{2\pi jk}{N_x} \right), \tag{5.42}
$$

where

$$
C_{k,p} = A_{k,0} + (-1)^p A_{k,N_y/2} + 2 \sum_{l=1}^{N_y/2-1} A_{k,l} \cos\left(\frac{2\pi pl}{N_y} \right). \tag{5.43}
$$

Similarly to the 1D case, a function $g(x, y)$ defined on the domain $[0, \pi] \times [0, \pi]$ with the homogeneous Neumann conditions

$$\frac{\partial g}{\partial x}(0, y) = \frac{\partial g}{\partial x}(\pi, y) = \frac{\partial g}{\partial y}(x, 0) = \frac{\partial g}{\partial y}(x, \pi) = 0 \tag{5.44}$$

(i.e., vanishing normal derivatives on the boundary) can be transformed as follows:

$$A_{k,l} \approx \frac{1}{4(M_x - 1)(M_y - 1)} \left[B_{0,l} + (-1)^k B_{M_x - 1,l} + 2 \sum_{j=1}^{M_x - 2} B_{j,l} \cos\left(\frac{\pi j k}{M_x - 1} \right) \right], \tag{5.45}$$

where

$$B_{j,l} = g(X_j, 0) + (-1)^l g(X_j, \pi) + 2 \sum_{p=1}^{M_y - 2} g(X_j, Y_p) \cos\left(\frac{\pi p l}{M_y - 1} \right), \tag{5.46}$$

with $M_x = N_x/2 + 1$ and $M_y = N_y/2 + 1$. The values $g(X_j, Y_p)$ can then be recovered by

$$g(X_j, Y_p) \approx C_{0,p} + (-1)^j C_{M_x - 1,p} + 2 \sum_{k=1}^{M_x - 2} C_{k,p} \cos\left(\frac{\pi j k}{M_x - 1} \right), \tag{5.47}$$

where

$$C_{k,p} = A_{k,0} + (-1)^p A_{k,M_y - 1} + 2 \sum_{l=1}^{M_y - 2} A_{k,l} \cos\left(\frac{\pi p l}{M_y - 1} \right). \tag{5.48}$$

The expressions (5.45) and (5.47) are the 2D DCT-I and its inverse. As for the 1D DCT-I, the 2D DCT-I is nearly its own inverse. Another useful property of the 2D DCT-I is that

it is really a composition of two 1D DCTs. Indeed, letting

$$\mathbf{G} = \begin{pmatrix} g(X_0, Y_0) & g(X_0, Y_1) & \dots & g(X_0, Y_{M_y-1}) \\ g(X_1, Y_0) & g(X_1, Y_1) & \dots & g(X_1, Y_{M_y-1}) \\ \vdots & \vdots & \vdots & \vdots \\ g(X_{M_x-1}, Y_0) & g(X_{M_x-1}, Y_1) & \dots & g(X_{M_x-1}, Y_{M_y-1}) \end{pmatrix}, \tag{5.49}$$

the 2D DCT-I is equivalent to first performing the 1D DCT-I along the rows of $\mathbf{G}$ and then along the columns of the matrix of the resulting coefficients.

If the domain of interest is instead $[-L, L] \times [-L, L]$, the change of variables

$$\tilde{x} = \frac{2L_x}{\pi}\left(x - \frac{\pi}{2}\right), \quad \tilde{y} = \frac{2L_y}{\pi}\left(y - \frac{\pi}{2}\right) \tag{5.50}$$

and the procedure described in Section 5.1.2 leads to the transform

$$\tilde{A}_{k,l} \approx \frac{1}{4(M_x-1)(M_y-1)}\left[\tilde{B}_{0,l} + (-1)^k \tilde{B}_{M_x-1,l} + 2\sum_{j=1}^{M_x-2} \tilde{B}_{j,l} \cos\left(\frac{\pi jk}{M_x-1}\right)\right], \tag{5.51}$$

where

$$\tilde{B}_{j,l} = \tilde{g}(\tilde{X}_j, -L_y) + (-1)^l \tilde{g}(\tilde{X}_j, L_y) + 2\sum_{p=1}^{M_y-2} \tilde{g}(\tilde{X}_j, \tilde{Y}_p) \cos\left(\frac{\pi pl}{M_y-1}\right), \tag{5.52}$$

with $X_j = L_x\left(\frac{2j}{M_x-1} - 1\right)$ and $Y_p = L_y\left(\frac{2p}{M_y-1} - 1\right)$, while the function $\tilde{g}$ can be recovered by

$$\tilde{g}(X_j, Y_p) \approx \tilde{C}_{0,p} + (-1)^j \tilde{C}_{M_x-1,p} + 2\sum_{k=1}^{M_x-2} \tilde{C}_{k,p} \cos\left(\frac{\pi jk}{M_x-1}\right), \tag{5.53}$$

where

$$\tilde{C}_{k,p} = \tilde{A}_{k,0} + (-1)^p \tilde{A}_{k,M_y-1} + 2 \sum_{l=1}^{M_y-2} \tilde{A}_{k,l} \cos\left(\frac{\pi p l}{M_y - 1}\right). \tag{5.54}$$

Finally, the second derivative of $\tilde{g}$ with respect to $\tilde{x}$ at the point (X_j, Y_p) is given by

$$\frac{\partial^2 \tilde{g}}{\partial \tilde{x}^2}(X_j, Y_p) \approx s_x^2 \left[(-M_x - 1)^2 (-1)^j \tilde{C}_{M_x-1,p} + 2 \sum_{k=1}^{M_x-2} -k^2 \tilde{C}_{k,p} \cos\left(\frac{\pi j k}{M_x - 1}\right) \right], \tag{5.55}$$

where the $\tilde{C}$ are defined as in (5.54). Similarly, the second derivative of $\tilde{g}$ with respect to $\tilde{y}$ at the point (X_j, Y_p) is given by (5.53) with

$$\tilde{C}_{k,p} = s_y^2 \left[-(M_y - 1)^2 (-1)^p \tilde{A}_{k,M_y-1} + 2 \sum_{l=1}^{M_y-2} -l^2 \tilde{A}_{k,l} \cos\left(\frac{\pi p l}{M_y - 1}\right) \right]. \tag{5.56}$$

As for the 1D DFT, it is sometimes more convenient to introduce the factors k^2, l^2, s_x^2, and s_y^2 in the coefficients $\tilde{A}_{k,l}$ themselves.

5.2.3. 2D Solver

For concreteness, consider the two-dimensional version of System (3.1). As for the 1D problem, the numerical method consists of a predictor stage and a corrector stage. First, $N_x N_y$ nodes (X_j, Y_p) are chosen such that $X_j = L_x \left(\frac{2j}{N_x - 1} - 1\right)$ and $Y_p = L_y \left(\frac{2p}{N_y - 1} - 1\right)$, with $0 \leq j \leq N_x - 1$, $0 \leq p \leq N_y - 1$, and N_x, N_y odd (preferably of the form $2^n + 1$ for computational reasons; see the discussion of the FFT in Section 5.5). Thus, the nodes (X_0, Y_p) are on the left boundary $x = -L_x$ and the nodes (X_{N_x-1}, Y_p) on the right boundary $x = L_x$. Similarly, the nodes (X_j, Y_0) are on the bottom boundary $y = -L_y$ and the nodes (X_j, Y_{N_y-1}) on the top boundary $y = L_y$. At each time, the values of u at

the nodes, $U_{j,p} = u(X_j, Y_p)$ can be grouped into a matrix $\mathbf{U}$ such that

$$\mathbf{U} = \begin{pmatrix} u(X_0, Y_0) & u(X_0, Y_1) & \dots & u(X_0, Y_{N_y-1}) \\ u(X_1, Y_0) & u(X_1, Y_1) & \dots & u(X_1, Y_{N_y-1}) \\ \vdots & \vdots & \vdots & \vdots \\ u(X_{N_x-1}, Y_0) & u(X_{N_x-1}, Y_1) & \dots & u(X_{N_x-1}, Y_{N_y-1}) \end{pmatrix} \tag{5.57}$$

and, analogously, the values of v at the nodes can be grouped into a matrix $\mathbf{V}$. Using the notation $\mathcal{F}(\mathbf{U})_{k,l}$ to denote the coefficient $\tilde{A}_{k,l}$ of the DCT-I of u (see (5.51)) and taking advantage of the facts that

$$\frac{\partial^2 \mathcal{F}(\mathbf{U}^n)_{k,l}}{\partial x^2} = -s_x^2 k^2 \mathcal{F}(\mathbf{U}^n)_{k,l}, \tag{5.58a}$$

$$\frac{\partial^2 \mathcal{F}(\mathbf{U}^n)_{k,l}}{\partial y^2} = -s_y^2 l^2 \mathcal{F}(\mathbf{U}^n)_{k,l}, \tag{5.58b}$$

the predictor step is

$$\mathcal{F}(\mathbf{U}^{n+1/2})_{k,l} \approx \frac{\mathcal{F}(\mathbf{U}^n)_{kl} + \frac{\Delta t}{2}\mathcal{F}(\mathbf{NLU}^n)_{k,l}}{1 + \frac{\Delta t}{2}(s_x^2 k^2 + s_y^2 l^2)}, \tag{5.59a}$$

$$\mathcal{F}(\mathbf{V}^{n+1/2})_{k,l} \approx \frac{\mathcal{F}(\mathbf{V}^n)_{kl} + \frac{\Delta t}{2}\mathcal{F}(\mathbf{NLV}^n)_{k,l}}{1 + \frac{\Delta t}{2} d_v (s_x^2 k^2 + s_y^2 l^2)}, \tag{5.59b}$$

where

$$\mathbf{NLU}^n = \mathbf{U}^n \circ (\mathbf{1} - \mathbf{U}^n - \alpha \mathbf{V}^n), \tag{5.60a}$$

$$\mathbf{NLV}^n = \mathbf{V}^n \circ (\mathbf{1} - \mathbf{V}^n - \beta \mathbf{U}^n), \tag{5.60b}$$

with the symbol $\circ$ denoting the Hadamard (element-wise) product (i.e., $(\mathbf{A} \circ \mathbf{B})_{k,l} = (\mathbf{A}_{k,l})(B_{k,l})$). The corrector step is

$$\mathcal{F}(\mathbf{U}^{n+1})_{k,l} \approx \frac{[1 - \frac{\Delta t}{2}(s_x^2 k^2 + s_y^2 l^2)]\mathcal{F}(\mathbf{U}^n)_{k,l} + \Delta t \mathcal{F}(\mathbf{NLU}^{n+1/2})_{k,l}}{1 + \frac{\Delta t}{2}(s_x^2 k^2 + s_y^2 l^2)}, \tag{5.61a}$$

$$\mathcal{F}(\mathbf{V}^{n+1})_{k,l} \approx \frac{[1 - \frac{\Delta t}{2} d_v (s_x^2 k^2 + s_y^2 l^2)]\mathcal{F}(\mathbf{U}^n)_{k,l} + \Delta t \mathcal{F}(\mathbf{NLU}^{n+1/2})_{k,l}}{1 + \frac{\Delta t}{2} d_v (s_x^2 k^2 + s_y^2 l^2)}. \tag{5.61b}$$

The method was implemented in Fortran and run in parallel on Quest, Northwestern University's high performance computing cluster, with communication between processes facilitated by the Message Passing Interface (MPI). Routines from the FFTW library [**29**] were used to compute the discrete cosine transforms and their inverses. Table 5.1 summarizes the efficiency of the program with respect to the number of processors.

	Processors		
N	**4**	**8**	**16**
513	5.36	3.03	1.62
1025	26.13	11.08	6.06
2049	99.85	62.85	25.58
4097	371.58	169.81	116.60

Table 5.1. Approximate time (in seconds) required to compute the two-dimensional solution to System (3.6) over 100 time steps on an $N \times N$ grid, including initialization. The initial conditions were the same for all runs.

CHAPTER 6

Two-Species Model and Curvature Advantages

6.1. Strong Interspecies Competition

6.1.1. One Dimension

Consider System (3.1) in one dimension with $\alpha, \beta > 1$, so that the coexistence state b_{uv} is unstable and the single-species states b_u and b_v are stable. Suppose the initial conditions are

$$u(x,0) = 1 - H_0(x), \tag{6.1a}$$

$$v(x,0) = H_0(x), \tag{6.1b}$$

where $H_0(x)$ is the Heaviside function centered at $x = 0$; i.e.,

$$H_0(x) = \begin{cases} 0, & x < 0 \\ 1, & x \geq 0. \end{cases} \tag{6.2}$$

Suppose $d_v = 1$ so that the diffusivities of the species are the same. The only difference in the properties of the species is then the strength of interspecies competition. If $\alpha > \beta$, then u is more susceptible to competition from v than v is from u and the b_v state displaces b_u (i.e., v reaches its carrying capacity across the domain and u goes extinct). On the other hand, if $\beta > \alpha$, b_u displaces b_v. In the special case $\alpha = \beta$, neither species, in general,

dominates the domain (see Section 6.2 for the exception to this general rule). Instead, the solution is a standstill, with neither u nor v expanding its territory. There is, of course, a smoothing of the solution near the interface between the b_u and b_v states due to diffusion, similar to that shown in Figure 6.5.

Similarly, if $\alpha = \beta$ but $d_v > 1$, v has a mobility advantage over u and the b_v state is able to displace the b_u state. Unsurprisingly, if $d_v < 1$, the b_u state displaces b_v. The situation is substantially more complicated if either $d_v < 1$ and $\alpha > \beta$ or $d_v > 1$ and $\alpha < \beta$. In these cases, an advantage in mobility may or may not overcome a disadvantage in direct interspecies competition and there is no clear rule for determining which species dominates. Note also that the above observations still hold when the initial conditions are not symmetric (e.g., if there is initially more of, say, species u in the domain).

6.1.2. Two Dimensions

Predictions of dominance can be even more difficult in two dimensions. Consider System (3.1) in two dimensions with the initial conditions given by

$$u(r, \theta, 0) = 1 - H_{R_0}(r), \tag{6.3a}$$

$$v(r, \theta, 0) = H_{R_0}(r); \tag{6.3b}$$

i.e., a disc of u of radius R_0 surrounded by v (note that $H_{R_0}(r) = H_0(r - R_0)$). Solutions to the analogous 1D problem suggest that if u has an overall advantage over v (due to mobility or competitiveness), the disc should expand until u kills off v and fills the domain, whereas if v has the advantage, the disc should contract (so that u goes extinct). If u and v have identical properties, then the disc should remain at approximately its

original size. It turns out that in this final case, the disc actually contracts, as if v has an advantage. Letting $R(t)$ be the radius of the disc at time t, the linear speed of contraction is approximately $\frac{1}{R(t)}$ for large R (see the end of Section (4.2.1); although b_u is a stable state, the curvature correction is not dependent on the stability of the displaced state), so that the rate of displacement increases as the disc contracts (and when R is no longer large, the correction becomes more extreme; see, e.g., [**21**]). Thus, for two-dimensional problems, there are three ways one species can gain an advantage over the other: direct competition (α vs. β), mobility (d_v), and positioning (curvature). Indeed, in some cases, a curvature advantage can overcome a disadvantage; Figure 6.1 shows the impact of curvature and mobility on the determination of a winner.

It should be noted that the curvature advantages are point-wise advantages; i.e., the local curvature at a point on an interface impacts the propagation speed of that point, rather than of the interface as a whole. For a disc, the interface has the same curvature everywhere, so the disc expands or contracts uniformly. For more complicated interface curves, however, this is not the case. Consider, for example, the initial conditions shown in Figure 6.2a. A section of the interface is curved in such a way that the curve is convex with respect to v (red). Over time, portions of the interface with greater curvature propagate more slowly than the flat portions, causing an overall flattening of the interface (Figure 6.2; for interpretation of this figure and all similar two-species color maps, refer to Table 6.1). On the other hand, if the curved section is initially concave with respect to v (Figure 6.3a), the parts of the interface with greater curvature (in terms of magnitude; note that curvature may be considered negative in the case of a concave curve) propagate more quickly than the flat portions, again causing an overall flattening of the interface (Figure

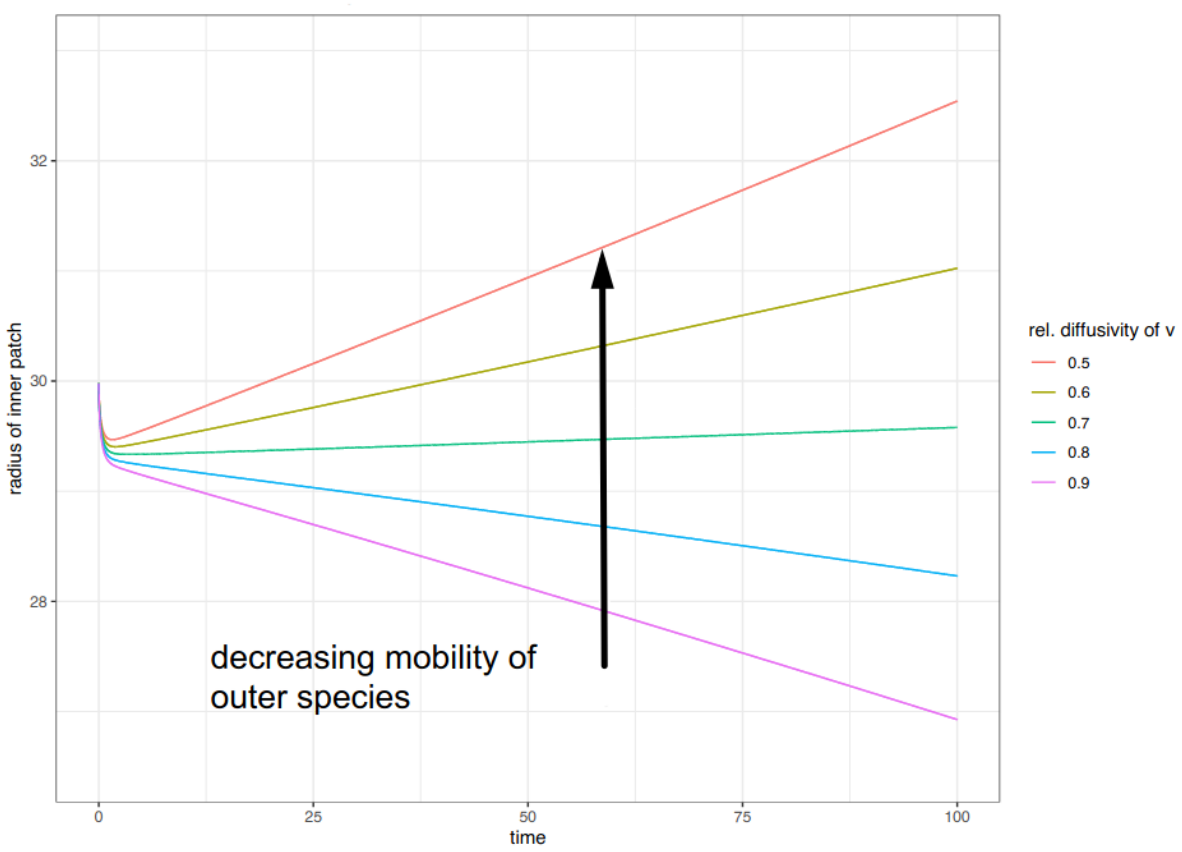

Figure 6.1. Radius of the disc of u over time (initially, a disc of u of radius 30 was surrounded by v). An increase in radius indicates an overall advantage of u, while a decrease indicates an overall disadvantage. The relative diffusivity of v is the parameter d_v. For all runs, $\alpha = \beta = 4$.

6.3). Although the solutions shown in Figures 6.2 and 6.3 are for the case $\beta = 0$, so that v is not impacted by u, the same phenomenon occurs when $\beta > 1$. This choice of β is for the purposes of illustration. Finally, these behaviors have been described for other ecological models [**30**] and for the Potts model [**31**].

Color	State
Black	Strong u Dominance
Dark Gray	Moderate u Dominance
Light Gray	Weak u Dominance
Dark Red	Strong v Dominance
Light Red	Moderate v Dominance
Orange	Weak v Dominance
White	Extinction
Magenta	Coexistence
Cyan	Transition Region

Table 6.1. Color map key for two-species problems. A species is considered to be strongly, moderately, or weakly dominant if its density is at least 0.6, 0.3, or 0.05 greater, respectively, than the density of the other species.

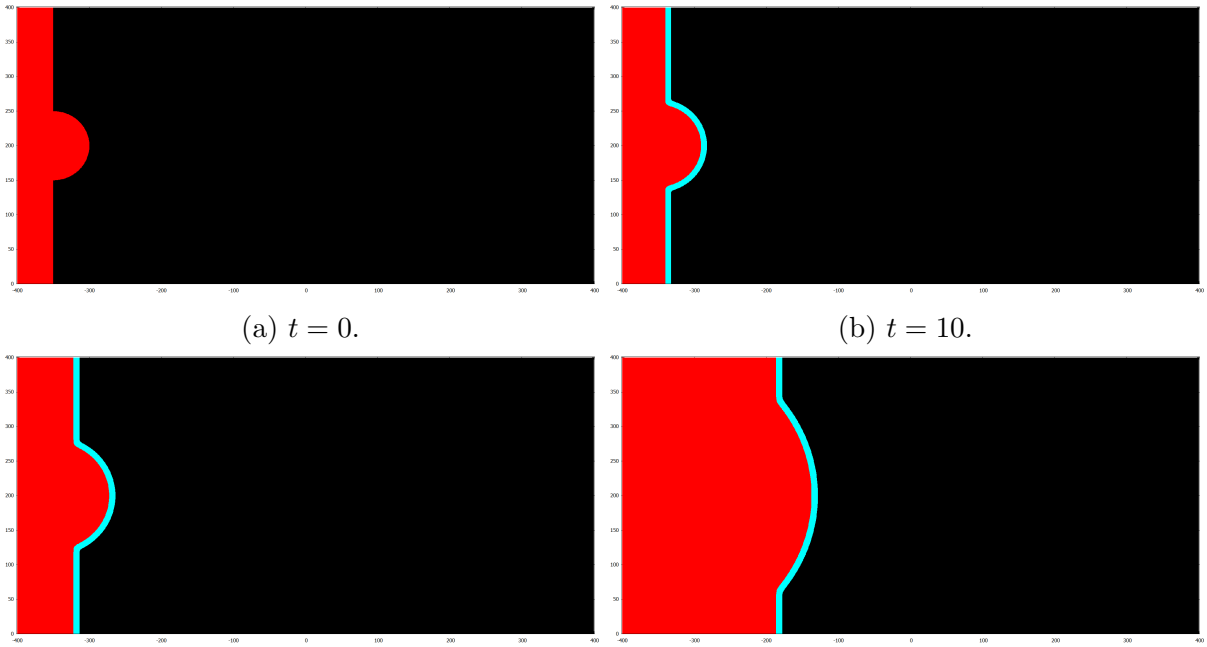

(a) $t = 0$. (b) $t = 10$.

(c) $t = 20$. (d) $t = 90$.

Figure 6.2. Propagation of an interface with a convex curve (with respect to v). Red regions indicate dominance by v, while black regions represent dominance by u (see Table 6.1). Note the flattening of the interface over time.

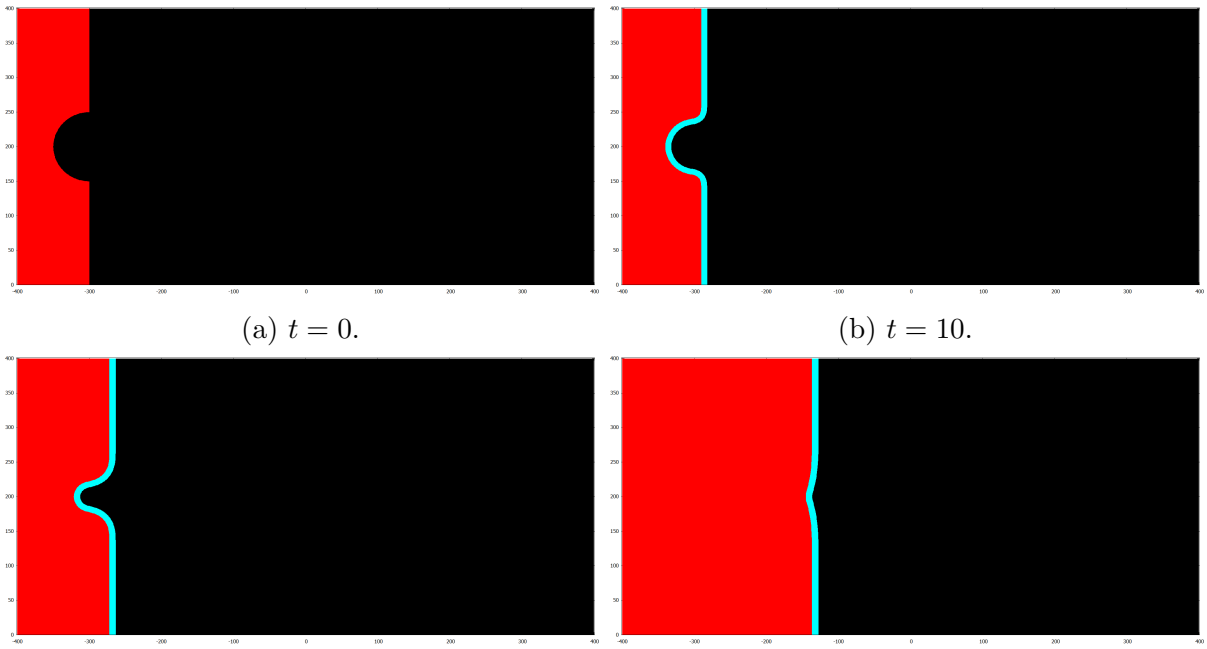

(a) $t = 0$. (b) $t = 10$.

(c) $t = 20$. (d) $t = 90$.

Figure 6.3. Propagation of an interface with a concave curve (with respect to v).

6.1.3. Connection with the Four-Species Model

System (3.15) where all four species have identical properties (referred to as a symmetric system) can be written as

$$\frac{\partial u}{\partial t} = \nabla^2 u + u(1 - u - \alpha v), \tag{6.4a}$$

$$\frac{\partial v}{\partial t} = \nabla^2 v + v(1 - v - \alpha w), \tag{6.4b}$$

$$\frac{\partial w}{\partial t} = \nabla^2 w + w(1 - w - \alpha z), \tag{6.4c}$$

$$\frac{\partial z}{\partial t} = \nabla^2 z + z(1 - z - \alpha u). \tag{6.4d}$$

In the regime $\alpha > 1$, the two-species non-competing states e_{uw} and e_{vz} are stable, while all other states are unstable or unphysical (recall from Section 3.3). In this regime, then, the species are expected to self-segregate into these two states (this happens as long as the species are able to mix), after which the interplay between the e_{uw} and e_{vz} states is analogous to the interplay between the species in the two-species model. Indeed, adding the equation for u to that for w and adding the equation for v to that of z gives

$$\frac{\partial(u+w)}{\partial t} = \nabla^2(u+w) + u(1-u-\alpha v) + w(1-w-\alpha z), \tag{6.5a}$$

$$\frac{\partial(v+z)}{\partial t} = \nabla^2(v+z) + v(1-v-\alpha w) + z(1-z-\alpha u). \tag{6.5b}$$

Since u and w are expected to have the same densities (similarly for v and z), the above becomes

$$2\frac{\partial u}{\partial t} = 2\nabla^2 u + 2u(1-u-\alpha v), \tag{6.6a}$$

$$2\frac{\partial v}{\partial t} = 2\nabla^2 v + 2v(1-v-\alpha u), \tag{6.6b}$$

which, of course, reduces to the two-species problem. Thus, the states e_{uw} and e_{vz} can be treated as directly competing species. In particular, the results in Sections (6.1.1) and (6.1.2) apply to the interactions between these states.

6.2. Non-Unique Coexistence State

The symmetric version of System (3.1) can be written as

$$\frac{\partial u}{\partial t} = \nabla^2 u + u(1 - u - \alpha v), \tag{6.7a}$$

$$\frac{\partial v}{\partial t} = \nabla^2 v + v(1 - v - \alpha u). \tag{6.7b}$$

The coexistence state $b_{uv} = (u_*, v_*)$ satisfies the system

$$u_* + \alpha v_* = 1, \tag{6.8a}$$

$$v_* + \alpha u_* = 1, \tag{6.8b}$$

which, as discussed in Section 3.1, has a unique solution for $\alpha \neq 1$, which is linearly stable for $\alpha < 1$ and unstable for $\alpha > 1$. Conversely, the single-species states b_u and b_v are stable for $\alpha > 1$ and unstable for $\alpha < 1$.

Consider first the one-dimensional problem on the interval $[-50, 50]$ with initial conditions

$$u(x, 0) = 1 - H_b(x), \tag{6.9a}$$

$$v(x, 0) = H_b(x). \tag{6.9b}$$

Taking $b = 40$ results in an initial 9:1 ratio of u to v. If $\alpha = 0.99$, the solution approaches the coexistence state, as expected by the stability analysis. On the other hand, if $\alpha = 1.01$, one could expect the solution to be a standstill, as discussed in Section 6.1. However, this does not occur. Instead, the relative weakness of the interspecies competition combined

with the size of the domain allows for an appreciable amount of species u to diffuse to both boundaries, causing the solution to approach the spatially-homogeneous single-species state b_u (Figure 6.4a; note that if either α or the domain were significantly larger, the solution would be a standstill).

If $\alpha = 1$, System (6.8) does not have a unique solution; i.e., the coexistence state is not unique. Instead, states for which $u + v = 1$ are stable, though not asymptotically so. The solution, therefore, is spatially homogeneous with $u = 0.9$ and $v = 0.1$, so that the ratio of u to v is preserved from the initial conditions (Figure 6.4b). This result holds for other initial ratios (other values of b) as well.

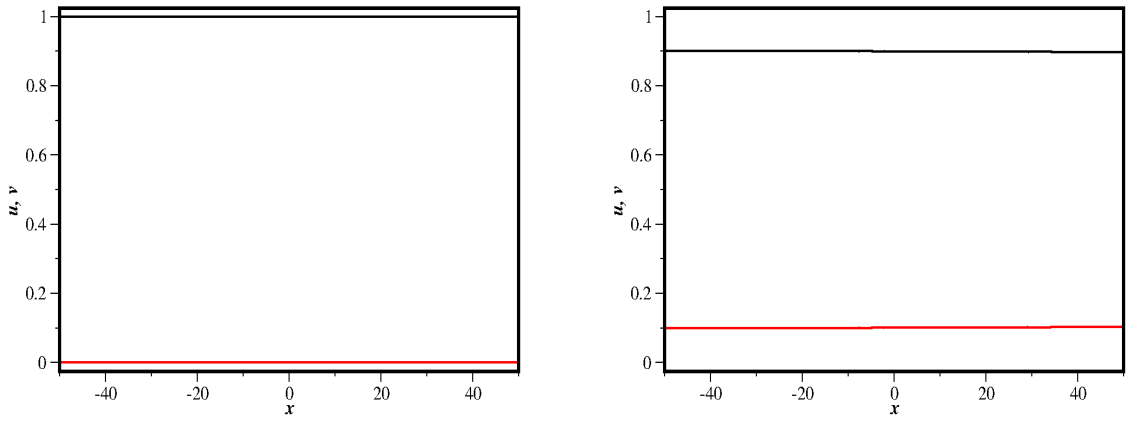

(a) $\alpha = 1.01$. (b) $\alpha = 1$.

Figure 6.4. Solution to System (6.7) at $t = 4800$. Initial conditions given by (6.9) with $b = 40$. Black curves indicate the density of u, while red curves indicate the density of v.

In general, then, for this type of initial condition, it should be expected that taking $\alpha \approx 1$ leads to a spatially homogeneous solution, with $\alpha = 0.99$ leading to the coexistence state, $\alpha = 1$ leading to a state consistent with the initial ratios of the species, and $\alpha = 1.01$

leading to a single-species state (assuming a suitably small domain), with the dominant species determined by the initial conditions. The obvious exception to this general point about $\alpha = 1.01$ is the case where $b = 0$. Here, the solution is a standstill (Figure 6.5). However, taking $\alpha = 1$ in this case leads to the expected solution $u(x,t) = v(x,t) = 0.5$.

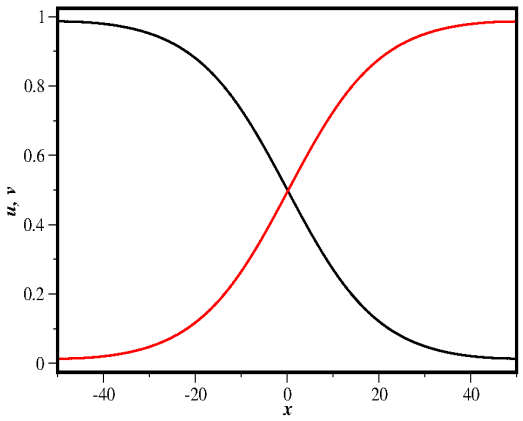

Figure 6.5. Solution at $t = 4800$ for $\alpha = 1.01$ and $b = 0$, illustrating a standstill.

Now, consider the two-dimensional problem on the domain $[-50, 50] \times [-50, 50]$ with initial conditions

(6.10a) $$u(r, \theta, 0) = H_{R_0},$$

(6.10b) $$v(r, \theta, 0) = 1 - H_{R_0}.$$

As in the 1D case, taking $\alpha = 0.99$ and any choice of R_0 leads to a spatially homogeneous solution that approaches the coexistence state. Additionally, taking $\alpha = 1$ leads to a spatially homogeneous solution respecting the criterion $u + v = 1$, with the ratio of u to v determined by the initial condition. In particular, taking $R_0 = R_* = 5000/\pi$ (so

that the area initially covered by v is equal to the area initially covered by u) leads to the solution $u(x,t) = v(x,t) = 0.5$. Thus, it can reasonably be said that curvature does not have an impact on the steady-state solution when $\alpha \leq 1$. However, it does have a significant impact on the transient behavior of the solution. Consider, for example, the initial condition shown in Figure 6.6a, in which the curvature of the species-species interface is positive (with respect to v) at some points and negative at others. As discussed in Section 6.1.2 for stronger interspecies competition, there is a flattening of the interface (although the "interface" is somewhat ill-defined) during the approach to the spatially homogeneous steady state (Figure 6.6b).

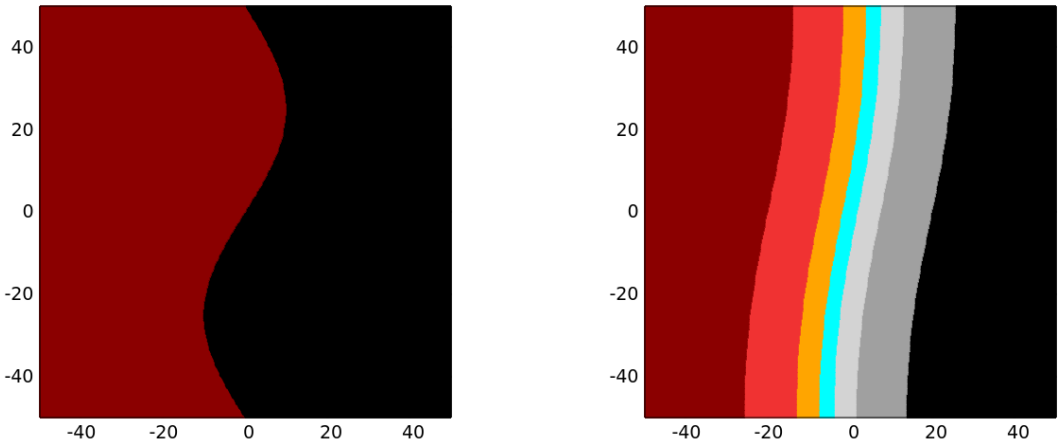

(a) $t = 0$. (b) $t = 400$.

Figure 6.6. Initial condition and transient solution for $\alpha = 1$.

On the other hand, taking $\alpha = 1.01$ and the initial conditions (6.10) with $R_0 = R_*$ leads to different solution behavior than what would be expected for the analogous planar problem. Based on the 1D results, the argument could be made that virtually nothing should happen, since the initial ratio of u to v is 1:1. Instead, the disc of v collapses

(Figure 6.7) and the solution approaches the spatially homogeneous single-species state b_u, as occurs for larger values of α (recall Section 6.1.2).

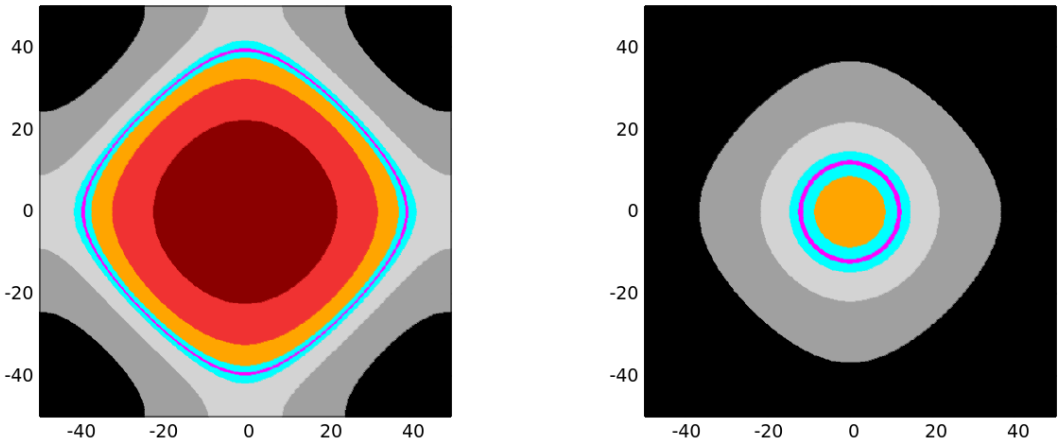

(a) $t = 300$. (b) $t = 1000$.

Figure 6.7. Transient solution for $\alpha = 1.01$ with $R_0 = R_*$.

CHAPTER 7

Introduction to Ordered and Disordered Behavior in RPS Systems

Note: much of the content in Chapters 7 through 11 was co-authored by A. Bayliss and V. A. Volpert and published in [**32**]. *Used with permission.*

In Chapters 7 through 11, the three-species RPS system (3.6) is analyzed to discern the conditions that lead to ordered versus disordered solution behavior. As discussed in Section 2.2.1, parameters appropriate for a model of a community of *E. coli* variants (call the variants u, v, and w) are chosen, so that the spatiotemporal patterns found may be experimentally observable.

As described in Section 2.1.1, two behaviors have been observed in spatially homogeneous experiments. In some cases, there is a time interval during which one species is dominant, followed by an interval for which its controlling species is dominant, and so on, with the cycle repeating for some time. In other cases, the system settles to a state in which only one species is detectable. When there is spatial dependence, single-species patches chase each other according to the RPS sequence (i.e., w chases v, v chases u, and u chases w). While the observed dynamics have not been analyzed in detail, no regular spatiotemporal structures were reported in the patch behavior [**3**].

Three-species cyclic ecosystems have been previously modeled using stochastic game theory on both a lattice [**33, 34, 35**] and on a continuous interval [**36**]. PDE models

have been derived from a stochastic game and shown to allow for spiral solutions in two dimensions [**35, 37, 38, 39, 40**], many of which account for effects on a species by both of the other species (e.g., u is affected by v and w). The fully deterministic model (3.6) was shown to reproduce some reported observations [**16**]; in particular, for certain parameter regimes, the system admits an asymptotically stable heteroclinic cycle among the three single-species states c_u, c_v, and c_w, modeling periods of dominance by each species in turn, as well as traveling waves in which single-species patches chase each other in the RPS sequence. Since the inclusion of stochastic effects, interspecies overcrowding, and predation is not necessary to describe the dynamics reported in the relevant ecological literature, System (3.6) is a suitable (and relatively simple) model to employ.

The focus in the following chapters is to analyze the nonlinear dynamics of RPS schemes; in particular, to demonstrate that several ordered solutions to System (3.6) exist in both 1D and 2D, and to determine and describe the mechanisms that lead to ordered as opposed to disordered structures. The 1D model represents an ecosystem confined to a ring (realistically, a thin annulus; e.g., the region near the walls of petri dish), while the 2D model represents an ecosystem in a petri dish. Thus, the 1D system is considered on the interval $[-L, L]$ with periodic boundary conditions (since the ecosystem should be thought of as being on a circle), while the 2D system is considered on the square $[-L, L] \times [-L, L]$ with no-flux boundary conditions (since there should be no movement of the species into or out of the petri dish). The boundary conditions are automatically enforced by the numerical methods used to solve the systems (see Chapter 5). Note also that although square petri dishes do exist, the square domain is largely chosen for

convenience; general solution behaviors are largely unaffected by the shape of the domain (there is, of course, some distortion near the boundary).

In the following chapters, the interaction parameters α, β, and γ are chosen such that

$$\alpha, \beta, \gamma > 2, \tag{7.1}$$

so that the two-species equilibria c_{uv}, c_{uw}, and c_{vw} are not physical, while the coexistence state c_{uvw} is always physical, but unstable. Under this assumption, the heteroclinic cycle $c_u \to c_v \to c_w \to c_u$ is asymptotically stable (see Section 3.2).

The mechanisms leading to ordered and disordered solutions to System (3.6) in the unstable coexistence regime are not well understood, though experimental observations strongly suggest that the *E. coli* system does operate in this regime, since stationary coexistence of the variants has not been reported in the ecological literature. Previous computational results have shown that spatiotemporal chaos can occur in this regime [**16**]. Spatiotemporal chaos has also been found numerically for systems of competing species [**41, 42, 43**], predator-prey systems [**44**], cyclic systems with five species [**20**], and various other ecological systems [**45**]. Nevertheless, ordered spatiotemporal patterns have also been shown computationally in some cases. A simple ordered structure occurs in 1D with periodic boundary conditions. If all diffusivities are equal and the initial conditions are just three equal patches of the individual species, then it has been shown that if the domain size is sufficiently large, the patch array will propagate rigidly in the RPS order with speed close to $2\sqrt{d}$, where the common diffusivity is d, provided that the patches are sufficiently wide [**16, 46**] (the pattern fails to persist if one of the patches is thin enough that diffusive leakage of the other two species brings substantial

amounts of the three species together, leading to the destruction of the patch's integrity). However, this pattern, while stable [**46**], is primarily a result of the spatial structure of the initial conditions (i.e., the species are initially separated). Computations in the regime of unstable coexistence that do not have such an initial spatial structure often devolve into spatiotemporal chaos for RPS systems, as well as for systems with more than three species [**20, 16**], consistent with the computations for other ecological systems referenced above.

Although chaotic behavior has been observed in competitive models, the actual causes of the chaos have not been previously determined. Thus, a primary focus of the following chapters is to provide support to the proposition that a mechanism for the onset of chaos is repeated patch splitting due to diffusion of competitors when a patch is sufficiently large. Other major findings include:

(1) Chaos tends to occur when interspecies competition is generally weak, while ordered patterns are favored when interspecies competition is strong, due to the ability of the species to self-segregate.

(2) Breather modes, where patches expand and contract in an ordered periodic fashion, can be found in some parameter regimes. Similar modes were found in [**40**] in a different context. For other choices of parameters, an asymmetric traveling array of single-species patches can be found (i.e., patches with different widths propagate rigidly).

(3) For fixed parameters, different initial conditions can lead to different steady-state behaviors.

(4) The associated ODE system (with appropriate initial conditions) can often be used to predict whether the solution to the PDE system is ordered or not.

(5) In 2D, spiral solutions are predominant. Different types of spiral structures can form, depending on the parameters and initial conditions.

CHAPTER 8

Solution Behavior for 1D Symmetric RPS Systems

8.1. System Setup and Discussion

Consider the one-dimensional symmetric version of System (3.6) on the domain $[-L, L]$; i.e.,

$$\frac{\partial u}{\partial t} = \frac{\partial^2 u}{\partial x^2} + u(1 - u - \sigma v), \tag{8.1a}$$

$$\frac{\partial v}{\partial t} = \frac{\partial^2 v}{\partial x^2} + v(1 - v - \sigma w), \tag{8.1b}$$

$$\frac{\partial w}{\partial t} = \frac{\partial^2 w}{\partial x^2} + w(1 - w - \sigma u), \tag{8.1c}$$

so that $d_v = d_w = 1$, $u_* = v_* = w_* = A$, and $\alpha = \beta = \gamma = \sigma = \frac{1-A}{A}$. The coexistence state $(u_*, v_*, w_*) = (A, A, A)$ is unstable if $A < A_* = 1/3$ (equivalently, $\sigma > \sigma_* = 2$). The only way to distinguish the three species is by the initial conditions and the model depends on only two parameters: A (or σ) and L. The majority of the results that follow are for $L = 60$, appropriate for bacterial colonies in liquid media, but larger values of L, appropriate for colonies in agar, are also considered (see Section 2.2.1). Note that as A decreases from A_*, σ increases from σ_*. Thus, interspecies competition increases as A decreases, making it more difficult for different species to cohabit a region. In general, strong interspecies competition promotes ordered states, while weaker interspecies

competition promotes chaos. In all cases, of course, the interspecies competition coefficient σ is larger than the intraspecies competition coefficient (normalized to unity).

All 1D computations were run with either mixed or patch initial conditions. The mixed conditions were taken to be perturbations of the unstable coexistence state c_{uvw}, so that all three species were initially present throughout the domain. For patch initial conditions, there was no initial cohabitation; rather, each species was contained in its own patch, though mixing immediately occurs to a small degree due to diffusion. The general form of the mixed initial conditions is

$$u(0,x) = \left(1 + \eta u_0 + \varepsilon \cos^n\left(\frac{m\pi x}{L}\right)\right) A, \tag{8.2a}$$

$$v(0,x) = \left(1 + \eta v_0 + \varepsilon \cos^n\left(\frac{m\pi x}{L} + \frac{2\pi}{\delta}\right)\right) A, \tag{8.2b}$$

$$w(0,x) = \left(1 + \eta w_0 + \varepsilon \cos^n\left(\frac{m\pi x}{L} + \frac{4\pi}{\delta}\right)\right) A, \tag{8.2c}$$

where $m = n = 1$, $\eta = \varepsilon = 0.3$, and $\delta = 3$, unless otherwise stated. These mixed conditions are symmetric in the mean if and only if $u_0 = v_0 = w_0$ or $\eta = 0$. Patch initial conditions always consist of three single-species patches (one of each species), with the degree of asymmetry quantified by the parameter R, the ratio of the width of the widest patch to that of the thinnest patch. The initial patch array is always chosen so that the patches of v and w are equal in extent, while the patch of u, surrounded by the other two patches, may be thinner. Patch initial conditions are symmetric if and only if $R = 1$. It is shown below that symmetry in the initial conditions (or the lack thereof) can be important in the ultimate evolution of the solution.

The principal results that have been found are as follows:

(1) For all mixed initial conditions, clusters dominated by an individual species are rapidly formed (referred to as self-segregation). Clusters that do not include significant quantities of the other two species are called patches. In order to be considered a patch, the dominant species must have a density of at least 0.9.

(2) Some solutions exhibit spatiotemporal chaos and, in some cases, this chaos is transitory. There are many examples where the chaos persists for an extremely long time (especially with respect to any realistic experimental timescale); however, it is unclear whether or not chaotic behavior always eventually terminates. In a chaotic solution, clusters form over the entire domain. When a cluster is surrounded by controlling clusters (e.g., a cluster of u surrounded by clusters of v), it is subsequently eliminated (referred to as coarsening). The transition from chaotic to laminar behavior always occurs when coarsening occurs more rapidly than clusters are generated. When chaotic behavior terminates, the solution is reduced to a spatially homogeneous heteroclinic cycle.

(3) Symmetric traveling waves (TW), consisting of single-species patches of equal extent propagating around the domain, are found in some cases. This type of solution has been found for more general models allowing for competitive effects on a species by both of the remaining species [**37, 43**] and the stability properties of these solutions were analyzed in [**46**]. Additionally, this solution behavior was observed for the present model in [**16**]. Such solutions can only be obtained with symmetric or near-symmetric initial conditions (i.e., symmetry in the mean for mixed initial conditions or $R \approx 1$ for patch initial conditions).

(4) Solutions can exhibit pseudo asymmetric traveling waves ($PATW$). For these solutions, there is an asymmetric patch array (consisting of three patches of different widths) that propagates nearly rigidly. The term "pseudo" is used because computations indicate there can be very slow changes in patch widths over very long times (of the order 10^5 units of time, corresponding to roughly 3.8 years of physical time - substantially larger than reported observations of relevant bacterial communities). These changes are usually not noticeable graphically, though they are apparent through detailed analysis of the numerical data.

(5) Solutions can be "breathers." These solutions are characterized by propagating patches that expand and contract in succession. The breathing can be periodic in time, in which case they are steady-state breathers. When the breathing is not periodic, the breathers are transitory, and the ratio of an expanded patch to a compressed patch increases over time. Transitory breathers ultimately evolve to chaotic solutions, while steady-state breathers are ordered states (they are modulated traveling waves).

(6) Patch splitting results in the onset of chaos. Consider a three-patch array with a wide patch of u and a thin patch of w. For any patch, there is always diffusion from the neighboring patches to some extent, so that v diffuses through the trailing edge of the patch of u, while w back-diffuses through the leading edge of the patch of u. If the patch of w is sufficiently thin, there can also be back-diffusion of v through the patch of w and into the leading edge of the patch of u. Thus, the controlling species v enters the patch of u from both edges. There

is then a reinforcement of v within the patch of u, resulting in the patch being split by a growth of v.

(7) In general, chaos is more prevalent for large A (near A_*) than for small A due to the role of interspecies competition. When A is large, interspecies competition is relatively weak and patch splitting predominates, leading to a transition to chaos. On the other hand, when A is small, interspecies competition is strong, making self-segregation of the species likely. In this case, ordered solutions are favored.

8.2. ODE System

The system of ODEs associated with the PDE system (8.1) is

$$\frac{du}{dt} = u(1 - u - \sigma v), \tag{8.3a}$$

$$\frac{dv}{dt} = v(1 - v - \sigma w), \tag{8.3b}$$

$$\frac{dw}{dt} = w(1 - w - \sigma u). \tag{8.3c}$$

Consider this system with the initial conditions

$$u(0) = (1 + \varepsilon)A, \tag{8.4a}$$

$$v(0) = \left(1 - \frac{\varepsilon}{2}\right) A, \tag{8.4b}$$

$$w(0) = \left(1 - \frac{\varepsilon}{2}\right) A, \tag{8.4c}$$

where $\varepsilon = 0.3$ and $A = \frac{1-\sigma}{\sigma}$, as usual. The solution for $A = 0.3$ ($\sigma \approx 2.33$) is shown in Figure 8.1a. In the figures presented throughout, the basic color scheme of black for u, red

for v, and green for w is employed. The species will often be referred to by these colors, for clarity. In Figure 8.1b, the time intervals for which the trajectory is in a neighborhood of the c_u state are shown. The trajectory is considered to be in this neighborhood when $u > 0.99999$.

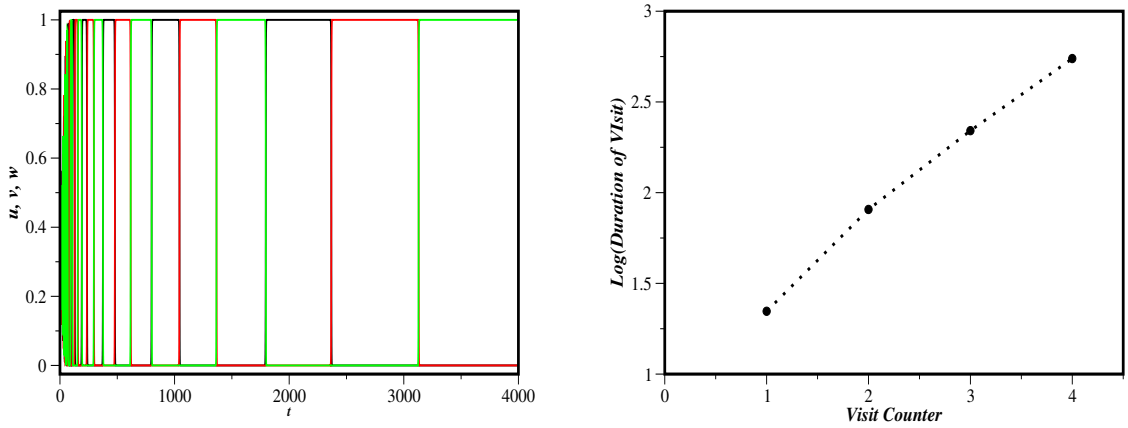

(a) (b)

Figure 8.1. (a) ODE solution for $A = 0.3$ and the initial conditions (8.4). Black, red, and green curves represent the densities of u, v, and w, respectively. Data at early times has been excluded. (b) Lengths of intervals where the trajectory is near the c_u equilibrium state. The vertical axis is the log (base 10) of visit duration, resulting in a roughly linear dependence on visit number. Visits are marked by points; the dotted connections are present to show the linear relationship.

This is a typical solution (a heteroclinic cycle) for the ODE system in the regime of unstable coexistence (in the regime of stable coexistence, the solution generally approaches the coexistence state). The solution can be described as follows:

(1) One species dominates for an interval of time until it is displaced by its controlling species - w displaces v (green displaces red), v displaces u (red displaces black), and u displaces w (black displaces green) (Figure 8.1a).

(2) These intervals become progressively longer as the trajectory gets closer to one of the single-species saddles; i.e., the duration of successive visits increases. More specifically, the log of the visit duration is a roughly linear function of the visit number (Figure 8.1b).

(3) While not readily discernible from the figures, as the trajectory moves closer to any one saddle (say, c_u), the two non-dominant species (v and w, in this case) get progressively closer to zero.

Points 1 and 2 describe ecological ramifications of ODE solutions. Point 1 is fully consistent with observations of variants *E. coli* and variants of side-blotched lizards [**3, 7**] (see Section 2.1). On the other hand, Point 2 has not been observed in ecological systems, at least based on published data. Indeed, such long observations may not be feasible; moreover, the property of progressively longer visits is inhibited by noise, as is demonstrated below.

Point 3 means that there is a limit to how long a trajectory approaching a heteroclinic cycle can be computed, which has significant computational ramifications. There are limits to how close a floating-point number of fixed precision can get to zero. Any computation of a heteroclinic cycle will inevitably fail when the trajectory is sufficiently close to one of the single-species states. If nothing is done, the final state will be a single-species state (mathematically unstable, as discussed in Section 3.2, but computationally stable

under these conditions). It is also possible that for sufficiently small numbers, discretization and roundoff errors will dominate the number. However, discretization and roundoff errors typically decrease when a trajectory approaches a single-species state. More importantly, such behavior is not accurate from an ecological perspective, since the continuum approximation for population densities is not valid at sufficiently small densities.

The issue from Point 3 can be addressed in a number of ways:

(1) Do nothing. In this case, the solution for some species will hit machine zero, there will be no further changes, and the computation will incorrectly predict one unstable single-species state as the steady state. The accuracy of computations of trajectories approaching a stable heteroclinic cycle can be improved by writing System (8.3) in terms of logs of the dependent variables [**16**]. In fact, this procedure was used to generate Figure 8.1a. However, the computed heteroclinic cycle will still terminate at some point and the issue that the continuum approximation is not valid at such low densities is not resolved. Furthermore, an effective way to implement this procedure remains elusive for the PDE system. The transformation to logs introduces a nonlinear coefficient in each diffusion term, thereby making semi-implicit temporal integration much more expensive.

(2) Introduce a cutoff variable u_c and set species densities to zero when they fall below u_c. This procedure also predicts an unstable single-species state as the ultimate steady state, but gives control over the cutoff, unlike in the previous method, where the final state is determined by computer hardware and compiler design.

(3) Introduce a floor u_f and set species densities to u_f when they fall below that value. Thus, none of the densities are ever zero, so the computation never terminates with an unstable single-species state. The effect of this procedure is shown in Figure 8.2a (solid black curve) with $u_f = 1 \times 10^{-20}$. For comparison, Figure 8.2a also includes the results from the computation that generated Figure 8.1a (thick cyan curve), illustrating the differences from a trajectory approaching the heteroclinic cycle without any control over low densities. The solution is now clearly periodic. Handling low-level densities in this way converts the heteroclinic cycle into a limit cycle. Note that u_f (or u_c in the previous method) can be chosen such that the minimum density is consistent with reasonable carrying capacities, thus addressing the issue with the continuum approximation.

(4) Introduce low-level additive noise, so that after every time step, each density is subject to noise of the form $\Delta t \varepsilon_n r$, where Δt is the time step size, ε_n is a specified magnitude, and r is a random number varying between ± 1. This works similarly to the floor, as effectively no species can remain at zero for a substantial amount of time. Figure 8.2a also shows u for a computation with noise (dotted curve the figure) with $\Delta t \varepsilon_n = 1 \times 10^{-20}$. The result with noise is what has been termed a "statistical limit cycle," and it appears from the figure that its average period is very close to the period of the limit cycle obtained using a floor, provided $u_f = \Delta t \varepsilon_n$.

Noise has been identified as a mechanism to prevent infinitely long intervals of residence near a saddle for systems with an attracting heteroclinic cycle [**47**]. The average period for a noise-induced statistical limit cycle in the case when

the noise-free problem has an attracting heteroclinic cyle has been shown to scale linearly with the magnitude of the log of the noise amplitude [**48**]. Instead of the period, consider the durations of visits of the trajectory to the neighborhood of the c_u saddle, as described above. Figure 8.2b shows the average visit duration against $\log(\Delta t \varepsilon_n)$ for a computation with noise (black circles) and the average visit duration against $\log(u_f)$ for a computation with a floor (cyan crosses). The results show good agreement with the theoretical noise scaling, as well as agreement between the visit durations for the floor limit cycle and the statistical limit cycle over almost 20 orders of magnitude. Thus, the floor and additive noise procedures (on average) give very similar results, provided the floor and noise level are comparable. Large amplitude effects on the solution have also been observed when the noise was such that trajectories could leave an invariant space [**49**] (in this case, the physical space $u, v, w \geq 0$); however, no species density is allowed to become negative due to the noise, so no $O(1)$ amplitude effects are observed.

All PDE computations make use of a floor (method 3) to deal with small densities, since this (i) allows the computations to be fully deterministic, (ii) reproduces behavior reported in spatially homogeneous ecological systems, (iii) is consistent with the idea of a minimum density, and (iv) does not admit bias toward any particular species in symmetric systems (as in method 2).

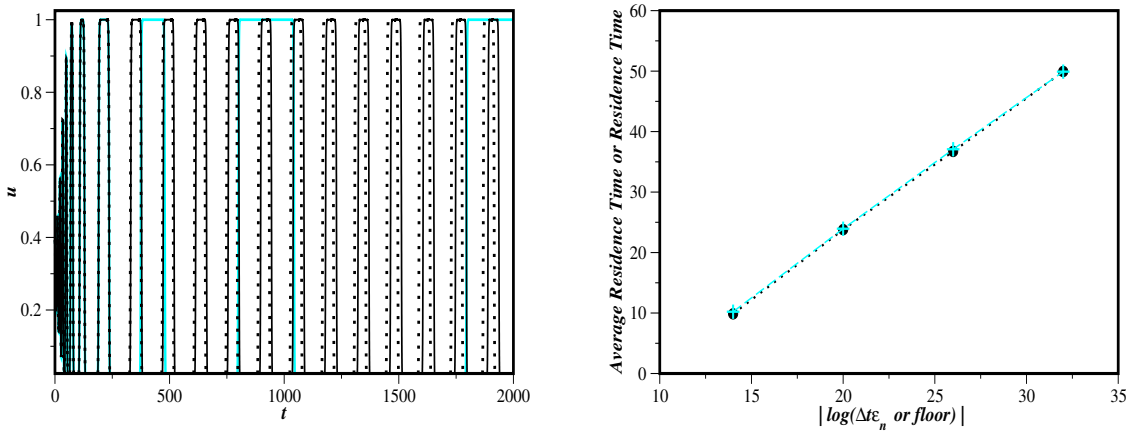

(a) (b)

Figure 8.2. (a) ODE solution (u only) for $A = 0.3$ and the initial conditions (8.4) computed with a floor ($u_f = 1 \times 10^{-20}$, solid black curve) and with additive noise ($\Delta t \varepsilon_n = 1 \times 10^{-20}$, dotted curve). The thick cyan curve is the solution shown in Figure 8.1a. (b) Average residence times of the trajectory near the c_u state for a computation with a floor (cyan crosses) and for a computation with noise (black circles). For visualization purposes, the data points are connected by dots and dashes.

8.3. Illustrations of 1D Solution Behavior

In this section, one-dimensional solution behaviors are illustrated and described in detail.

8.3.1. Chaos

Consider System (8.1) where $A = 0.3$ ($\sigma \approx 2.33$) with the mixed initial conditions (8.2), where $(u_0, v_0, w_0) = (1.4, 1, 0.6)$. Figure 8.3 shows the solution at $t = 700$ (solid curves), $t = 701$ (dotted curves), and $t = 702$ (dashed curves). Note that the time $t = 700$ corresponds to a physical time of approximately 10 days. All three species exhibit spatial

oscillations; however, there is no apparent order to these oscillations. In fact, the most positive Lyapunov exponent, estimated numerically by the method discussed in [**50**], is greater than zero, indicating that the solution is indeed chaotic. For the same parameters except with $A = 0.34$ (so that the coexistence state is stable), there is no positive Lyapunov exponent and the solution simply approaches the stable coexistence state. Similar solutions have been computed by others from comparable models [**38, 43**].

Despite the disordered nature of the solution, and the very significant changes over short periods of time, the solution still respects the RPS dynamics; i.e., there should be (and is) some predictable behavior within the disordered structure. The organizing principles for RPS dynamics are very simple - each species tries to eliminate its victim species and is eliminated by its controlling species. These principles are manifested for the solution shown in Figure 8.3 in two ways: the motions of clusters of a species toward clusters of the victim species and the rise of a species initially at low levels when it is surrounded by its victim species (coinciding with the decline of the victim species). The figure shows four clear examples of the former behavior, while the latter behavior is shown in the regions labeled $R1$, $R2$, and $R3$. The results indicate that RPS-dictated motions, when combined with disordered spatial profiles, can sustain chaotic behavior. The mechanism leading to chaos is patch splitting, described in detail in Section 8.3.4.

Over the time period considered in the figure, none of the species are ever essentially eliminated; i.e., all three species coexist at all spatial points, allowing for the RPS interactions illustrated in the figure. For this value of A, interspecies competition is weak enough that the species cannot self-segregate. Because of this, it is more appropriate to refer to regions where a species dominates as clusters, rather than patches. Moreover,

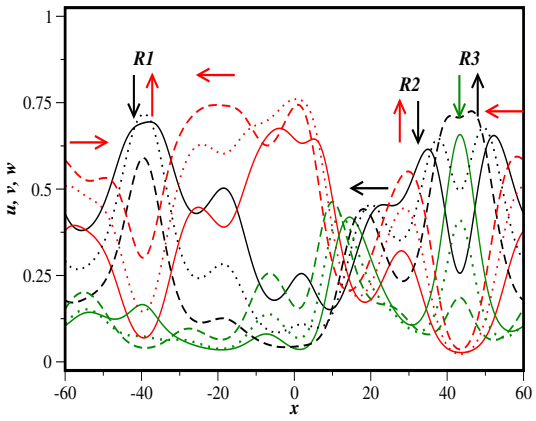

Figure 8.3. Solution at $t = 700$ (solid curves), $t = 701$ (dotted curves), and $t = 702$ (dashed curves) as a function of x. Parameters given in the text. The labels indicate regions where RPS motions are apparent.

it should be noted that this solution remains chaotic for a very long time, though it is unclear whether it eventually collapses into a spatially-homogeneous solution. For smaller values of A, chaos often collapses within a reasonable amount of time (see Section 8.3.4). Chaotic solutions can also be computed from other mixed initial conditions, as well as from patch conditions (see Table 9.1).

Finally, letting $\bar{u}(t)$, $\bar{v}(t)$, and $\bar{w}(t)$ be the spatial means of the mass fractions of u, v, and w, respectively (henceforth referred to as the species fractions); i.e.,

$$\bar{u}(t) = \frac{1}{\overline{uvw}(t)} \int_{-L}^{L} u(t,x)\,dx, \tag{8.5a}$$

$$\bar{v}(t) = \frac{1}{\overline{uvw}(t)} \int_{-L}^{L} v(t,x)\,dx, \tag{8.5b}$$

$$\bar{w}(t) = \frac{1}{\overline{uvw}(t)} \int_{-L}^{L} w(t,x)\,dx, \tag{8.5c}$$

where

$$\overline{uvw}(t) = \int_{-L}^{L} u(t,x) + v(t,x) + w(t,x)\,dx, \tag{8.6}$$

and then finding the temporal averages

$$E[\bar{u}(t)] = \frac{1}{t_2 - t_1}\int_{t_1}^{t_2} \bar{u}(t)\,dt, \tag{8.7a}$$

$$E[\bar{v}(t)] = \frac{1}{t_2 - t_1}\int_{t_1}^{t_2} \bar{v}(t)\,dt, \tag{8.7b}$$

$$E[\bar{w}(t)] = \frac{1}{t_2 - t_1}\int_{t_1}^{t_2} \bar{w}(t)\,dt \tag{8.7c}$$

with $t_1 = 500$ and $t_2 = 700$ reveals that $E[\bar{u}(t)] \approx E[\bar{v}(t)] \approx E[\bar{w}(t)] \approx 1/3$ to a very close approximation, so that on average (in space and time), the three species are close to being evenly distributed.

8.3.2. Patch Traveling Waves

Here, two types of patch traveling waves are illustrated: (i) symmetric traveling waves (TW) where there are three patches of equal width (as described in, e.g., [**16**], [**37**], and [**46**]) and (ii) pseudo asymmetric traveling waves ($PATW$), where the widths of the patches differ, but propagation is still rigid to a close approximation over the time intervals considered.

For $L = 60$ and larger, symmetric traveling waves are always found when using symmetric patch initial conditions ($R = 1$), provided that A is sufficiently small, which is consistent with the stability analysis in [**46**]. However, if A is too large (close to A_*), chaotic solutions are found instead. For larger domains, symmetric traveling waves with

larger A may, in fact, be stable, since chaos arises when the patches are too thin and interspecies competition is too weak to prevent the three species from accumulating within a patch, thus destroying the integrity of the patch. Furthermore, for sufficiently small A (e.g., $A = 0.215$ for $L = 60$), symmetric patch traveling waves can arise from mixed initial conditions, provided the conditions are symmetric in the mean. Conversely, symmetric patch traveling waves never arise from asymmetric patch initial conditions ($R > 1$) or from mixed conditions that are not symmetric in the mean.

Consider the mixed initial conditions with $A = 0.215$, $\delta = 3$, and $\eta = 0$, which are symmetric in the mean. After a brief transient, during which the species self-segregate due to the strength of interspecies competition, the solution consists of three rigidly-propagating patches. The solution at $t = 4000$ is shown in Figure 8.4a (dotted curves), with the direction of propagation indicated. The species chase each other in the RPS order; i.e., u (black) chases w (green), w chases v (red), and v chases u. The same solution can be computed from symmetric patch initial conditions. Symmetric patch traveling waves are computationally stable when interspecies competition is sufficiently strong, with the required strength dependent on L, in agreement with previous results [**37, 43**]. Specifically, lengthening the domain allows for stable traveling wave solutions with weaker interspecies competition. Assuming the domain is long enough to allow for substantial separation of the species-species interfaces (as is the case for $L \geq 60$), the patches propagate with speed $s \approx 2$, as predicted by the analysis described in Section 4.2.1 (note also the connection to the Fisher-KPP equation). Note that it is only possible to compute a truly symmetric traveling wave using the method described in Section 5.1.3 if the number of grid points is divisible by 3. This was generally not the case, since the

FFT implementation used is most efficient when the number of grid points is a power of 2; however, the grids were sufficiently fine that symmetric traveling waves could be computed within discretization error.

Now, consider the asymmetric mixed initial conditions with $(u_0, v_0, w_0) = (1.02, 1, 0.98)$, $\eta = 0.3$, and all other parameters the same as above. The solution is shown in Figure 8.4a (solid curves). The array is noticeably no longer symmetric. For these initial conditions, the red patch has expanded at the expense of the green and black patches. $PATW$ solutions can also be found using asymmetric patch initial conditions.

The computed patch widths for the symmetric TW (dashed and dotted curves), the $PATW$ from mixed initial conditions (solid curves), and the $PATW$ from patch initial conditions with $R \approx 1.038$ (solid curves with circles) are shown in Figure 8.4b. The patch widths are computed for species u by determining the spatial extent for which $u \geq 0.9$. As previously mentioned, the patch widths are not perfectly steady over very long periods of time (much longer than what is shown in the figure). For realistic ecological timescales, however, it is clear from the figure that propagation of the array can be treated as rigid.

Figure 8.4c compares the means of the $PATW$ from mixed initial conditions (solid curves) to those of the symmetric TW from mixed initial conditions (dashed and dotted curves). For the symmetric TW, the means equilibrate over the time period shown, whereas the means for the $PATW$ do not (though they do equilibrate to within graphical accuracy after an additional 50 units of time). After a complex initial stage, red establishes superiority (point R in the figure). For early times with smooth initial conditions, the competition kinetics are dominant over diffusion (i.e., diffusion operates on a slower

timescale). As a result, the qualitative behavior of the initial stages of the solution can be modeled by the solution to the associated ODE system with the initial conditions given by the means of the PDE initial conditions. The ODE solution is shown over the same interval for the asymmetric mean (solid curves) and the symmetric mean (dotted curves) in Figure 8.4d. For the symmetric initial conditions, the ODE solution does not approach the heteroclinic cycle (even though it is attracting); rather, it approaches the coexistence state. On the other hand, for the asymmetric initial conditions, there is first a complex oscillatory pattern as the solution approaches the heteroclinic cycle. The first species that is completely dominant is v, and it rises to near its carrying capacity around $t = 50$. For smooth mixed initial conditions, the widest patch in the $PATW$ PDE solution appears to be determined by the initially dominant species in the ODE solution. In the PDE solution, after the initial transient, diffusion becomes operable and the solution becomes increasingly spatially homogeneous, creating a rigidly propagating patch structure (as opposed to the heteroclinic cycle for the ODE). From Figure 8.4d, it is clear that although the ODE system is not chaotic, it is very sensitive to the initial conditions.

8.3.3. Steady-State Breather Solutions

Consider patch initial conditions with $R \approx 2.002$, so that the initial ratio of the width of the widest patch to that of the thinnest patch is significantly greater than for the initial conditions that led to the $PATW$ solution in the previous section. There is no longer rigid propagation of asymmetric patches. Instead, after an initial transient, each patch expands (inhales) and contracts (exhales) as the array propagates. Note that the same solution (with a shift in time) is obtained from mixed initial conditions. These solutions

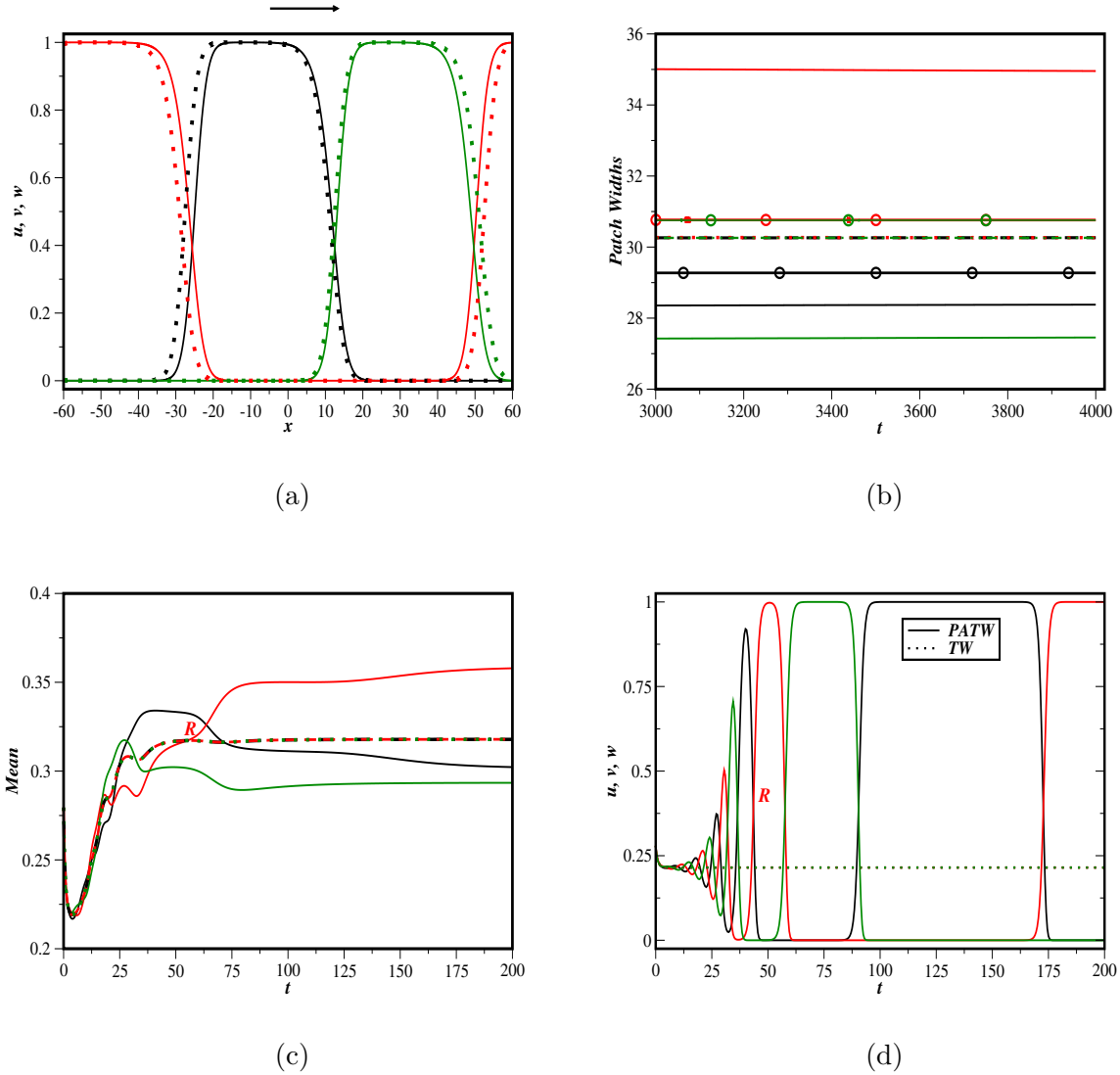

Figure 8.4. (a) Snapshot of $PATW$ (solid curves) and TW (dotted curves) at $t = 4000$. Parameters given in the text. (b) Patch widths as a function of time for $PATW$ solution with mixed initial conditions (solid curves), $PATW$ solution with patch initial conditions and $R \approx 1.038$ (solid curves with circles), and TW solution with mixed initial conditions (dashed and dotted curves). (c) Means at early times of $PATW$ (solid) and TW (dashed and dotted) solutions in Figure 8.4a. (d) ODE solution at early times with initial conditions determined by the mean values of the $PATW$ (solid) and TW (dotted) solutions in Figure 8.4a.

are termed "breathers" and, for steady-state breathers, the breathing is periodic. There are two timescales associated with these solutions: the time required to propagate across the domain and the period of the breathing.

In order to illustrate the nature of the solution, Figure 8.5a shows the patch widths over approximately two breathing periods. The figure also includes the speeds (scaled by a factor of 5 for clarity) of the leading edge (dotted curve) and the trailing edge (dashed curve) of the patch of u. The speeds are computed by searching for the point where $u = 0.9$ and is decreasing (for the leading edge) and where $u = 0.9$ and is increasing (for the trailing edge). These points are obtained by linear interpolation after being bracketed by the grid point data (and adjusted for periodicity). Numerically approximating the spatial derivative at these points gives the two interface speeds. Note that there will always be only one point characterizing the leading edge and one point characterizing the trailing edge, since the integrity of the patch is maintained through the breathing.

Figures 8.5b and 8.5c show the spatial profiles of the densities u, v, and w at points C and E from Figure 8.5a, respectively. Both figures include additional copies of the profiles scaled by 1×10^6 in order to show diffusive penetration of the species into neighboring patches. At point C, the black patch is at its maximum extent. The controlling species red can diffuse into the black patch uncontrolled by green, since the black patch is wide enough and A is small enough to prevent interaction of red and green within the black patch. As a result, the red patch can expand at the expense of the black patch, leading to the contraction of the black patch. Similarly, at point E, the green patch is at its maximum extent and the black patch will now expand at the expense of the green patch due to diffusive leakage. As A decreases (interspecies competition becomes stronger),

the breathing slows down, since diffusive penetration becomes more difficult (it is harder for two species to cohabit the same spatial region). Steady-state breather solutions can be computed for $0.195 \leq A \leq 0.215$. It is prohibitively expensive to compute breather solutions for smaller values of A, due to the extraordinarily long breathing periods. As A increases, diffusive penetration is easier, so the breathing periods are shorter. Additionally, smaller minimal patch widths are possible, since interspecies competition is weaker. As a result, breather solutions cannot be maintained. Instead, there is patch splitting and, ultimately, a transition to chaos.

8.3.4. Transitory Breathers, Patch Splitting, and Chaos

Consider now the case $A = 0.225$ with patch initial conditions such that $R = 1.167$. A plot of the patch widths against time is given in Figure 8.6a. The patches still expand and contract in the RPS order; however, the maxima of the patch widths are monotonically increasing, while the minima are monotonically decreasing. Additionally, the period of the breathing shortens over time (i.e., the breathing becomes more rapid). For this value of A, the breathing does not stabilize. Thus, this behavior is referred to as a transitory breather, and it will be shown immediately below that it is a prelude to chaos. Note that the same behavior occurs for mixed initial conditions.

After $t \approx 4000$, the breathing pattern collapses. Recall that the definition of patch used here is a region for which the density of the dominant species exceeds 0.9. In the collapse seen in the figure, clusters (in which the dominant species does not have time to grow to the density required for a patch) are rapidly generated, and the solution thus becomes chaotic.

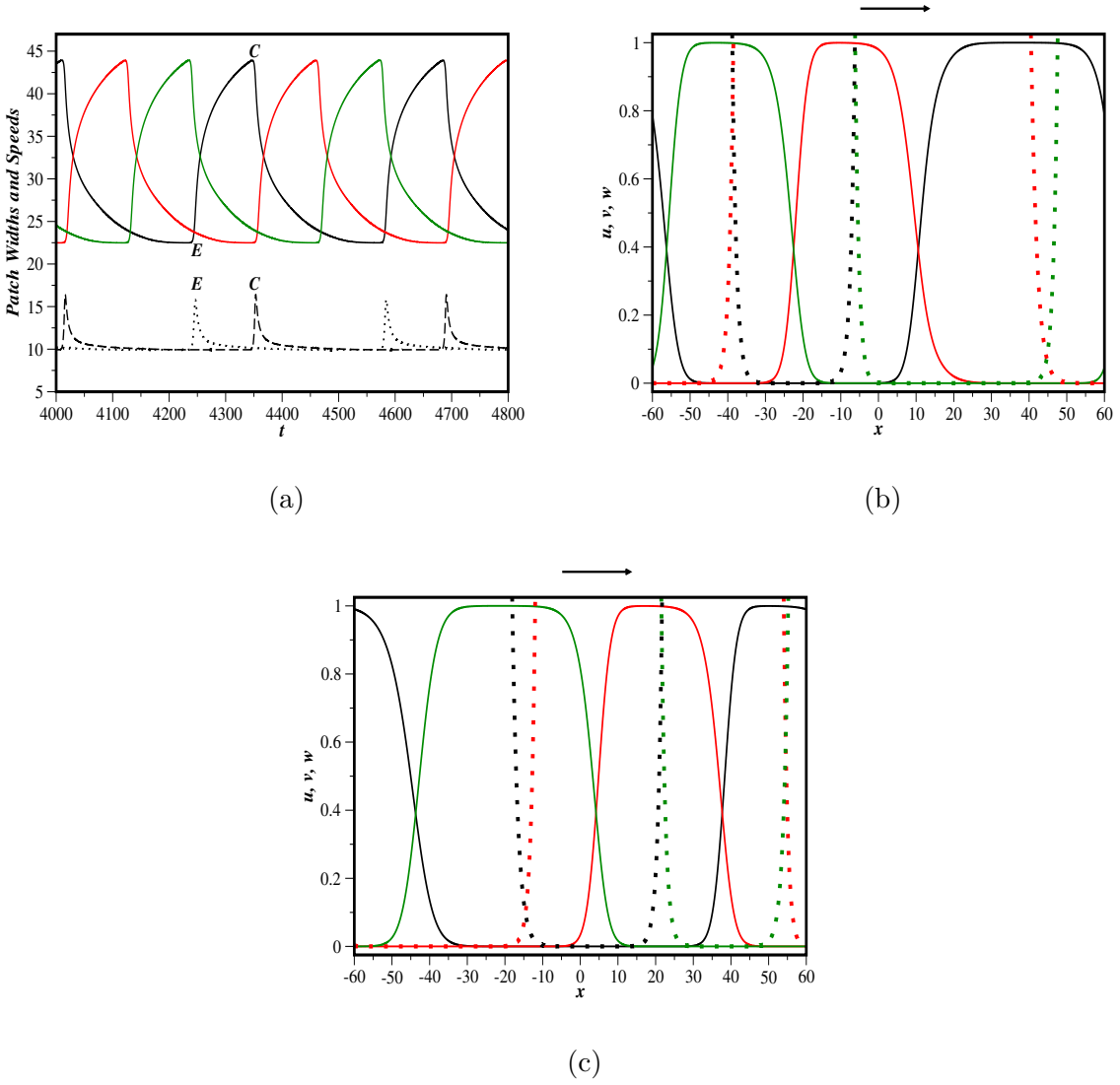

(a)

(b)

(c)

Figure 8.5. (a) Patch widths and interface speeds for steady-state breather solution. Parameters given in the text. The speeds of the leading edge (dotted curve) and the trailing edge (dashed curve) of the patch of u are scaled by a factor of 5. (b) Spatial profiles at point C in Figure 8.5a. The dotted curves are the same profiles scaled by 1×10^6. (c) Spatial profiles at point E in Figure 8.5a. The dotted curves are the same profiles scaled by 1×10^6.

Figure 8.6b shows the patch widths over a restricted time interval, during which the black patch collapses and the red patch expands. The qualitative behavior is similar to that of the steady-state breather in that the speed of the leading edge is greatest when the red patch first starts to expand and then decreases throughout the expansion (note that it is well above 2).

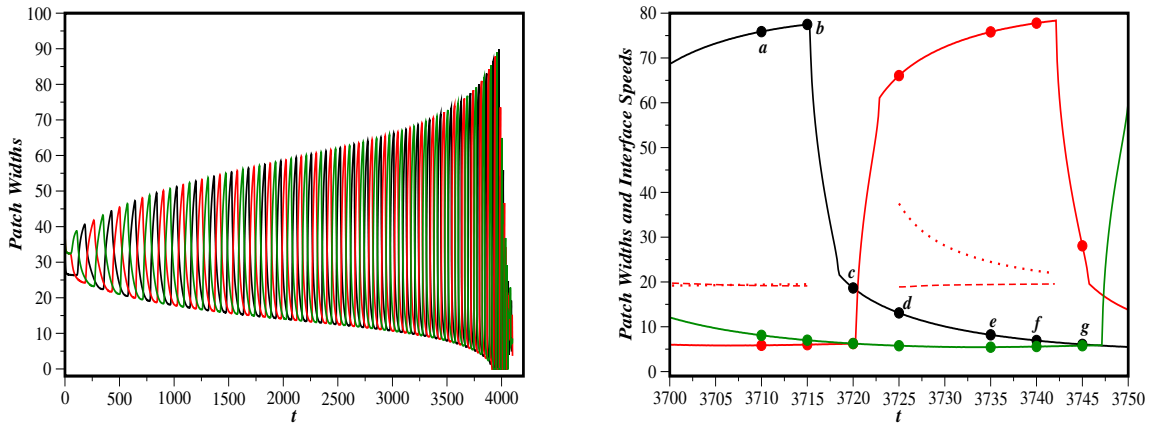

(a) (b)

Figure 8.6. (a) Patch widths for transitory breather with $A = 0.225$. Other parameters given in the text. (b) Patch widths and speeds for the leading edge of the v-patch (dotted curves) and the trailing edge of the v-patch (dashed curves). Speeds are scaled by a factor of 10.

In Figures 8.7-8.9, the spatial profiles at the points labeled a - g in Figure 8.6b are shown. At point a, (Figure 8.7a), red has substantially diffused into the black patch and is just beginning to split it. In order to clearly show the diffusive leakage into the patches, the figure includes copies of the spatial profiles scaled by a factor of 1×10^2 (dotted curves) and an additional copy of red scaled by 1×10^3 (dashed curve). Red, as usual, diffuses forward into the black patch (i.e., through the trailing edge of the black patch),

but, since the green patch is thin, red also back-diffuses into the black patch through the leading edge of the black patch. Within the black patch, green is confined to a small area near the leading edge, so red is not controlled by green in the interior of the wide black patch. A disturbance in red (labeled RB in the figure) of the order 1×10^{-3} signifies the beginning of the splitting of the black patch. At point b (Figure 8.7b), the disturbance RB is visible without scaling, leading to a dip in black - the initial stage in the splitting of the black patch into two smaller patches (denoted D and S in the figure). Patch D is doomed, as it will be surrounded by red, while patch S will survive. At point c (Figure 8.7c), there are two clearly visible red patches (RB and the original red patch, RO). The doomed black patch D has shrunk, while black patch S has survived.

At point d (Figure 8.8a), the two red patches have consumed the black patch D and have merged into one large red patch, creating a three-patch array with the red patch the largest. At this time, the red patch is expanding at the expense of the surviving black patch. At point e (Figure 8.8b), green has back-diffused through the thin black patch and is ready to split red (GB; see the dashed profile in the figure, which shows the density of green scaled by 1×10^3).

At point f (Figure 8.9a), two clearly-defined green patches are visible - the patch that formed as a result of the split (GB) and the original patch GO. The red patch has been split into a doomed patch (D) and a surviving patch (S). At point g (Figure 8.9b), green is the dominant species and the two green patches GB and GO are about to merge. The doomed red patch D is barely visible.

Thus, over the time interval considered, dominance has been transferred from black to red to green via patch splitting. There is no such splitting for steady-state breather

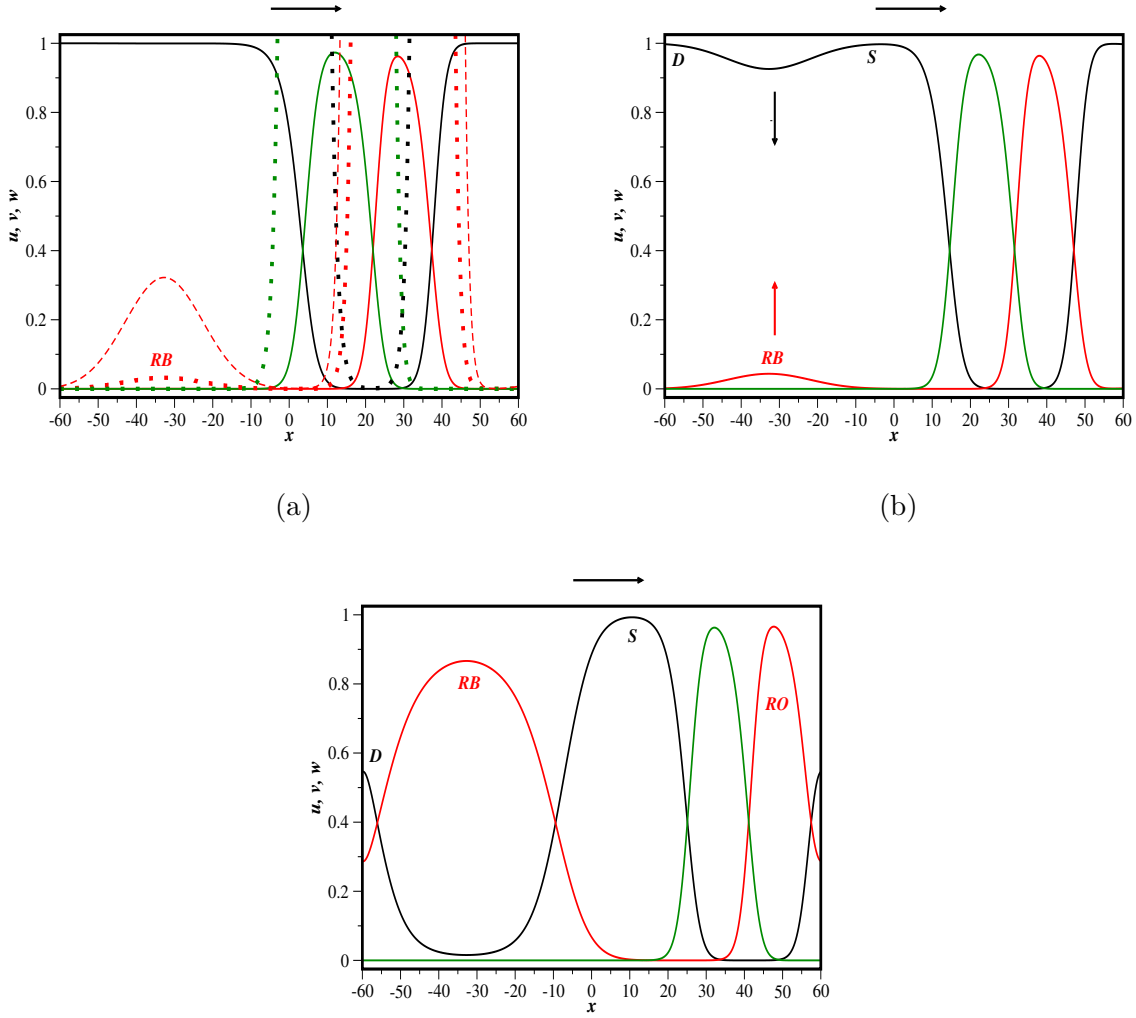

(a)

(b)

(c)

Figure 8.7. (a) Spatial profiles at point a in Figure 8.6b. The dotted curves are the same profiles scaled by 1×10^2 . The dashed curve is just red scaled by 1×10^3 . (b) Spatial profiles at point b. The disturbance RB will split the black patch into two patches: D (doomed) and S (surviving). (c) Spatial profiles at point c. There are now two clearly defined red patches, RB and RO (original red patch). Black patch D is shrinking, as it is doomed, while black patch S survives.

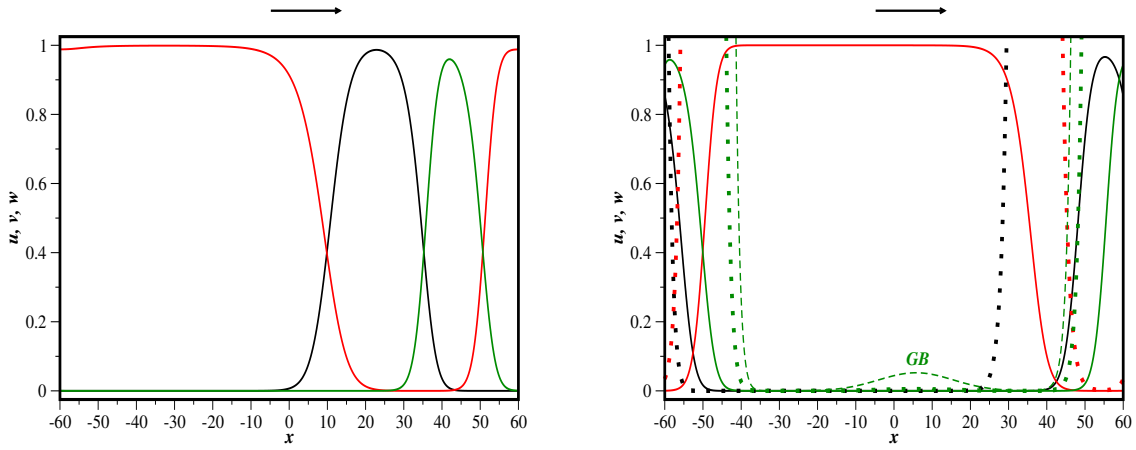

(a) (b)

Figure 8.8. (a) Spatial profiles at point d in Figure 8.6b. The three patch breather array has been restored with red as the largest patch. (b) Spatial profiles at point e. The dotted curves are the same profiles scaled by 1×10^2. The dashed curve is just green scaled by 1×10^3.

solutions - there is only expansion and contraction, at least on a macroscopic level. The splitting is the result of weaker interspecies competition (larger A), allowing multiple species to cohabit the same space to an appreciable extent. Because of this, large patches have to be sufficiently large so as to allow for separation of the three species. This leads to a corresponding decrease in the thin patches, as seen in Figure 8.6a. The splitting occurs increasingly more rapidly, due to the thinness of the small patches. As shown in the figure, the splitting does not stabilize. This is a spatial analogy to the temporal heteroclinic cycle in that each species is dominant over larger and larger spatial regions. However, unlike the temporal heteroclinic cycle, the spatial interval is bounded. The spatial regions of dominance cannot increase indefinitely, causing the solution to collapse into chaos.

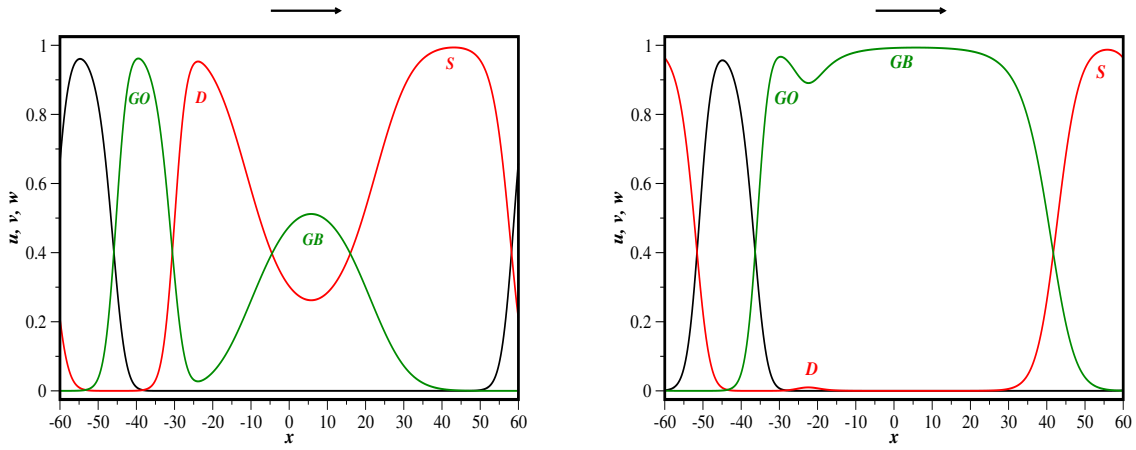

(a) (b)

Figure 8.9. (a) Spatial profiles at point f in Figure 8.6b. The rising green patch RB is now visible without any scaling. It is splitting the red patch into a doomed patch (D) and a surviving patch (S). The original green patch (GO) is also marked in the figure. (b) Spatial profiles at point g. The green patches GB and GO are about to merge. The doomed red patch D is barely visible, so that red has essentially been split by green.

Finally, spatial profiles of the solution in the late stages of this process (times $t_1 = 4012.5$, $t_2 = 4018.75$, and $t_3 = 4025$) are shown in Figure 8.10. At time t_1, the green patch has just been split by black into a doomed patch D and a surviving green patch S. In the normal course of events, the two black patches $B1$ and $B2$ would merge. However, since the green patch S is so thin, red is about to split black before the merger (RR). Since the original red patch RO is still present, there are now five clear patches with an incipient sixth patch (RR). At time t_2, the the black patch $B2$ has been split into $B21$ and $B22$ by the growing red patch RR. Thus, there are now three black patches, since patch $B1$ is still present. There are also two red patches, RR and the original red patch RO. Moreover, there are two green patches, D (not yet eliminated) and S. Finally, at time t_3, the doomed

green patch D has been eliminated. Furthermore, $B21$ has merged with $B1$; however, the resulting patch (labeled $B21$ in Figure 8.10c) is shrinking, since it is now surrounded by two red patches due to the demise of D. Red's dominance is short-lived, however, since RR is in the process of being split by green (GR). The successive splittings become increasingly complicated, leading to the onset of chaos; i.e., chaotic behavior arises due to successively more rapid splittings before the elimination and consolidation of patches, as described above, can occur.

For this value of A, the chaotic behavior itself is transient. When run for a longer time, the solution becomes spatially homogeneous. There are two competing processes: (i) the generation of new clusters and (ii) coarsening due to destruction of doomed clusters that are surrounded by competitors. In this case, the elimination of doomed clusters prevails, and the solution becomes a spatially-homogeneous heteroclinic cycle. An illustration of the coarsening is shown in Figure 8.11, where the solution is shown at times $t = 5593.5$ (solid curves), $t = 5595$ (dotted curves), and $t = 5596.5$ (dashed curves). Coarsening processes are indicated by arrows in the figure. The short time interval shown allows for the elimination of a doomed red cluster (labeled D) while red is exhibiting dominance in other parts of the spatial domain. The coarsening process is complex and relatively prolonged; however, this solution becomes effectively spatially homogeneous around $t = 6000$. As mentioned above, it may be that all chaotic solutions eventually succumb to coarsening, but it is not practical to resolve this issue computationally.

Note that for this value of A, symmetric patch initial conditions and symmetric (in the mean) mixed initial conditions give rise to a simple symmetric patch traveling wave

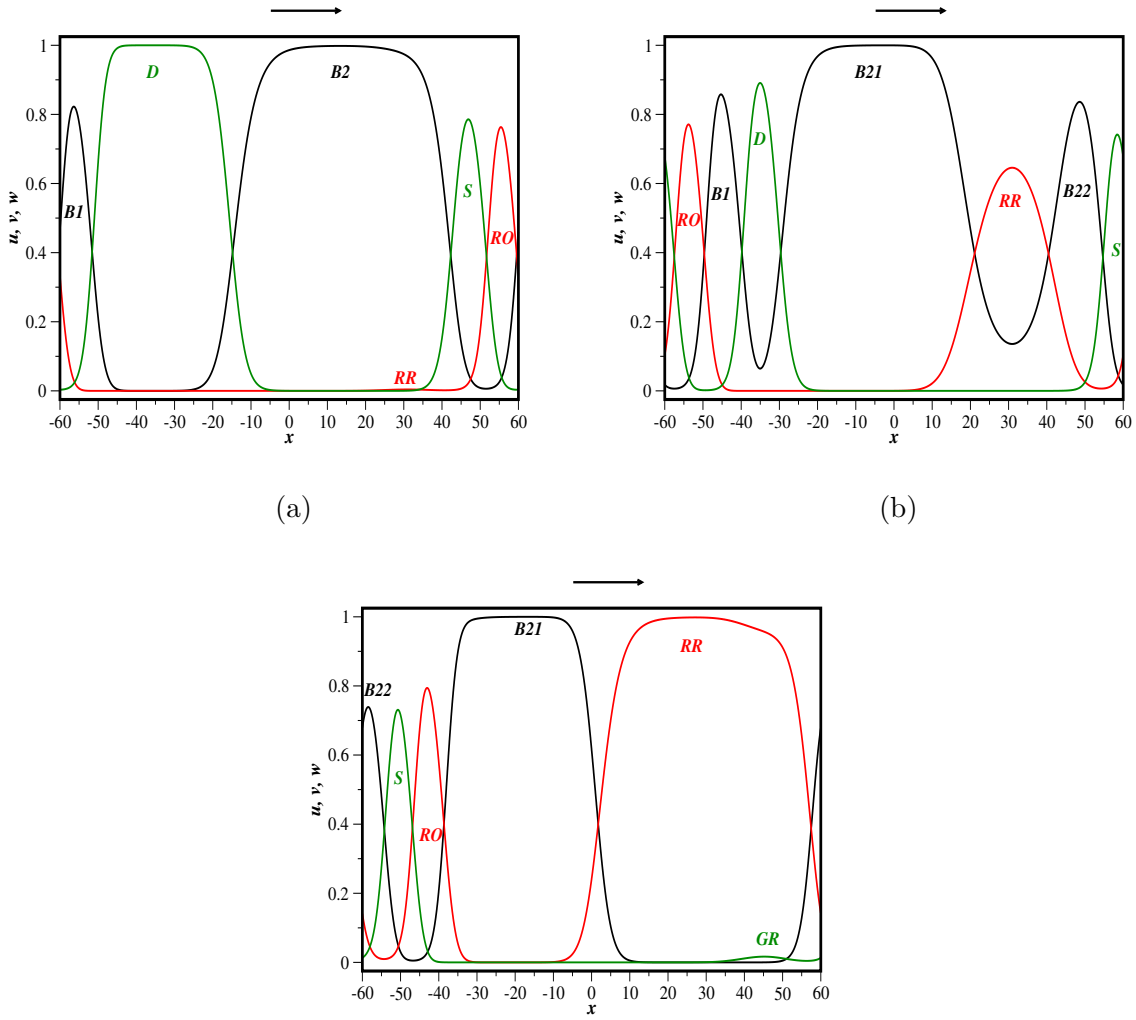

Figure 8.10. Spatial profiles at time (a) $t_1 = 4012.5$, (b) $t_2 = 4018.75$, and (c) $t_3 = 4025$.

that is stable for this value of L. The results described here indicate that much more complicated dynamics can occur when the symmetry in the initial condition is broken.

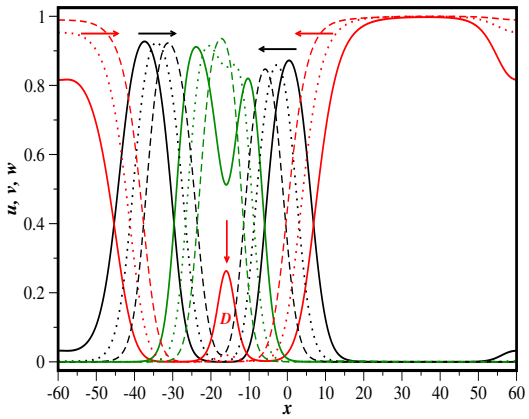

Figure 8.11. Spatial profiles at times $t = 5593.5$ (solid), $t = 5595$ (dotted) and $t = 5596.5$ (dashed), illustrating the coarsening of a chaotic solution leading to spatial homogeneity.

CHAPTER 9

Predictions of 1D Solution Behavior

9.1. Initial Conditions

Here, the results of a set of computations with different initial conditions are tabulated, with a focus on the degree of asymmetry in the initial conditions, the strength of interspecies competition, and the length of the domain. For mixed initial conditions, $\delta = 3$, $m = n = 1$, and $\eta = \varepsilon = 0.3$, as described immediately below (8.2). Furthermore,

$$u_0 = 1 + \kappa, \quad v_0 = 1, \quad w_0 = 1 - \kappa, \tag{9.1}$$

so that the degree of asymmetry is characterized by the parameter κ for mixed initial conditions and by the parameter R for patch initial conditions.

Table 9.1 provides the types of solutions that are obtained as A, L, and the degree of initial asymmetry are varied. The trends are summarized as follows (note that many computations not tabulated here support these trends):

(1) For fixed A and L, increasing the degree of initial asymmetry leads to progressively more complex dynamics (TW to $PATW$ to breather solutions to chaos). It is actually rare to obtain a TW solution. As discussed in Section 8.3.2, for a grid with 2^n points, truly symmetric patch initial conditions are impossible to define - the most symmetric possible conditions for an 8192-point grid, the size used here, have $R = 1.0033$ (starred entry in the table). To compensate for this,

however, rigidly propagating solutions with differences in patch widths of size $O(1 \times 10^{-3})$ were taken to be symmetric patch traveling waves.

(2) For fixed initial asymmetry and fixed L, chaotic behavior is more prevalent as A increases.

(3) For $L = 360$, breather solutions have not been found computationally from mixed initial conditions, but they can be found from patch initial conditions.

(4) For fixed A, chaos is inhibited by increasing L. In all cases examined, chaos ultimately arises due to patch splitting, but patch splitting requires the formation of narrow patches, which is more difficult on large domains.

Finally, the roles of δ, m, and n in (8.2) have been examined. Varying δ and n makes no qualitative change in the types of solutions that can occur. In the case $A = 0.215$, $n = 1$, $L = 60$, $\kappa = 0.05$, and $m = 2$ (doubling the frequency of the mixed conditions), the solution becomes chaotic (for $m = 1$, it is a steady-state breather). This is likely due to the fact that for early times, thinner patches form than for the $m = 1$ case. Note that in order to test stability, a small perturbation of the form $\cos\left(\frac{\pi x}{L}\right)$ was included, since odd modes could not otherwise be introduced to the computation.

9.2. Order Versus Disorder and the Associated ODE System

In this section, it will be shown that patch splitting is a fundamental driver of chaos, even when patches are not well defined (i.e., when they are really clusters). It will further be shown that for mixed initial conditions, this behavior can result from the behavior of the associated ODE system.

A	L	IC	κ	R	Type
0.215	60	M	0	NA	TW
0.225	60	M	0	NA	TW
0.235	60	M	0	NA	C
0.235	360	M	0	NA	$PATW$
0.215	60	M	0.01	NA	$PATW$
0.225	60	M	0.01	NA	C
0.215	60	M	0.05	NA	B
0.215	60	M	0.2	NA	B
0.215	60	M	0.4	NA	B
0.215	360	M	0.4	NA	$PATW$
0.235	360	M	0.4	NA	$PATW$
0.265	360	M	0.4	NA	$PATW$
0.275	360	M	0.4	NA	C
0.215	60	M	0.5	NA	C
0.215	60	M	0.6	NA	C
0.215	360	M	0.6	NA	$PATW$
0.215	60	P	NA	1.0033*	TW
0.215	60	P	NA	1.038	$PATW$
0.215	60	P	NA	1.166	$PATW$
0.225	60	P	NA	1.166	C
0.215	60	P	NA	2.002	B
0.225	360	P	NA	2.002	C
0.215	60	P	NA	4.523	C

Table 9.1. Tabulation of solution types as initial asymmetry (κ or R), A, and L are varied. The initial conditions (IC) can be either mixed (M) or patch (P). Solution types are symmetric traveling waves (TW), pseudo asymmetric traveling waves ($PATW$), steady-state breathers (B), or chaotic (C).

Consider $A = 0.3$, so that interspecies competition is relatively weak. For this value of A with $L = 60$, all solutions that have been computed are chaotic. First, suppose there are symmetric patch initial conditions (technically near-symmetric, as previously discussed). In Figure 9.1a, the patch widths for the resulting solution are shown. The solution is a transitory breather, although instead of each species breathing in turn, the

species breathe simultaneously (compare with Figure 8.6a). This can be attributed to the fact that the species can cohabit the same space with relative ease, due to the weak interspecies competition.

The simultaneous breathing breaks down at $t \approx 175$, leading to irregular behavior in the patch widths. Recall that the patch widths are defined as the spatial extent over which a species density exceeds 0.9. Thus, a near-zero patch width does not necessarily imply that a species is largely absent across the domain - just that it does not generally exceed 0.9. The transition to chaos is still via patch splitting. This is illustrated at $t = 175$, near the start of the chaotic behavior (Figure 9.1b).

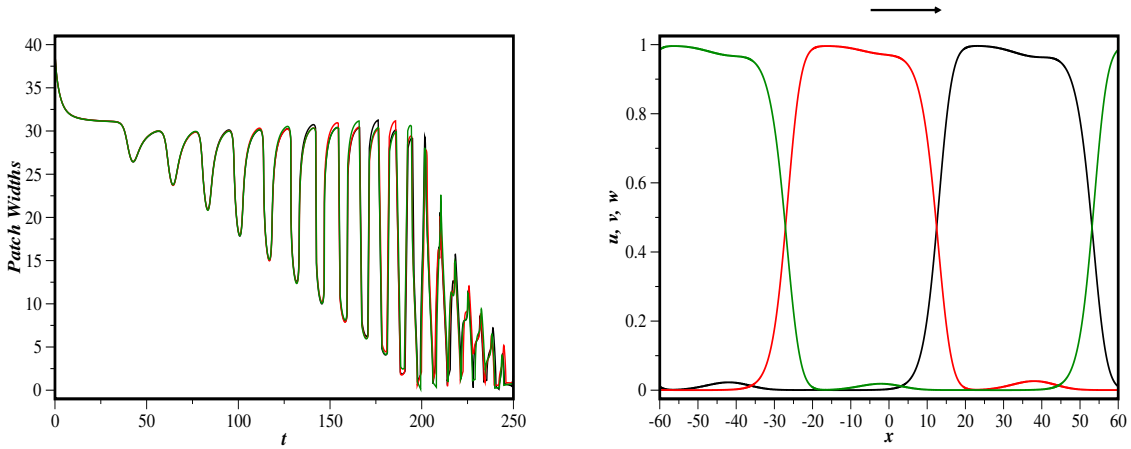

(a) (b)

Figure 9.1. (a) Patch widths for transitory simultaneous breather and transition to chaos. $A = 0.30$ with patch initial conditions and $R = 1.0033$. (b) Spatial profiles at $t = 175$ for transitory simultaneous breather, showing incipient patch splitting, the mechanism leading to chaos.

Next, consider mixed initial conditions with asymmetric means, $(u_0, v_0, w_0) = (1.4, 1, 0.6)$ (the initial conditions used to generate Figure 8.3). For $A =$

0.215, a breather solution is found (see Table 9.1). For $A = 0.3$, the solution becomes chaotic around $t = 50$. Chaos occurs before true patches can form; there are just clusters in which one species dominates, but all species are present. However, the onset of chaos still occurs via cluster splitting as a consequence of diffusive leakage. This is illustrated in Figure 9.2a, where the solution is plotted at $t = 47.5$ (solid curves) and $t = 50$ (dashed curves). This is early in the transition to chaos, but the figure shows red splitting a large black cluster into two regions: a region marked D, which is surrounded by red (and thus doomed) and a region marked S, which can survive. The origin of chaotic behavior can be traced to cluster or patch splitting in many other computations as well.

For comparison, Figure 9.2b shows the solution at $t = 55$ with the same initial conditions, but with $A = 0.215$. By this time, true patches have formed and the system is in the early stages of breather formation (not yet equilibrated). Patches can form because it is difficult for all three species to occupy the same spatial region due to the stronger interspecies competition. The patches are more easily maintained not only because of the large coefficient σ, but also because the dominant species is at or near its carrying capacity (unity), thus making it more effective in killing off its victim species (note the form of the interspecies competition terms in System (8.1)).

Now, consider the relationship between the chaotic solution and the associated ODE computation. For the ODE computation, the initial conditions are taken as the means of (8.2); i.e.,

$$u(0) = (1 + \eta u_0)A, \quad v(0) = (1 + \eta v_0)A, \quad w(0) = (1 + \eta w_0)A. \tag{9.2}$$

In Figure 9.3a, the time-dependent spatial means of u, v, and w from the PDE computation are plotted (solid curves) along with the ODE solution with (9.2) as the initial conditions (dashed curves) for early times. The dark circles in the figure correspond to the times of the spatial profiles in Figure 9.2a and are the times when there is a transition to chaos via cluster splitting.

Both the PDE means and the ODE solution are oscillatory and exhibit similar qualitative behavior up to the time of the transition to chaos (dark circles in the figure). For very early times (e.g., $t \approx 10$), the two solutions are very close. For $t > 10$, the solutions drift apart. The drift can be attributed to the impact of diffusion on the oscillations; i.e., diffusion causes the time between successive oscillations to increase because it couples neighboring spatial regions. Since the ODE solution will approach the attracting heteroclinic cycle, the oscillations in the ODE solution do not stabilize; rather, they increase monotonically (note that for this initial condition, the oscillations approach unity and exhibit the characteristic behavior of a heteroclinic cycle at $t \approx 125$). On the other hand, the slow increase of the oscillations in the means of the PDE solution inhibits the formation of patches because the dominant species in the clusters that form are slow to approach carrying capacity. The relatively small dominant species densities, along with the relatively small interspecies competition coefficient σ, create a situation in which each species is not very effective in controlling its victim species. This allows the species to share the same spatial regions, leading to the cluster splitting shown in Figure 9.2a and ultimately to chaos.

Conversely, consider the PDE and ODE solutions with the initial conditions described above, but with $A = 0.215$ (Figure 9.3b). As before, both solutions are similar up until

$t \approx 10$, at which point they drift apart as the periods of the oscillations in the means of the PDE solution increase relative to those of the ODE oscillations (again, diffusion slows down the oscillatory motion). However, for these initial conditions, the approach of the ODE solution to the heteroclinic cycle is much more rapid (at $t \approx 60$, the ODE solution already has the characteristics of a heteroclinic cycle). The PDE solution means also grow much more rapidly than in the $A = 0.3$ case and are able to stabilize in amplitude (recall that since the PDE solution is a breather, all of the spatial means are necessarily below unity and greater than zero). The fact that the PDE oscillations stabilize at a relatively high level, combined with the interspecies competition coefficient σ, enables the formation of patches, since each species is efficient in expelling its victim species from its patch. Said another way, the species self-segregate, there is no patch splitting and thus no transition to chaos; instead, the solution is an ordered steady-state breather. For both values of A, the behavior of the PDE solution is associated with the behavior of the associated ODE system. This relationship has been observed for many other parameters as well.

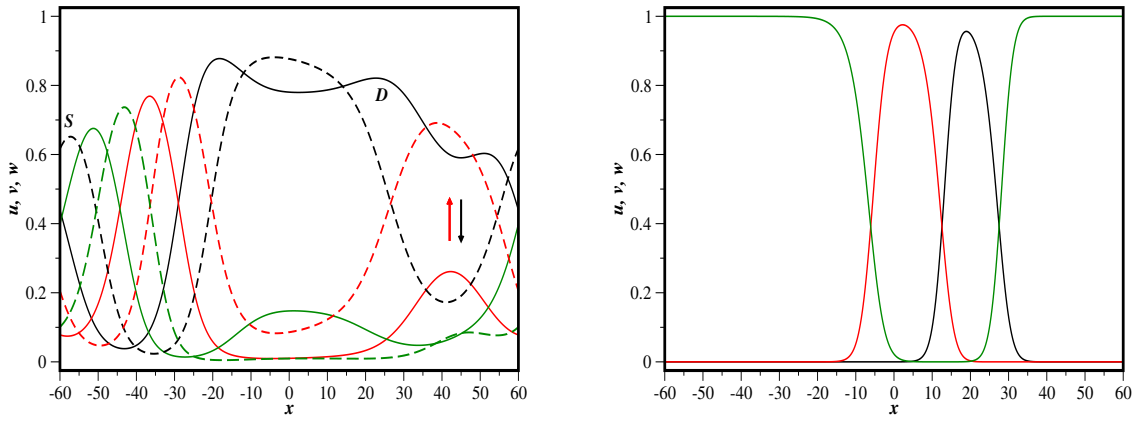

(a) (b)

Figure 9.2. (a) Cluster splitting for transition to chaos using mixed initial conditions. The solution is plotted at times $t = 47.5$ (solid curves) and $t = 50$ (dashed curves). $A = 0.30$ and other parameters given in the text. The splitting motion is shown via arrows and the resulting split clusters are denoted by D and S. (b) Spatial profiles for breather solution, $A = 0.215$ at $t = 55$. Other parameters the same as for Figure 9.2a.

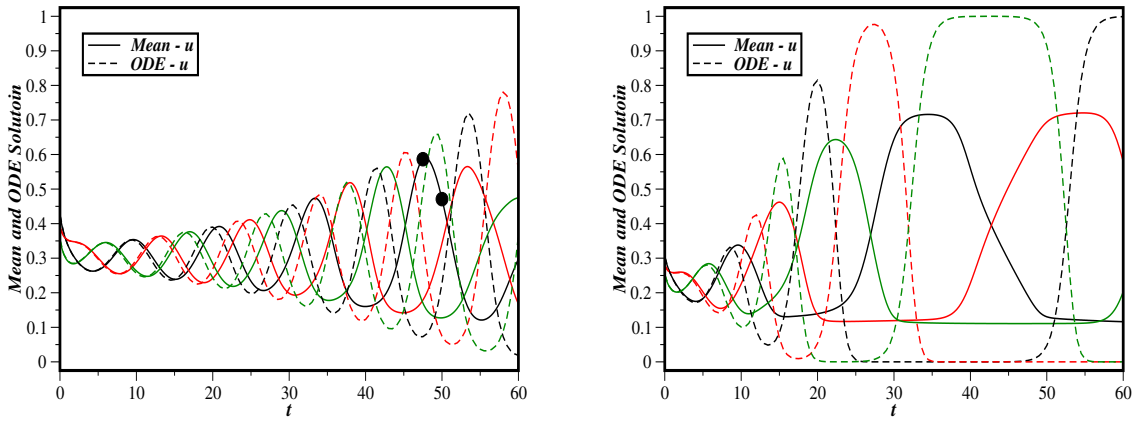

(a) (b)

Figure 9.3. (a) ODE solution with (9.2) as initial condition (dashed curves) and the means of the PDE solution for early times (solid curves). The circles indicate the times for the spatial profiles shown in Figure 9.2a. $A = 0.30$ (chaotic PDE solution). Other parameters given in the text. (b) ODE solution using (9.2) as initial condition (dashed curves) and the mean of the PDE solution for early times (solid curves). $A = 0.215$ (breather PDE solution). Other parameters the same as for Figure 9.3a.

CHAPTER 10

Solution Behavior for 2D Symmetric RPS Systems

10.1. System Setup

The two-dimensional symmetric version of System (3.6) on the domain $[-L, L] \times [-L, L]$ is

$$\frac{\partial u}{\partial t} = \frac{\partial^2 u}{\partial x^2} + \frac{\partial^2 u}{\partial y^2} + u(1 - u - \sigma v), \tag{10.1a}$$

$$\frac{\partial v}{\partial t} = \frac{\partial^2 v}{\partial x^2} + \frac{\partial^2 v}{\partial y^2} + v(1 - v - \sigma w), \tag{10.1b}$$

$$\frac{\partial w}{\partial t} = \frac{\partial^2 w}{\partial x^2} + \frac{\partial^2 w}{\partial y^2} + w(1 - w - \sigma u), \tag{10.1c}$$

so that, as in the symmetric 1D system, $d_v = d_w = 1$, $u_* = v_* = w_* = A$, and $\alpha = \beta = \gamma = \sigma = \frac{1-A}{A}$. The coexistence state is again unstable if $A < A_* = 1/3$ (equivalently, $\sigma > \sigma_* = 2$).

In two dimensions, four general types of solutions have been found in the unstable coexistence regime, three of which are ordered. As in 1D, the ordered solutions are primarily composed of single-species regions. The four categories are as follows:

(1) Chaotic solutions - exhibiting spatiotemporal chaos

(2) Spiral solutions - composed of spirals with each arm comprised of mainly one species

(3) Single-species dominance - spatially-homogeneous solution that approaches the heteroclinic cycle

(4) Traveling fluid patches - propagation of non-rigid patches

Throughout this chapter, mixed initial conditions are defined as

$$u(x,y,0) = \left(1+\varepsilon\cos\left(\frac{\pi x}{L}\right)\cos\left(\frac{\pi y}{L}\right)\right)A, \tag{10.2a}$$

$$v(x,y,0) = \left(1+\varepsilon\cos\left(\frac{\pi x}{L}+\frac{2\pi}{3}\right)\cos\left(\frac{\pi y}{L}\right)\right)A, \tag{10.2b}$$

$$w(x,y,0) = \left(1+\varepsilon\cos\left(\frac{\pi x}{L}+\frac{2\pi}{3}\right)\cos\left(\frac{\pi y}{L}+\frac{2\pi}{3}\right)\right)A, \tag{10.2c}$$

where $\varepsilon = 0.3$ as before and L is taken to be 60 unless otherwise specified. Other computations have been run with many different initial conditions, but qualitatively different behaviors have not been found.

10.2. Illustrations of 2D Solution Behavior

Here, the four types of 2D solutions are illustrated.

10.2.1. Chaos

Consider System (10.1) with the mixed initial conditions (10.2). The solution is shown at time $t = 2400$ in Figure 10.1. Refer to Table 10.1 for the key to this plot and all similar plots in this chapter. As in the analogous 1D computation, the solution appears disordered and shows no recognizable pattern. Additionally, there is no clear separation of the species, due to weak interspecies competition (small σ).

Color	State
Black	Strong u Dominance
Dark Gray	Moderate u Dominance
Light Gray	Weak u Dominance
Dark Red	Strong v Dominance
Light Red	Moderate v Dominance
Orange	Weak v Dominance
Dark Green	Strong w Dominance
Light Green	Moderate w Dominance
Yellow	Weak w Dominance
White	Extinction
Magenta	Coexistence
Cyan	Transition Region

Table 10.1. Color plot key. A species is considered to be strongly, moderately, or weakly dominant if its density is at least 0.6, 0.3, or 0.05 greater, respectively, than the densities of the other two species.

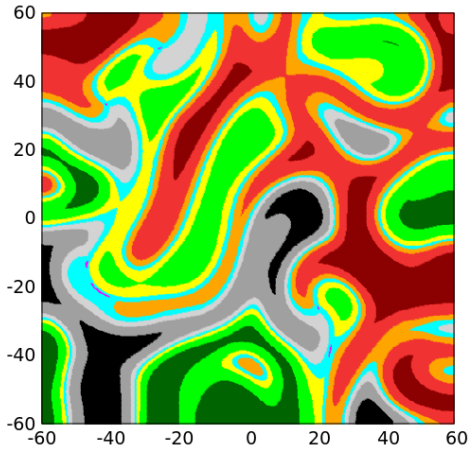

Figure 10.1. Chaotic solution at $t = 2400$ for $A = 0.3$. Color scheme defined in Table 10.1.

10.2.2. Spirals

It has long been known that reaction-diffusion systems, particularly those that model biological and chemical processes, can have spiral solutions [**51**]. Often, these spirals are associated with excitable media [**52**]. While System (10.1) does not model an excitable

medium, spirals are perhaps the most readily computable two-dimensional ordered pattern. As with the ordered patterns found in 1D, spirals are only found when there is sufficiently strong interspecies competition. As with 1D traveling wave solutions, the strength of competition required varies inversely with the size of the domain, in agreement with the results presented in [**37**] and [**46**]. In this case, spirals can be found for many different initial conditions. Below, two examples of spirals are given.

Single spirals can be found for both mixed and patch initial conditions, as long as the patches are such that diffusion can bring all three species together in non-negligible concentrations (see [**53**] for details of spiral formation). Given an array of small, randomly-placed single-species patches, if A is sufficiently small, spiral formation is generally (but not exclusively) expected. The patch initial conditions shown in Figure 10.2a gives rise to a single spiral solution (shown at $t = 2400$ in Figure 10.2b) when $A = 0.16$. The spiral is composed of three essentially single-species arms, and the rotation about the center is such that the different species chase each other in the RPS sequence. At this time, the spiral encompasses the entire computational domain, although the arms are truncated at the boundaries due to the no-flux boundary conditions. The solution persists for as long as it was computed (certainly for a length of time beyond what is experimentally relevant).

Figure 10.2c shows the behavior at the center of the spiral (bracketed as closely as possible). The solution at this point is oscillatory (graphically periodic), with low-level oscillations about some value B close to, but greater than, A. The existence of a small gap between A and B is not entirely surprising; it has been previously shown, for a related

model, that the average species densities are not, in general, exactly A within a spiral core [**54**].

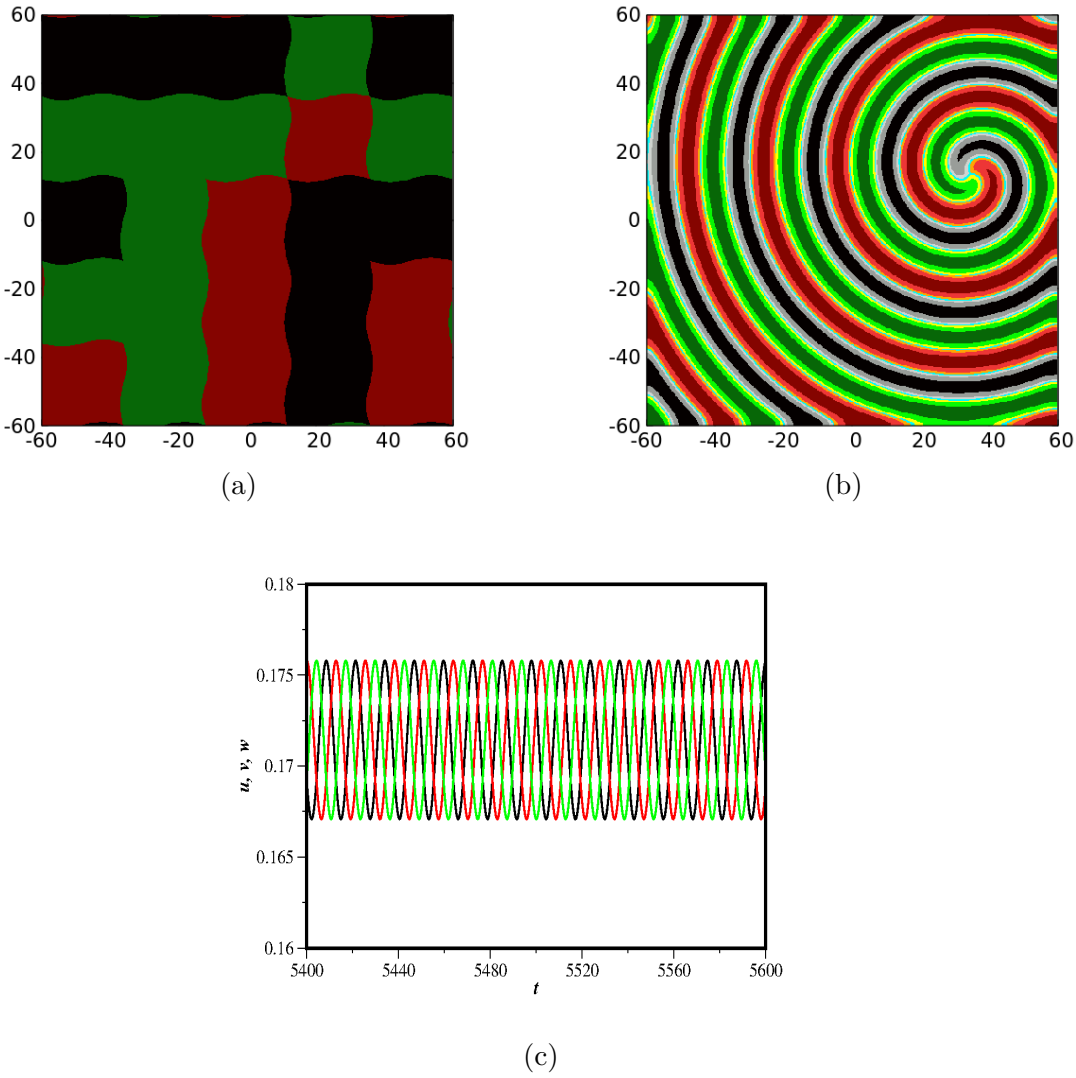

Figure 10.2. (a) Patch initial conditions that give rise to a single spiral. (b) Single spiral solution at $t = 2400$ for $A = 0.16$. (c) u, v, and w near the center of the spiral for $5400 \leq t \leq 5600$.

Spiral pairs [**55**] are also possible for different initial conditions. The solution for $A = 0.16$ from the mixed initial conditions at $t = 2000$ is shown in Figure 10.3. This solution is

not a steady-state solution. For longer times, the spiral pairs separate and eventually, one spiral in each pair is disrupted by the boundary and is destroyed, a behavior reminiscent of the spiral annihilation discussed in [**56**] (and indeed, such solutions were found to occur in the regime of strong interspecies competition). There is then a collection of single spirals which are sufficiently separated so that they do not interact, a configuration that persists for as long as it was computed.

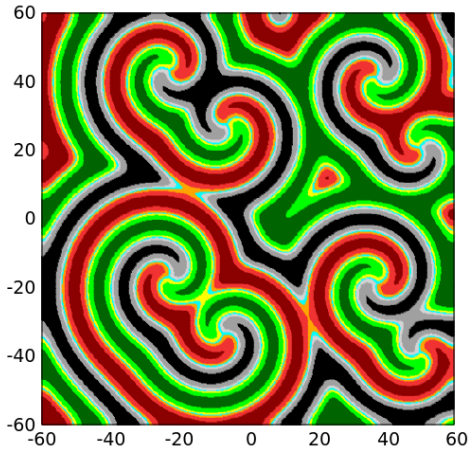

Figure 10.3. Multiple spiral structure from mixed initial conditions at $t = 2000$ for $A = 0.16$.

10.2.3. Single-Species Dominance

Consider the patch initial condition shown in Figure 10.4a. The solution for $A = 0.1$ is shown in Figures 10.4b-10.4d at times $t = 100$, $t = 120$, and $t = 140$. By $t = 120$, due to coarsening, species u is effectively no longer present in the domain. This essentially creates a two-species system consisting of v and w. Since v is susceptible to w, w quickly kills off v, and thus a state very close to the single-species state c_w is attained by $t = 140$ (corresponding to less than two days in physical time). As in other cases of coarsening,

the solution becomes (graphically) spatially homogeneous and approaches the heteroclinic cycle.

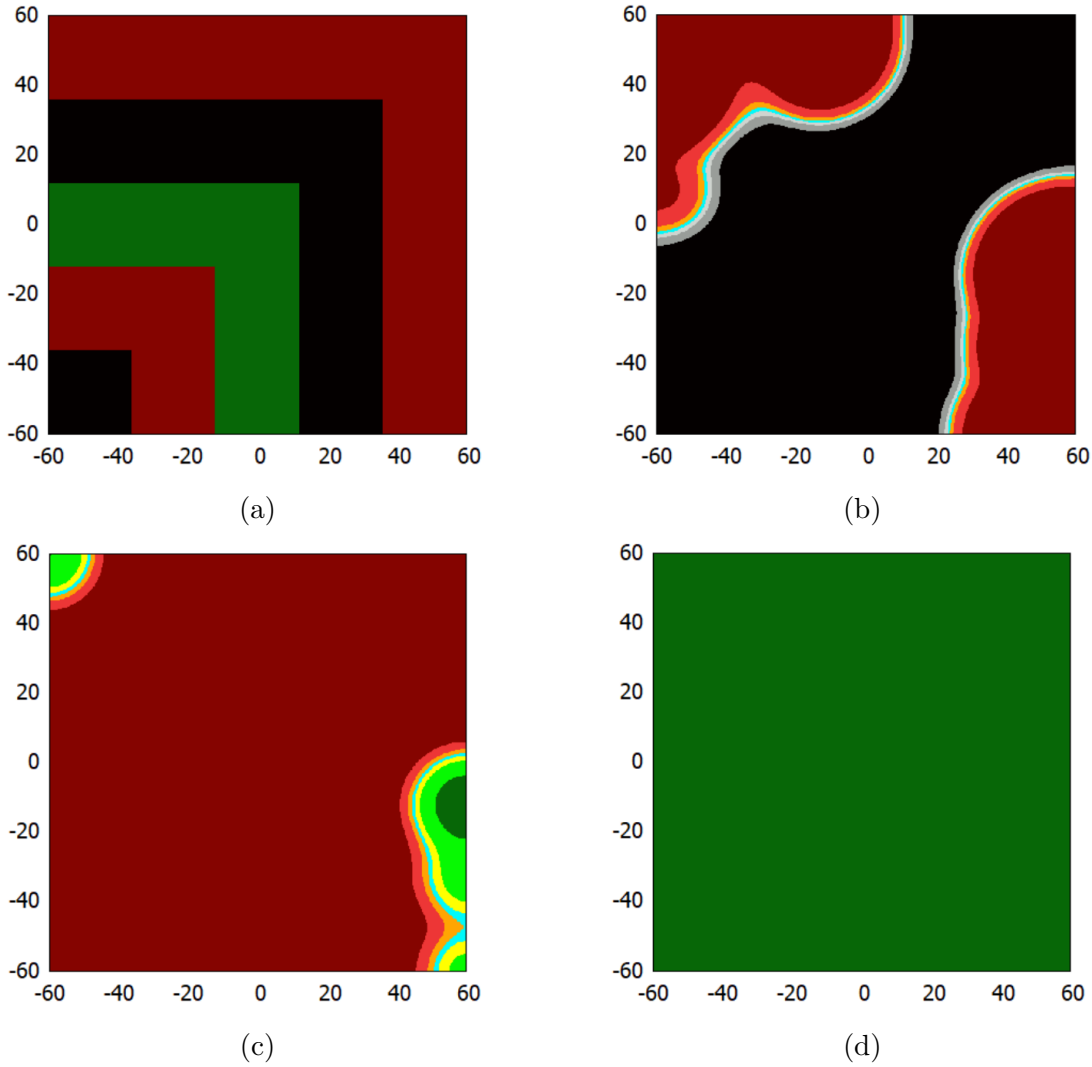

Figure 10.4. (a) Patch initial conditions that give rise to a single-species solution. (b) Solution at $t = 100$ for $A = 0.1$. (c) $t = 120$. (d) $t = 140$, where essentially only w remains.

10.2.4. Traveling Fluid Patches

Slightly modifying the patch initial condition used previously (see Figure 10.5a), again taking $A = 0.1$, and increasing L to 165 leads to a solution in which single-species patches consistently develop in regions dominated by victim species. The solution is shown over a short time interval in Figures 10.5b - 10.5d. In this interval, black patches develop in regions dominated by green. These patches, which expand at the expense of green, will later be disrupted in a similar manner by red. These processes continue for as long as the solution was computed.

As in analogous 1D computations, diffusion allows species to leak into patches of their victim species. If this leakage is allowed to occur virtually unchecked, a dominant species will be able to grow within a patch of its victim species, displacing the victim species from within. Additionally, note the effect of curvature on the speed of the species-species interfaces: as the signed curvature of the interface increases, its speed decreases, which is consistent with analysis of the Fisher-KPP equation (see Sections 4.1.3 and 4.2.1). This causes a "flattening" of the interface over time; i.e., the curvature at each point of the interface tends to zero. Thus, though the shapes of the patches are initially not fixed, on a sufficiently large domain, the patches may eventually be treated as constant in shape.

Other configurations of traveling curved patches are also possible. One such example is a pacemaker, as illustrated in Figure 10.6. The initial conditions consist of a small circular (unstable) coexistence region within an ambient environment of only black. A circular red patch (which can be thought of as a circular ripple) is ejected from the coexistence region, propagating outward as it displaces the ambient species u. This is followed by a circular green patch displacing v, and so forth. Coexistence does not directly displace

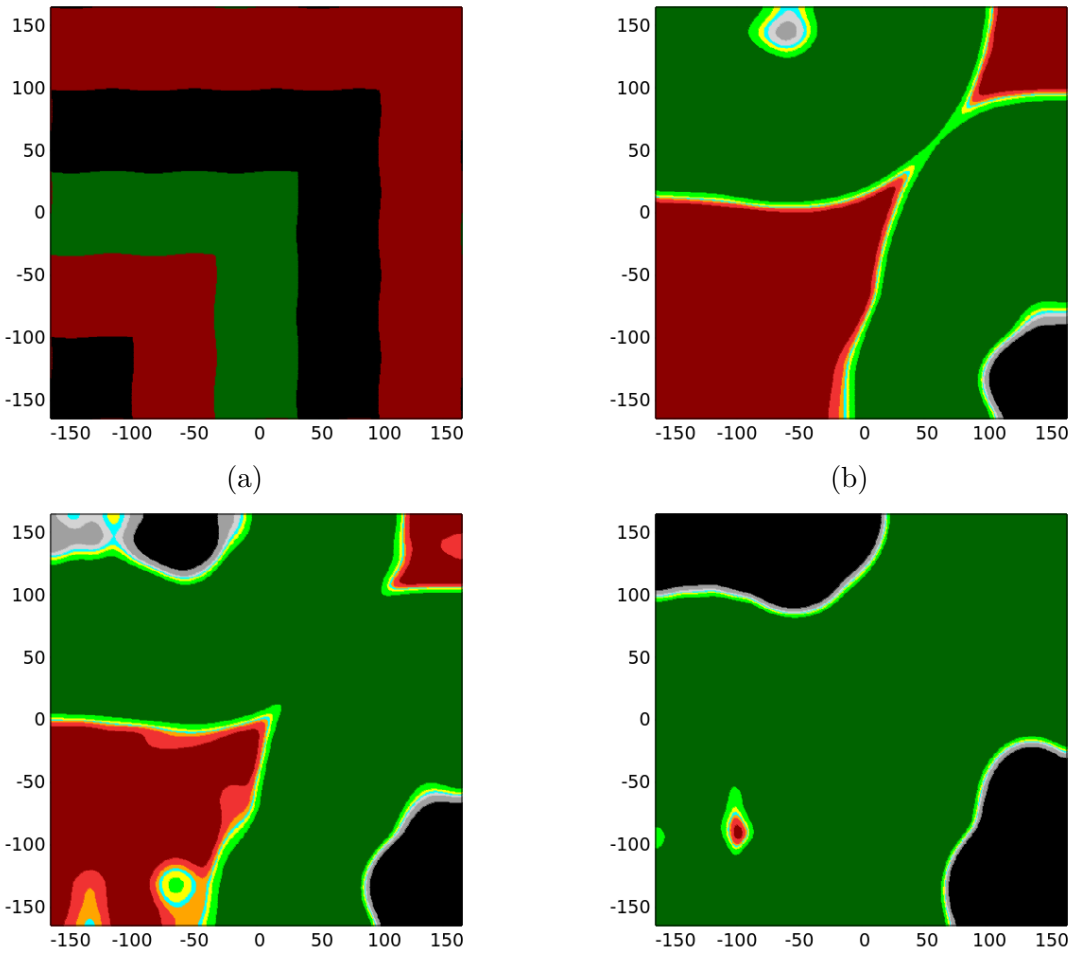

Figure 10.5. (a) Patch initial conditions that give rise to a fluid patch solution. (b) Solution at $t = 2421$ for $A = 0.1$. (c) $t = 2424$. (d) $t = 2431$.

a single species; rather, the displacement occurs via a succession of ripples propagating outward from the coexistence region in the *RPS* sequence. Such behavior also occurs in 1D, as shown in [**16**]. Note that the pacemaker pattern does not persist forever, in this case, as coarsening eventually leads to spatial homogeneity.

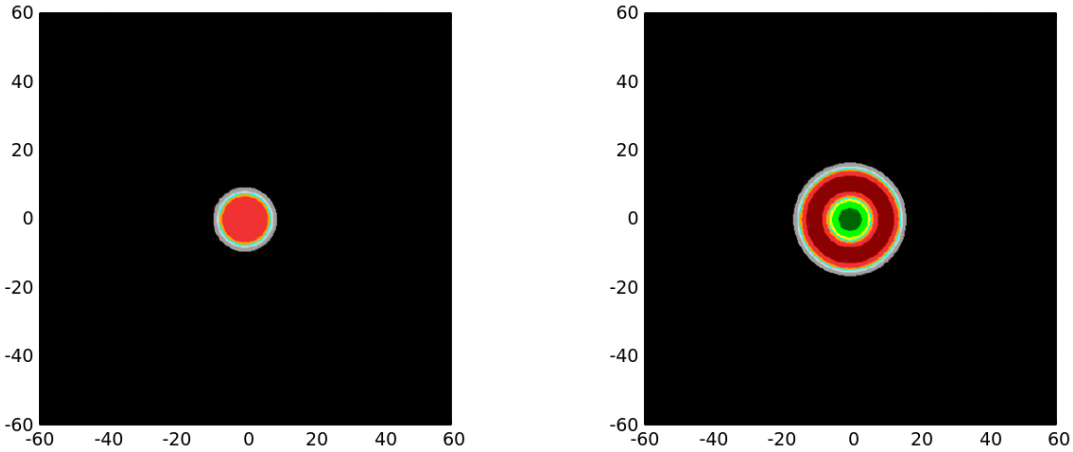

(a) (b)

Figure 10.6. (a) Pacemaker pattern at $t = 4$. (b) $t = 8$.

CHAPTER 11

Survival of the Weakest Phenomenon

Recall that for the symmetric RPS system, the only way to distinguish the three species is via the initial conditions. If the initial conditions for all three species in a 1D symmetric system are identical, then

$$\lim_{t\to\infty} (u(t,x), v(t,x), w(t,x)) = (A, A, A), \tag{11.1}$$

where $A = \frac{1}{\sigma+1}$ with $\sigma = \alpha = \beta = \gamma$ as before; i.e., when there is no mechanism to distinguish any of the species, the solution converges to the coexistence state. In particular, this is true in the regime of unstable coexistence ($A < 1/3$). To see this, consider that if the initial conditions are identical for all three species, then

$$u(t,x) = v(t,x) = w(t,x), \tag{11.2}$$

so that any one species (say, u) satisfies the scalar equation

$$\frac{\partial u}{\partial t} = \frac{\partial^2 u}{\partial x^2} + u(1 - u - \sigma u), \tag{11.3}$$

for which $u = A$ is a stable fixed point (the only stable equilibrium). It has been verified that computations respect the symmetry $u = v = w$ and that the numerical solutions approach (A, A, A) as $t \to \infty$ when the initial conditions are the same for all species.

Although breaking the symmetry of the problem via the initial conditions allows the solution to evolve to either an ordered or chaotic state, the resulting solutions often still inherit some form of symmetry. As described in Section 8.3.1, the temporal averages of the species fractions $\bar{u}(t)$, $\bar{v}(t)$, and $\bar{w}(t)$ (spatial means of the mass fractions of u, v, and w) are very close to 1/3 over a sufficiently long period of time for chaotic solutions to the symmetric problem. For steady-state breather solutions (Section 8.3.3), as shown by the solid curves in Figure 11.1, the average species fraction over a period is clearly the same for each species and it is, in fact, 1/3 to a very close approximation. Finally, for a symmetric patch traveling wave, the solution is three equally-spaced patches and the species fraction is clearly 1/3 for each species (species fractions shown with dots, circles, and crosses in Figure 11.1). Furthermore, note that for the 2D solutions discussed in Chapter 10, average species fractions over a sufficiently long period of time are also 1/3 to within a close approximation. In these cases, no species enjoys sustained overall dominance. Note that there is a dominant species in pseudo asymmetric traveling wave solutions, though the identity of the dominant species is determined by the initial conditions.

Asymmetry can be introduced to the RPS system through unequal diffusivities or unequal interaction coefficients. Clearly, in many *E. coli* systems (e.g., the one described in [**3**]), the interaction coefficients would be unequal, since the mechanisms of competition are different. A few representative results are discussed below (mainly in terms of species fractions, since the primary effect of breaking the symmetry of the problem is the introduction of a hierarchy of dominance), while a more detailed discussion in the context of an exceptional species is given in the following chapters.

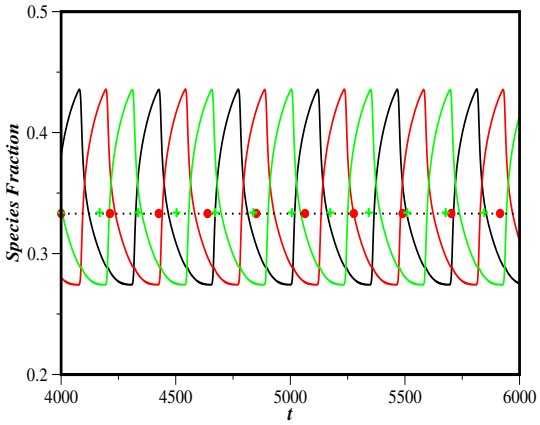

Figure 11.1. Species fractions for breather solution (solid curves) and symmetric patch traveling wave (dotted curve, circles, and crosses) for the symmetric RPS system with $A = 0.215$.

Throughout this chapter, System (3.6) will be considered on the interval $[-L, L]$ (1D) or on the square $[-L, L] \times [-L, L]$ (2D) with the mixed initial conditions

$$u(0,x) = \left(1 + \varepsilon \cos\left(\frac{\pi x}{L}\right)\right) u_*, \tag{11.4a}$$

$$v(0,x) = \left(1 + \varepsilon \cos\left(\frac{\pi x}{L} + \frac{2\pi}{\delta}\right)\right) v_*, \tag{11.4b}$$

$$w(0,x) = \left(1 + \varepsilon \cos\left(\frac{\pi x}{L} + \frac{4\pi}{\delta}\right)\right) w_* \tag{11.4c}$$

in 1D and

$$u(0,x,y) = \left(1 + \varepsilon \cos\left(\frac{\pi x}{L}\right) \cos\left(\frac{\pi y}{L}\right)\right) u_*, \tag{11.5a}$$

$$v(0,x,y) = \left(1 + \varepsilon \cos\left(\frac{\pi x}{L} + \frac{2\pi}{3}\right) \cos\left(\frac{\pi y}{L}\right)\right) v_*, \tag{11.5b}$$

$$w(0,x,y) = \left(1 + \varepsilon \cos\left(\frac{\pi x}{L} + \frac{2\pi}{3}\right) \cos\left(\frac{\pi y}{L} + \frac{2\pi}{3}\right)\right) w_* \tag{11.5c}$$

in 2D, with $\varepsilon = 0.3$ and u_*, v_*, and w_* the components of the coexistence state.

11.1. Unequal Diffusivities

Consider (3.6) with $\alpha = \beta = \gamma = \sigma$ and $d_w = 1$, but with $d_v = 1.1$. The solution to the 1D symmetric problem (i.e., with $d_v = 1$) with the initial conditions (11.4), $u_* = v_* = w_* = A = \frac{1}{\sigma+1} = 0.215$, $\delta = 3$, and $L = 60$ is a symmetric patch traveling wave, due to the symmetry in the initial conditions. With $d_v = 1.1$, however, the solution is a breather. Unlike the breathers found for the symmetric problem, the temporal oscillations in the species fractions are not identical (Figure 11.2a). Overall, it is clear that w is the most dominant species overall, with the more mobile species v second. This perhaps surprising result is explained by overcompensation: the increased effectiveness of v in penetrating patches of u reduces the presence of u, allowing growth of w beyond what would normally be expected. For this system, it is very often the controlling species of the most advantaged species that is dominant. This phenomenon, termed "survival of the weakest" [**57**] has been observed in other models of RPS competition and experimentally in ecosystems of *E. coli* variants [**58**].

In two dimensions, with $L = 60$, $A = 0.16$, and $d_v = d_w = 1$, a spiral solution arises from the initial conditions (11.5). With $d_v = 1.1$, the spirals are not disrupted (at least, not on any ecologically-relevant timescale), but the species fractions (Figure 11.2b) again show a clear hierarchy of dominance ($w > v > u$).

11.2. Unequal Interaction Coefficients

Consider now System (3.6) with $d_v = d_w = 1$, but $\alpha \neq \beta \neq \gamma$, so that the effect of interspecies competition is not uniform among the species. The 1D problem with

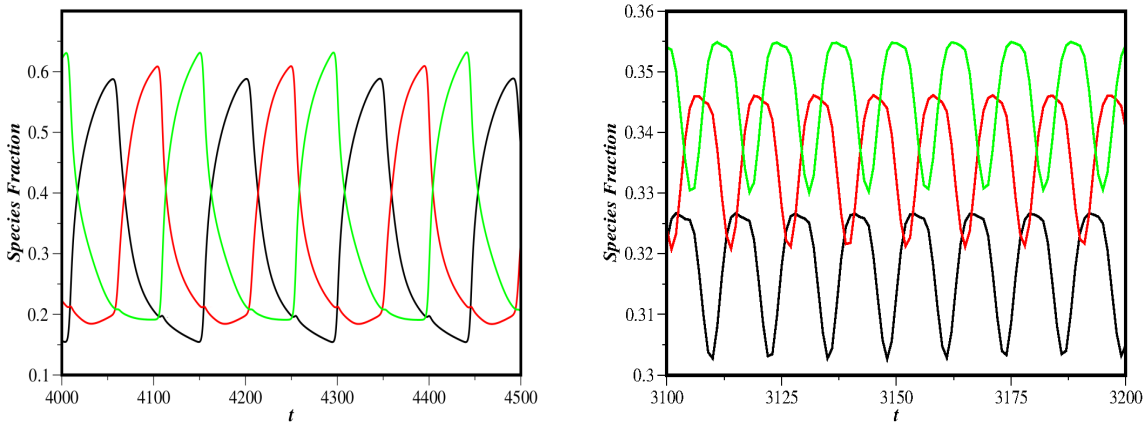

(a) (b)

Figure 11.2. Species fractions for (a) a 1D breather solution with $d_v = 1.1$ and (b) a 2D spiral solution with $d_v = 1.1$. Other parameters given in the text.

the initial conditions (11.4), $L = 60$, $\delta = 4$, and $(\alpha, \beta, \gamma) \approx (4.36, 3.28, 3.49)$ results in a breather solution with species fractions as shown in Figure 11.3a. As in the case of unequal diffusivities, it is not the most advantaged species (in this case, v, since β is the smallest coefficient) that dominates; instead, it is its controlling species (w). In fact, v is actually the least dominant species here. In 2D, using the same interaction parameters and value of L, a spiral solution arises from the initial conditions (11.5). As in the 1D case, there is clear dominance by species w (Figure 11.3b).

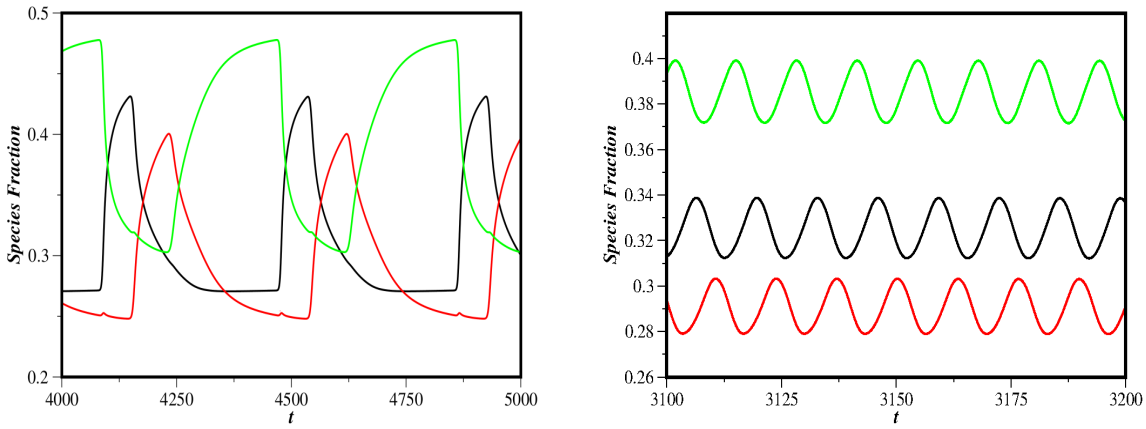

(a) (b)

Figure 11.3. Species fractions for (a) a 1D breather solution with asymmetric interaction coefficients and (b) a 2D spiral solution with asymmetric interaction coefficients. Parameters given in the text.

CHAPTER 12

Introduction to Systems with an Exceptional Species

Note: Much of the content in Chapters 12 through 15 was co-authored by A. Bayliss and V. A. Volpert and submitted to Applied Mathematics and Computation in a manuscript entitled "Cyclic Ecological Systems with an Exceptional Species." Used with permission.

In Chapters 12 through 15, N-species cyclic ecological models with an exceptionally weak or strong competitor are considered. The primary cases of interest are $N = 3$ and $N = 4$, though many results are also valid for larger N. The three-species model is

$$\frac{\partial u}{\partial t} = \nabla^2 u + u(1 - u - \alpha v), \tag{12.1a}$$

$$\frac{\partial v}{\partial t} = d\nabla^2 v + v(1 - v - \beta w), \tag{12.1b}$$

$$\frac{\partial w}{\partial t} = \nabla^2 w + w(1 - w - \alpha u); \tag{12.1c}$$

i.e., species v is exceptional in terms of its diffusivity or interaction coefficient. The four-species model is System (3.15), where v is again the exceptional species, reproduced here

for convenience:

$$\frac{\partial u}{\partial t} = \nabla^2 u + u(1 - u - \alpha v), \tag{12.2a}$$

$$\frac{\partial v}{\partial t} = d\nabla^2 v + v(1 - v - \beta w), \tag{12.2b}$$

$$\frac{\partial w}{\partial t} = \nabla^2 w + w(1 - w - \alpha z), \tag{12.2c}$$

$$\frac{\partial z}{\partial t} = \nabla^2 z + z(1 - z - \alpha u). \tag{12.2d}$$

For both systems, d will generally be taken as 1, so that all diffusivities are equal. This assumption will be relaxed in Chapter 16.

Systems (12.1) and (12.2) are appropriate for modeling the impact of an invasive species (this is done in [**59**] with a related six-species model), and the results presented here will be discussed in this context. However, these models may also be readily applied to explain certain social phenomena, as an alternative to models based on agents [**60**] or stochastic ODEs [**61**]. The interplay among alliances in these models has clear relevance to, for example, the formation of political alliances. In particular, the existence of an opinion or party that is exceptional in some way can have a notable effect on the viability of political strategies (see, e.g., [**62**]).

In the following chapters, the focus will be on invasion problems; i.e., situations in which one equilibrium state displaces an unstable or less robust equilibrium (see also Section 6.1 for a discussion of the $N = 2$ case). In some cases, this displacement occurs via a rigidly-propagating traveling wave, while in others, the propagation is dynamically evolving. The dominant feature in all considered exceptional species parameter regimes is some manifestation of a transcritical bifurcation, where there is a transfer of stability

from an alliance state, generally involving $N-1$ species, to the coexistence state, in which all species are present (see Chapter 13). Although the term "alliance" is sometimes used in the literature to refer to partnerships among species that are resistant to invasion (see, e.g., [**63, 64**]), the term is used here to describe any partnership, regardless of whether it can be disrupted. The behaviors that are described arise from patch initial conditions; mixed initial conditions could give rise to other behaviors (see, e.g., [**65, 66**]).

CHAPTER 13

State Stability in the Exceptional Species Regime

Two parameter regimes are considered for Systems (12.1) and (12.2) in the case $d = 1$.

13.1. Weak Exceptional Species

In this case, $\alpha < 1$ and $\beta > 1$, so that v is more vulnerable than the other species.

13.1.1. Three Species

The stability analysis for the three-species system in Section 3.2 shows the following:

(1) The extinction state (c_0) and the single-species states (c_u, c_v, c_w) are unstable.

(2) The two-species state $c_{vw} = (0, 1-\beta, 1)$ is never physical, since the density of v is negative.

(3) The two-species state $c_{uv} = (1-\alpha, 1, 0)$ is always physical, since $\alpha < 1$. However, it is unstable and disrupted by growth in w, since perturbations in w satisfy

$$\frac{d\tilde{w}}{dt} = \tilde{w}R, \quad R = 1 - \alpha(1-\alpha) > 0 \tag{13.1}$$

where $\tilde{w}$ denotes the linearized perturbation in w. Note that this state would be stable in a two-species community (excluding w).

(4) The two-species state $c_{uw} = (1, 0, 1-\alpha)$ is also always physical, with the linearized equation in v given by

$$\frac{d\tilde{v}}{dt} = \tilde{v}S, \quad S = 1 - \beta(1-\alpha), \tag{13.2}$$

so that c_{13} is stable if $S < 0$ and unstable if $S > 0$. The stability bound is then $S = 0$ or $\beta_S = \frac{1}{1-\alpha}$. If $\beta > \beta_S$, then species v cannot survive in combination with the other two species and the u-w alliance is stable.

(5) When $\beta < \beta_S$, v is strong enough to survive with the other two species, so that the coexistence state $c_{uvw} = (u_*, v_*, w_*)$ is stable. The coexistence state is also physical under these circumstances (when $\beta = \beta_S$, the coexistence state and the c_{uw} state coalesce; on the other hand, when $\beta > \beta_S$, the component v_* is negative). As mentioned in Section 3.2, the stability condition for the coexistence state is $(\alpha-1)^2(\beta-1) < 1$; thus, as β decreases through β_S, there is a transfer of stability from c_{uw} to the coexistence state. In other words, β_S is a transcritical bifurcation point. Analogous transcritical bifurcations occur in the $N = 4$ case, as well as when the exceptional species is less vulnerable than the others, as discussed below.

13.1.2. Four Species

The stability analysis for the four-species system in Section 3.3 shows the following:

(1) The extinction state (e_0), single-species states (e_u, e_v, e_w, e_z), non-competing alliances (e_{uw}, e_{vz}), and alliances of two competing species (e_{uv}, e_{uz}, e_{vw}, e_{wz}) are unstable (and e_{vw} is not physical).

(2) The three-species alliances e_{uvw}, e_{uvz}, and e_{vwz} are either unstable or nonphysical (or both).

(3) The three-species alliance $e_{uwz} = (1, 0, 1-\alpha(1-\alpha), 1-\alpha)$ is physical. Its stability depends on the linearization of the v equation,

$$\frac{d\tilde{v}}{dt} = \tilde{v}Q, \quad Q = 1 - \beta(1 - \alpha(1 - \alpha)). \tag{13.3}$$

The stability bound for the e_{uwz} state is thus $Q = 0$ or $\beta = \beta_Q = \frac{1}{1-\alpha+\alpha^2}$. The state is stable for $\beta > \beta_Q$.

(4) As β decreases through β_Q, the component v_* of the coexistence state $e_{uvwz} = (u_*, v_*, w_*, z_*)$ transitions from negative to positive; when $\beta = \beta_Q$, the coexistence state coalesces with the e_{uwz} state. Furthermore, the coexistence state is stable for $\beta < \beta_Q$, so that there is a transfer of stability from the e_{uwz} state to the coexistence state (i.e., β_Q is a transcritical bifurcation point). In other words, when $\beta > \beta_Q$, species v is too vulnerable to exist in alliance with the other three species. When $\beta < \beta_Q$, v is strong enough to exist stably with the other three species.

13.2. Strong Exceptional Species

In this case, $\alpha > 1$ and $\beta < 1$, so that v is less vulnerable than the other species.

13.2.1. Three Species

For the three-species system, the states c_0, c_u, c_v, and c_w are unstable, while c_{uv} and c_{uw} are not physical. The relevant two-species state is c_{vw}, which is always physical, and can

only be disrupted by growth in u. The linearized equation for u is

$$\frac{d\tilde{u}}{dt} = \tilde{u}T, \quad T = 1 - \alpha(1 - \beta). \tag{13.4}$$

The stability bound is $T = 0$ or $\alpha_T = \frac{1}{1-\beta}$. When α decreases through α_T, u becomes strong enough to exist together with the other two species. When $\alpha = \alpha_T$, there is a transcritical bifurcation leading to the transfer of stability from the c_{vw} state to the coexistence state.

13.2.2. Four Species

For the four-species system, the extinction state, single-species states, and two-species states are unstable or nonphysical (or both). The only possibly physical three-species state is the e_{uvw} state, which excludes species z. The following hold:

(1) The e_{uvw} state is physical if and only if

$$\beta_{PH} < \beta < 1, \quad \beta_{PH} = \frac{\alpha - 1}{\alpha} = \frac{\alpha^2 - \alpha}{\alpha^2}. \tag{13.5}$$

When $\beta = \beta_{PH}$, the e_{uvw} state coincides with the two-species e_{vw} state, which is unstable. On the other hand, when $\beta = 1$, the e_{uvw} state coincides with the e_{uw} non-competing alliance state, which is stable for $\beta > 1$; i.e., there is a transfer of stability from the e_{uvw} state to the e_{uw} state at the transcritical bifurcation point $\beta = 1$.

(2) The e_{uvw} state is stable if and only if

$$\beta > \beta_P = \frac{a^2 - \alpha + 1}{\alpha^2}. \tag{13.6}$$

Additionally, the e_{vz} alliance state is always stable for $0 < \beta < 1$ and $\alpha > 1$. Thus, for any $\alpha > 1$, there is bistability between the e_{vz} and e_{uvw} states if $\beta_P < \beta < 1$.

(3) For $\alpha > 1$ and $\beta > \beta_P$, the coexistence state is unstable when it is physical. On the other hand, coexistence is nonphysical for $\beta < \beta_P$.

CHAPTER 14

Three-Species Systems with an Exceptional Species

As in previous chapters, illustrations of spatial profiles employ the color scheme black for u, red for v, and green for w. In this chapter, the three-species system (12.1) is considered.

14.1. Weak Exceptional Species

First, consider the case of a stable u-w alliance (the c_{uw} state) displacing the v-only state (c_v) on a one-dimensional domain with $\alpha = 0.5$ and $\beta = 2.5$. The initial conditions are shown in Figure 14.1a. There is a small patch of the u-w alliance embedded in a community of v (note that the initial condition is independent of β, given the definitions of the c_{uw} and c_v states). As usual, the computation assumes periodic boundary conditions; however, the domain is sufficiently large that steady-state displacement speeds can be obtained before wraparound effects can occur.

The solution at $t = 1200$ is shown in Figure 14.1b. The solution is a rigidly-propagating traveling wave with the c_{uw} state displacing the c_v state with a speed very close to 2, as predicted by the methodology described in Section 4.2.1. Species v is actually displaced by a ripple of species w drawn out from the c_{uw} state (labeled GR in the figure). While it may look like a c_w buffer state, it is more appropriate to consider this region as a ripple that is just part of a non-monotone traveling wave, as discussed below.

In two dimensions, surrounding a circular patch of the c_{uw} state with a region of the c_v state results in an expansion of the c_{uw} patch (see Figure 14.2; refer to Table 14.1 for the key to this plot and all similar plots in Chapters 14 and 15). Note that this computation, as with other two-dimensional computations, was run with no-flux boundary conditions. As in the analogous one-dimensional computation, the c_2 state is directly displaced by a ripple of species w drawn out from the c_{uw} state (the light green ring in the figure). According to the analysis in Section 4.2.1, the linear speed of expansion should be approximately $2 - \frac{1}{R(t)}$, with $R(t)$ the radius of the inner patch at time t. Indeed, the computed speed $(1.98 - \frac{0.98}{R(t)})$ is very close to this approximation.

Color	**State**
Black	Strong u Dominance
Red	Strong v Dominance
Light Green	Strong w Dominance
Blue	Strong z Dominance ($N = 4$ only)
Dark Green	$c13$ state ($N = 3$ only)
Yellow	$d1010$ state ($N = 4$ only)
Purple	$d0101$ state ($N = 4$ only)
Orange	$d321$ state ($N = 4$ only)
White	Extinction
Magenta	Coexistence
Gray	Transition Region

Table 14.1. Color key for visualizations of two-dimensional solutions in Chapters 14 and 15. A species is considered to be strongly dominant if its density is at least 0.5 greater than the densities of the other species.

Next, consider the same one-dimensional problem as before, but with $\beta = 1.5$, so that the c_{uw} state is now unstable, while the coexistence state is stable (i.e., v is sufficiently strong that it can exist in combination with the other two species). The initial conditions

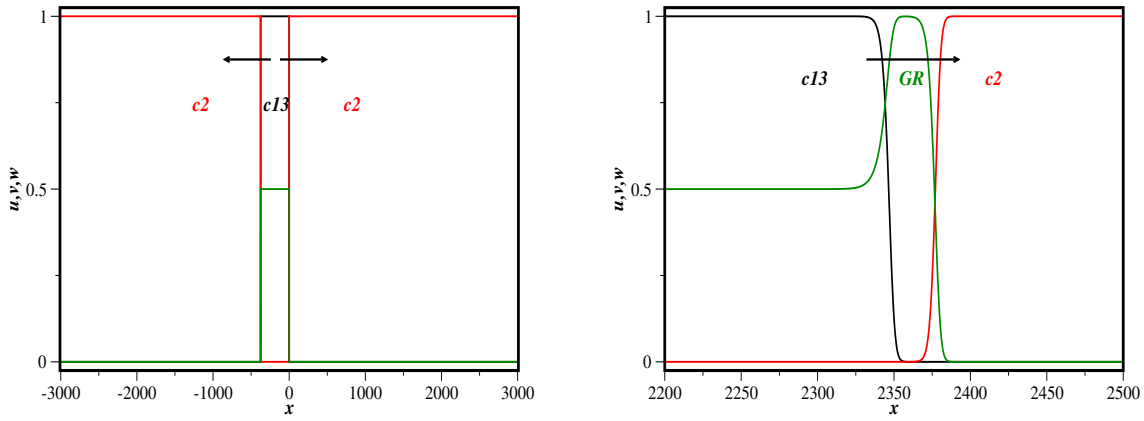

(a) (b)

Figure 14.1. (a) Initial condition for displacement of the c_v state by the c_{uw} state. $\beta = 2.5$ and $\alpha = 0.5$ so that v is too vulnerable to allow for a stable coexistence state. (b) Solution at $t = 1200$ over a subdomain. The green ripple GR directly displaces v.

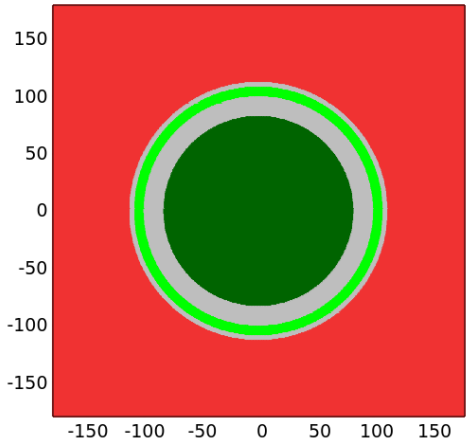

Figure 14.2. Expansion of a circular patch of c_{uw} into a region of c_v (dark green - c_{uw} state, gray - transition region, light green - strong domination by w, red - strong domination by v

.

are as shown in Figure 14.1a, so that the coexistence state is not initially present. For early times, diffusion of v into the c_{uw} state leads to formation of the c_{uvw} coexistence state. This state then expands to displace both the unstable c_{uw} state and the unstable c_v state. Thus, the incipient c_{uvw} patch propagates in both directions. The early-time behavior is shown in Figure 14.3a.

For later times (Figure 14.3b), the c_{uw} state has been completely displaced and the c_{uvw} state displaces the residual c_v state. As before, the actual displacement of v is due to ripples (in this case, a leading green ripple (GR) followed by a smaller amplitude black ripple (BR). This profile propagates rigidly with a speed very close to 2 and the solution is a non-monotone traveling wave.

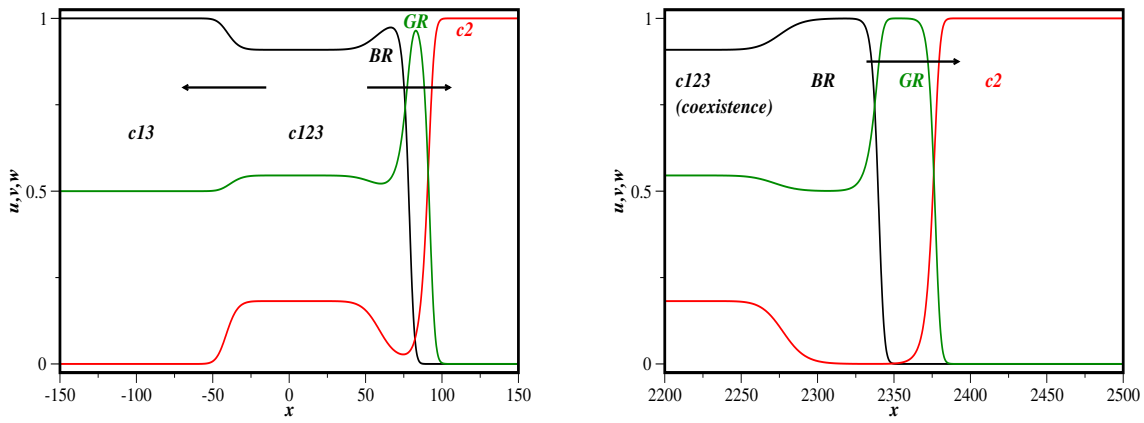

(a) (b)

Figure 14.3. (a) Solution at $t = 50$ over a subdomain for displacement of the c_{uw} and c_v states by the c_{uvw} state ($\alpha = 0.5$, $\beta = 1.5$). Ripples GR and BR represent the leading edge of the c_v displacement. (b) Solution at $t = 1200$ over a subdomain. The initial c_{uw} state has been completely displaced. The green and black ripples effect the displacement of the c_v state.

In order to determine the speed at which the c_{uvw} state displaces the c_{uw} state, a separate computation was run without the c_v state. The initial conditions are shown in Figure 14.4a. The solution at $t = 1400$ is shown in Figure 14.4b. There are now no ripples since such ripples would be ineffective in displacing an alliance state. The solution is a monotone traveling wave and its speed should be given by

$$s = 2\sqrt{1 + \beta(\alpha - 1)} \tag{14.1}$$

(see Appendix B.1) and should be just 1 for the parameters considered here. This fits the computed speed (0.992) well. Speeds were also computed for different values of β, all of which showed good agreement with (14.1).

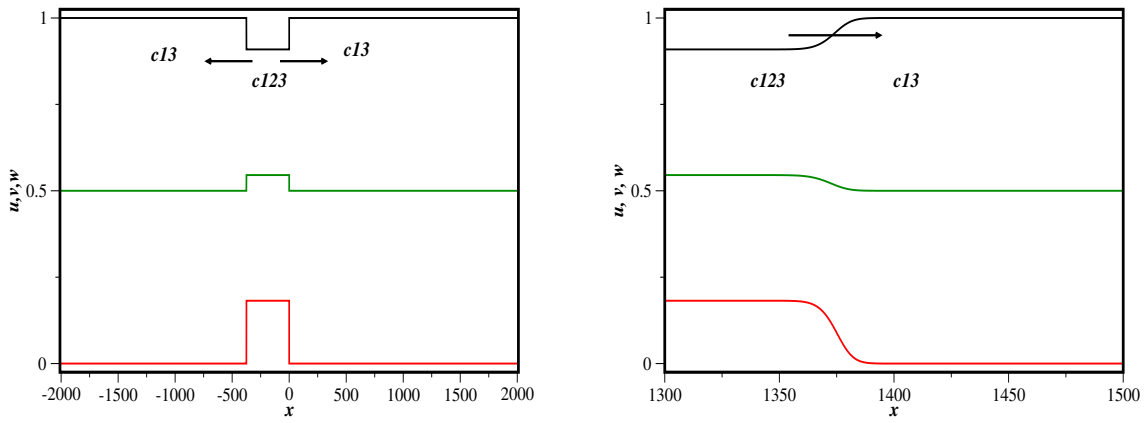

(a) (b)

Figure 14.4. (a) Initial conditions for displacement of the c_{uw} state by the c_{uvw} state ($\alpha = 0.5$, $\beta = 1.5$). (b) Solution at $t = 1400$ over a subdomain.

Consider now the onset and structure of the displacing ripples. To simplify the interpretation of the ripples, a related computation was run where the c_{uvw} coexistence state

directly displaced the c_v state with $\beta = 1.5$ (there was no initial c_{uw} state). The long-time results are very similar to the computation with the c_{uw} state adjacent to the c_v state (see Figure 14.3b).

A snapshot of the solution is shown in Figure 14.5a. Observe that the c_v state is displaced by a ripple of w (GR), which is in turn displaced by a ripple of u (BR), after which the c_{uvw} coexistence state appears. Note that these ripples are not single-species states. They are composed of a mixture of all three species, albeit with one species clearly dominating. This whole structure is a rigidly-propagating non-monotone traveling wave propagating with speed very close to 2, the speed associated with the displacement of the c_v state.

The origin of the ripples can be explained as follows. Consider the trailing edge of the retreating c_v state (point A in Figure 14.5a). At this point, v is large and, since v kills u in the competition scheme, u has been essentially eliminated. Since u controls w, this means that w is effectively uncontrolled, and a bubble of w rises from the coexistence mixture. This bubble increases until it settles on the pseudo-equilibrium of the unstable c_w state (GR in the figure), all the while killing off species v. The decline of v then allows u to increase and, since u kills w, this is accompanied by a decrease in w. The process continues until the solution settles near the pseudo-equilibrium of the unstable c_{uw} state (BR in the figure). The reduction in u then allows v to resurge and, with all three species present, the solution then settles on the stable c_{uvw} coexistence state.

This process is a consequence of the RPS dynamics. Diffusion regulates the speed of propagation (i.e., the propagation speeds of the ripples); however, the structure of the ripples is controlled by the dynamics (i.e., the kinetics of the system). In order to see

this, Figure 14.5b shows the solution as a function of t at the point A (trailing edge of the retreating c_v state). Contrast this figure with Figure 14.5c, which is the solution to the associated three-species ODE system with initial conditions corresponding to the PDE solution at the same point A at the time shown in Figure 14.5a (note that in Figure 14.5b, the initial time is set to zero to facilitate comparision with Figure 14.5c). Both solutions exhibit the same qualitative structure, though the timescales are of course different, since the timescales for Figure 14.5b involve the propagation speed of the traveling wave (close to 2), while the timescales for Figure 14.5c are completely controlled by the RPS dynamics.

14.2. Strong Exceptional Species

Consider the displacement of the c_u state by the c_{vw} state in one dimension with $\alpha = 2.5$ and $\beta = 0.5$ (note that the only stable state is the v-w alliance c_{vw}). The initial conditions consist of a small patch of the v-w alliance embedded in a u-only environment (Figure 14.6a). The solution at $t = 800$ is shown in Figure 14.6b. As before, ripples (in this case, a ripple of v (RR)) have developed to actually effect the displacement of u. Also as before, this ripple is only an approximation to the c_v state - a pseudo-equilibrium region rather than a true buffer state. The solution is again a rigidly-propagating non-monotone traveling wave with a speed of propagation very close to the predicted value 2.

Now, consider the same problem as above except with $\alpha = 1.5$, so that the c_{vw} state is now unstable, while the c_{uvw} coexistence state is stable. The initial conditions are the same as in Figure 14.6a. As before, for early times, the stable coexistence state displaces both unstable states (Figure 14.7a). For long times, the c_{vw} state has completely

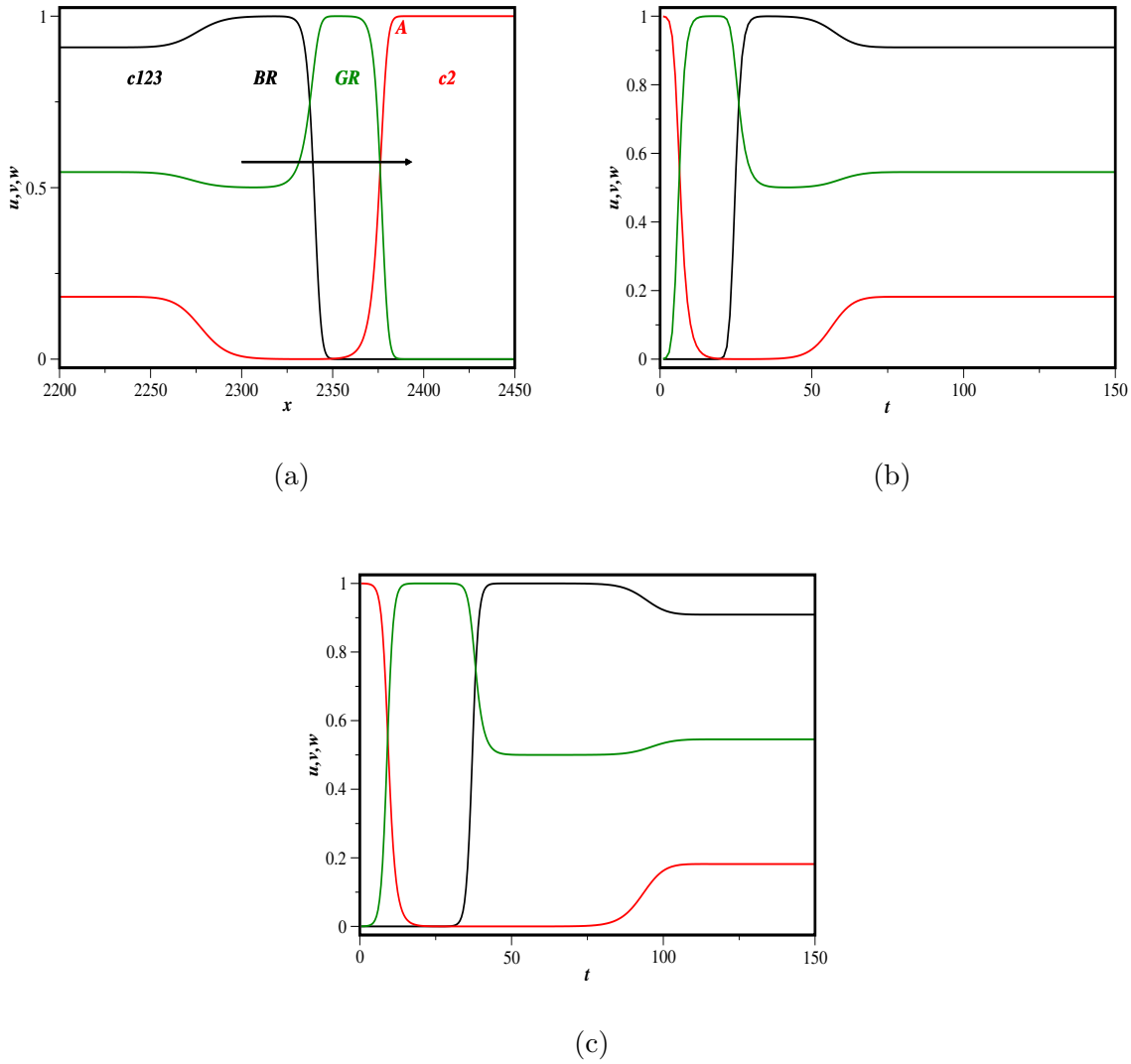

(a) (b)

(c)

Figure 14.5. (a) Solution over a subdomain for the displacement of the unstable c_v state by the stable c_{uvw} state at $t = 1200$ ($\alpha = 0.5$, $\beta = 1.5$). (b) Solution at point A in (a) as a function of time (initial time set to zero). (c) Solution of the associated ODE problem with the PDE solution at point A as the initial conditions.

disappeared and the c_u state is displaced by ripples emanating from the coexistence state

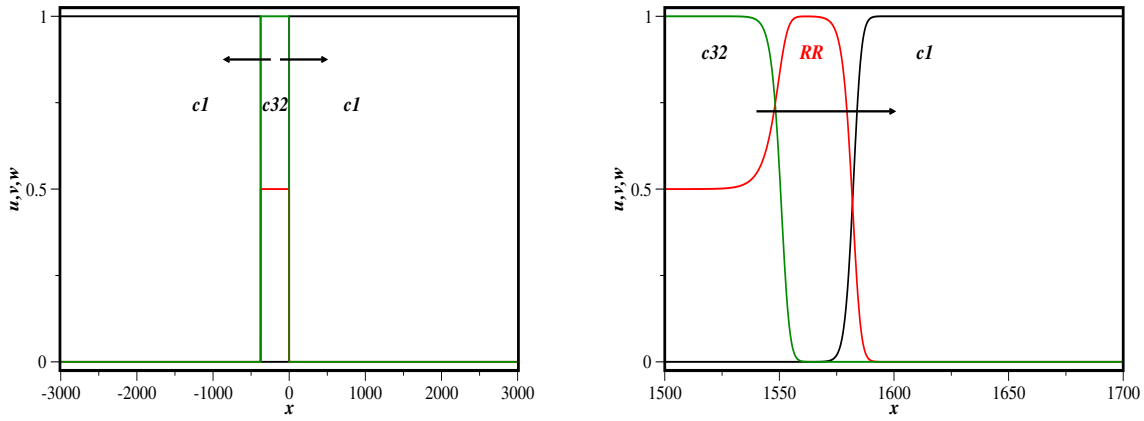

(a) (b)

Figure 14.6. (a) Initial conditions for displacement of the c_u state by the c_{vw} state ($\alpha = 2.5$, $\beta = 0.5$). Species u is too vulnerable to competition from v to allow for a stable coexistence state. (b) Solution at $t = 800$ over a subdomain. The red ripple RR effects the displacement of u.

(Figure 14.7b; ripples labeled RR and GR). The entire structure is a rigidly-propagating non-monotone traveling wave propagating with speed very close to 2.

This process is again primarily a consequence of the RPS dynamics. As before, diffusion regulates the speed of propagation (i.e., the timescale of the ripples); however, the structure of the ripples is controlled by the kinetics of the system. In order to see this, Figure 14.7c shows the solution at point A as a function of t. Contrast this figure with Figure 14.7d, which is the solution to the associated ODE system with the initial conditions given by the solution to the PDE solution at point A at the time shown in Figure 14.7b (as before, the initial time is set to zero in Figure 14.7c to facilitate comparison with Figure 14.7d). Both solutions exhibit the same qualitative structure, demonstrating the dominance of kinetic effects (competition) over diffusion. The results illustrate how

a simple ODE model can shed light on the structure of traveling waves for the invasion problem (indeed, the diffusion terms can be thought of as a perturbation to the ODE problem, as shown in [**67**]).

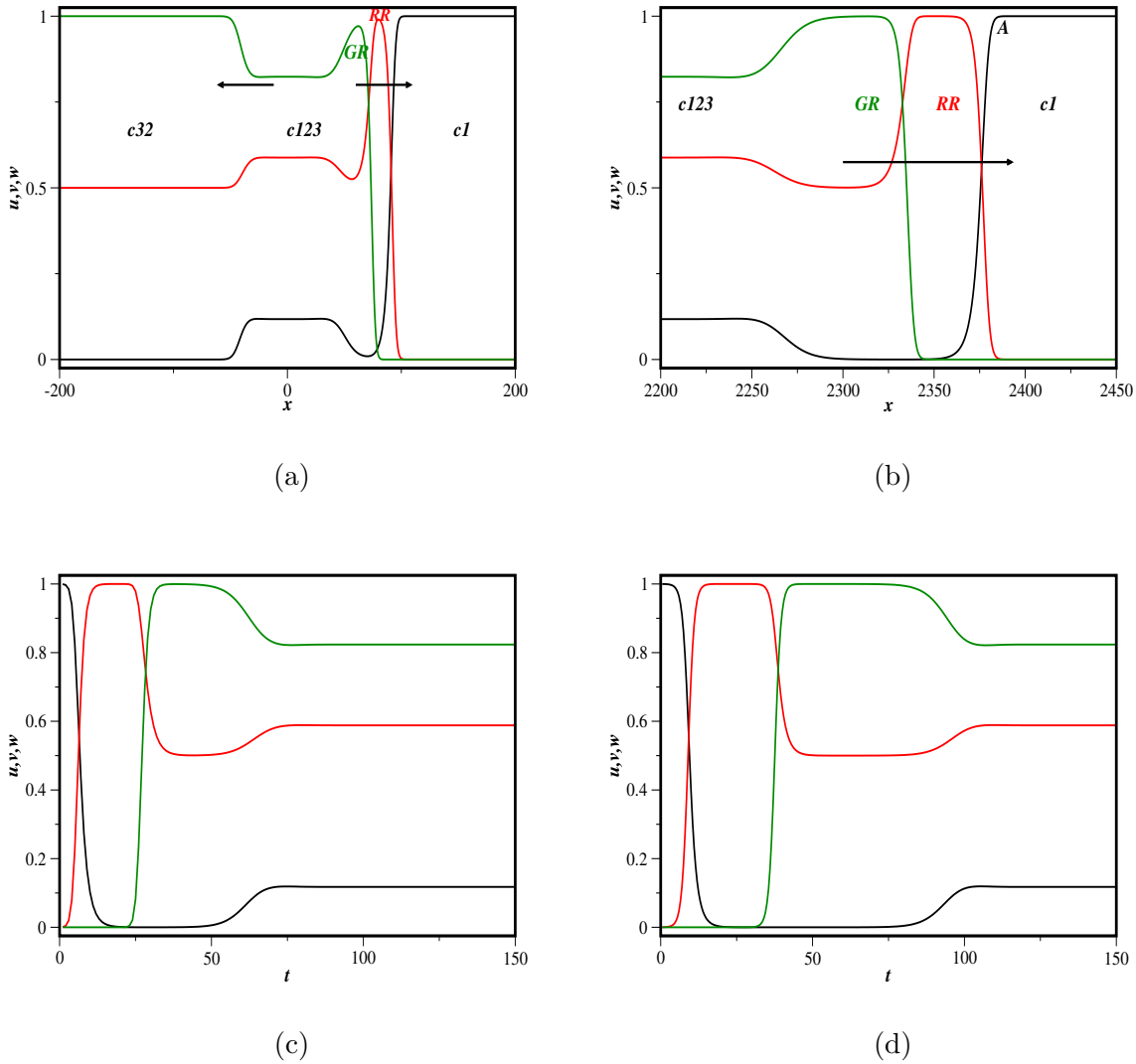

Figure 14.7. (a) Solution at $t = 50$ over a subdomain for the displacement of the c_{vw} and c_u states by the c_{uvw} state ($\alpha = 1.5$, $\beta = 0.5$). The ripples RR and GR represent the leading edge of the c_u displacement. (b) Solution at $t = 1200$ over a subdomain for the displacement of the unstable c_u state by the c_{uvw} state. (c) Solution at point A as a function of time (initial time set to zero). (d) Solution of the associated ODE system using the PDE solution at point A as the initial conditions.

CHAPTER 15

Four-Species Systems with an Exceptional Species

In the figures of spatial profiles presented in this chapter, the color scheme is extended to include blue for species z. Here, the four-species system (12.2) is considered.

15.1. Weak Exceptional Species

Consider the one-dimensional invasion of the e_{uwz} state into a patch of only v in the case where $\alpha = 0.85$ and $\beta = 1.5$, so that the e_{uwz} state is stable (the v-only state d_v is unstable, as always). The initial conditions are shown in Figure 15.1a. There is a small patch of the e_{uwz} alliance embedded in an extensive v-only environment.

The e_{uwz} state does not displace the e_v state directly, as shown in Figure 15.1b. This is presumably because u is killed by v and cannot survive in a stable configuration with species v near its carrying capacity. Instead, an unstable v-w-z alliance (the e_{vwz} state) forms and actually effects the displacement of v by incorporating v into the three-species alliance. This unstable buffer state expands against the e_v state at a speed close to 2, as previously described in [**20**]. The speed of displacement of the unstable e_{vwz} state by the stable e_{uwz} state is estimated to be approximately 1.16 (Appendix B.2). Thus, the region occupied by the unstable e_{vwz} state is continually expanding, a process termed dynamical stabilization [**68, 69**], and the solution is not a traveling wave (note the clear contrast with the three-species model). Similar behavior has been observed for predator-prey models [**27**], where it was shown that expansion of the unstable state would ultimately stop due

to noise (roundoff error in terms of computation and stochastic perturbations in physical systems). In this case, the computation was not run long enough for roundoff effects to manifest and the unstable state is thus clear, well-defined, and expanding in time.

The solution for $\beta = 1.1$ (so that e_{uwz} is unstable and e_{uvwz} is stable) at $t = 800$ is shown in Figure 15.1c. Even though the initial conditions involve only the e_{uwz} state (as in Figure 15.1a), the e_{uwz} state is rapidly displaced by the e_{uvwz} coexistence state. Again, an expanding buffer region of the e_{vwz} state forms, except now it is displaced by the coexistence state.

Finally, consider the case where the target (displaced) state is the e_{vz} alliance state. The initial conditions are shown in Figure 15.2a and the solution with $\beta = 1.5$ is shown in Figure 15.2b. There is now no buffer state. This is due to the fact that species u must be present in order to displace species z in the alliance state. The estimate for the speed of displacement of the e_{vz} alliance state by the e_{uwz} state is 0.77 (see Appendix B.3), and the computed speed is very close to this value.

15.2. Strong Exceptional Species

15.2.1. Solutions

Here, only the three relevant states e_{uvw} (stable for $\beta_P < \beta < 1$), e_{uw} (unstable for $\beta < 1$), and e_{vz} (stable) are considered. For all computations in this section, $\alpha = 3$ and $\beta < 1$. Under these conditions, the e_{vz} state displaces the other two states. This is not surprising, since v is the strongest species and the e_{vz} alliance state contains the largest population of v. In particular, the e_{vz} alliance displaces the e_{uw} alliance.

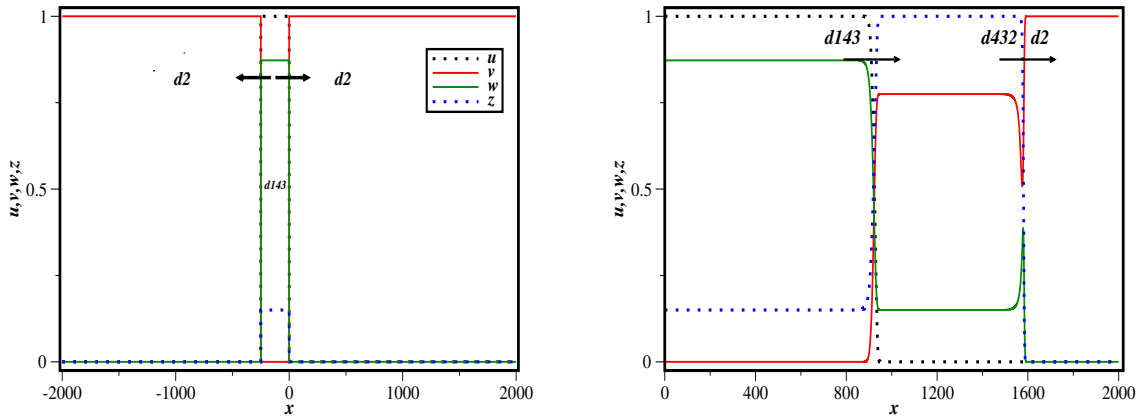

(a) (b)

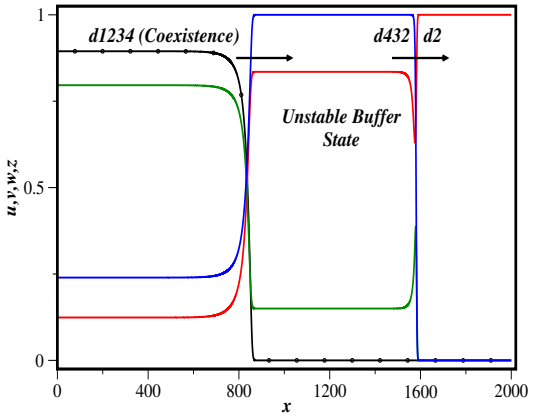

(c)

Figure 15.1. (a) Initial conditions for displacement of the e_v state. (b) Solution at $t = 800$ over a subdomain ($\alpha = 0.85$, $\beta = 1.5$). The unstable buffer state is expanding since it displaces the e_v state more quickly than it is displaced by the e_{uwz} state. (c) Solution at $t = 800$ over a subdomain ($\alpha = 0.85$, $\beta = 1.1$). The advancing stable state is the coexistence state.

The initial conditions for all one-dimensional computations in this section are shown in Figure 15.3. There is a small patch of the e_{vz} state embedded in a region of the e_{uw} state.

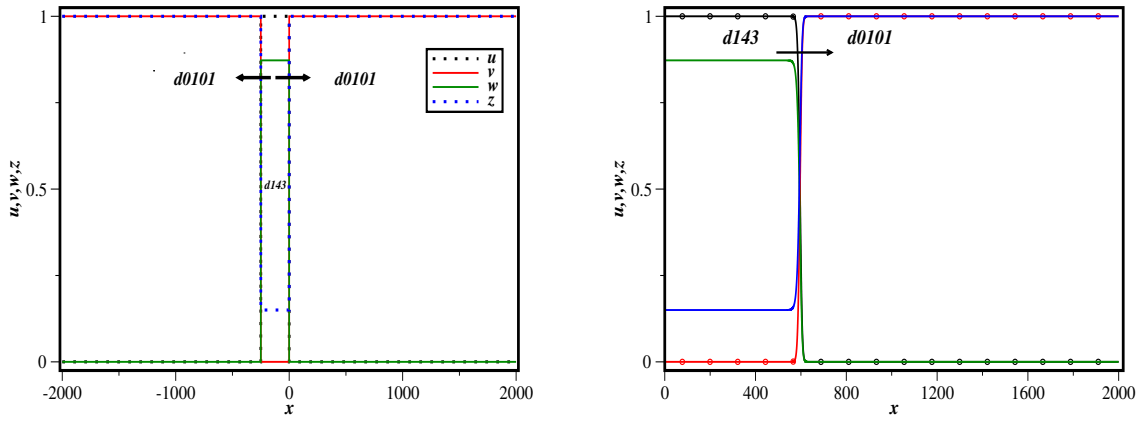

(a) (b)

Figure 15.2. (a) Initial conditions for displacement of the e_{vz} state. (b) Solution at $t = 800$ over a subdomain, illustrating displacement of the e_{vz} state by the e_{uwz} state ($\alpha = 0.85$, $\beta = 1.5$). There is now no buffer state; the e_{uwz} state effects the displacement directly.

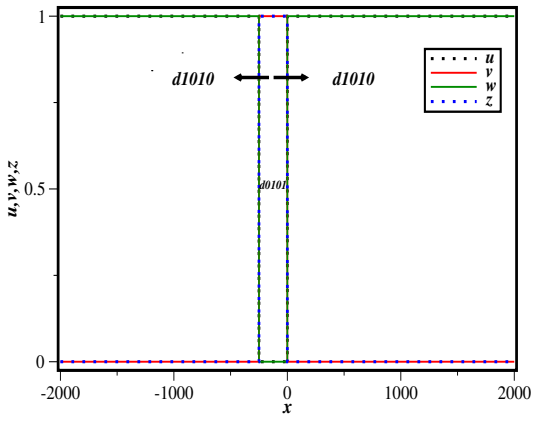

Figure 15.3

First, consider the nature of the displacement of the e_{uw} alliance. The two allied species v and z both will penetrate the e_{uw} alliance; however, they will not progress at

the same rate. Species v should progress ahead of z because it is less vulnerable to the competition. This allows for v to mix with the already available u and w in the e_{uw} region. As a consequence, if β is such that the three-species e_{uvw} state is stable, the u-v-w alliance can form as a buffer state ahead of the advancing e_{vz} alliance. When this happens, there are then two displacements: (i) e_{uvw} displaces e_{uw} with speed s_{uvw} and (ii) e_{vz} displaces e_{uvw} with speed s_{vz}. However, this will not occur for all values of β. The conditions for the buffer state to form are (i) the e_{uvw} state must be stable and (ii) the speed e_{uvw} needs to be greater than the speed e_{vz}. If both these conditions hold, then the e_{uvw} buffer state is continually increasing and the solution will not be a rigidly-propagating traveling wave. Conversely, if either of these conditions is false, then no buffer state forms and the solution is expected to be a rigidly-propagating traveling wave.

For $\alpha = 3$, $\beta_P \approx 0.77$. Consider the case $\beta = 0.85$ so that the e_{uvw} state is stable. Figure 15.4a shows the formation of a buffer region of the e_{uvw} state between the two alliance states e_{uw} and e_{vz}. The points A and C in the figure are where u and w, respectively, first rise above 0.9999, scanning from left to right. The points B and D are where v and z, respectively, first drop below the same threshold (also scanning from the left). Point A is taken as the trailing edge of the retreating u-w alliance. Thus, in this case, the velocity of point A represents the speed of displacement of the e_{uw} state by the e_{uvw} buffer state (i.e., s_{uvw}). Similarly, the point C represents the trailing edge of the e_{uvw} buffer state, while the points B and D represent the leading edge of the advancing e_{vz} alliance state. Points B, C, and D propagate with the same velocity s_{vz}. When a buffer state forms, point A propagates faster than the other three points and the extent of the buffer state increases in time. The solution, in this case, is a dynamically-evolving wave. This can be

seen in Figure 15.4b, where the solution is shown for a later time. The region occupied by the e_{uvw} buffer state has now greatly increased in extent.

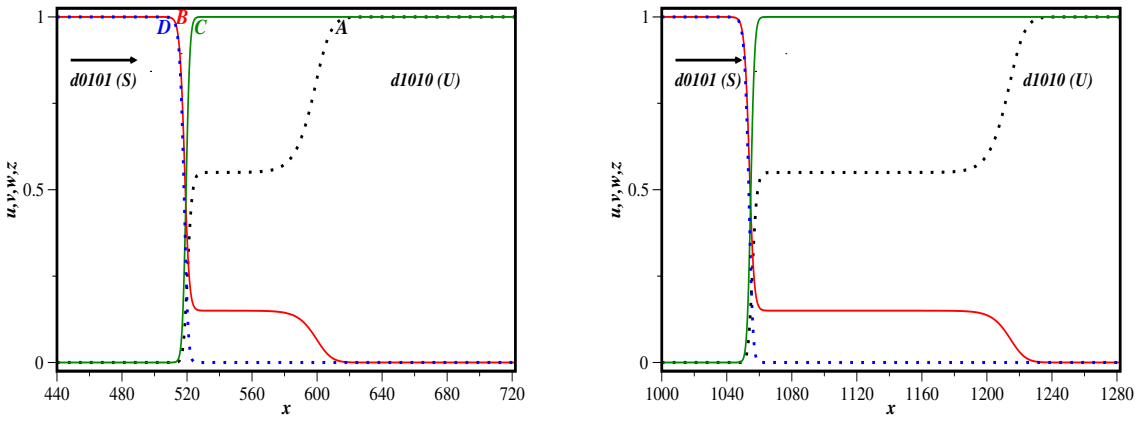

(a) (b)

Figure 15.4. (a) Buffer e_{uvw} state at $t = 800$ ($\beta = 0.85$). Solution shown over a subdomain. (b) Buffer state at $t = 1600$.

In two dimensions, taking $\beta = 0.85$ and initial conditions consisting of a circular patch of the e_{vz} alliance surrounded by the e_{uw} alliance (Figure 15.5a) also leads to the formation and expansion of a e_{uvw} buffer region, as shown in Figures 15.5b and 15.5c.

Going back to the one-dimensional problem, when point A propagates with the same speed as the other three points, there is no buffer state. The entire spatial profile propagates rigidly in time. There is, of course, a transition region between the advancing e_{vz} state and the retreating e_{uw} state, and the solution shows some semblance of trying to form a buffer state, but no such state forms and the transition region does not change over time. Figure 15.6a shows the solution when s_{vz} is greater than s_{uvw} ($\beta = 0.95$) so that there is no intermediate buffer state.

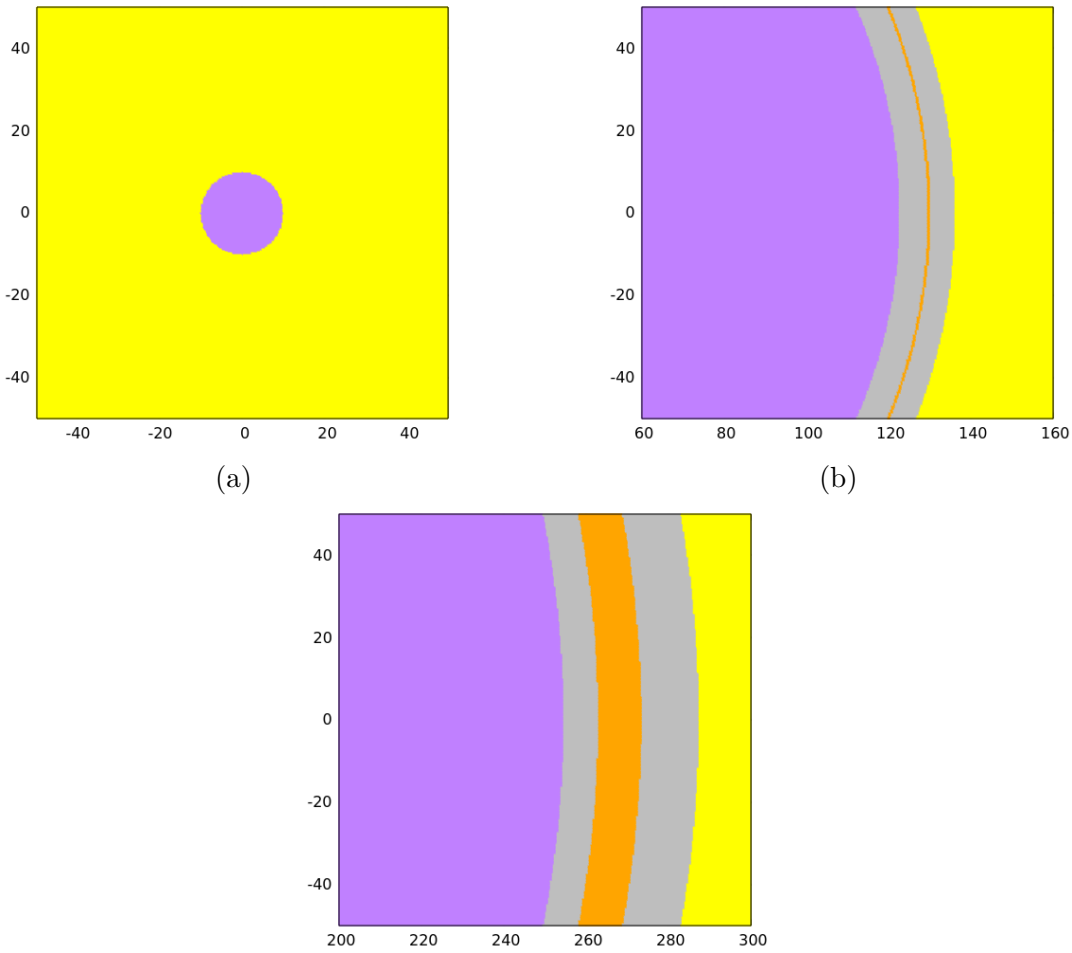

Figure 15.5. (a) Initial conditions for 2D computation resulting in buffer state formation (purple - e_{vz} alliance, yellow - e_{uw} alliance). (b) Formation of e_{uvw} buffer state (orange region). (c) Buffer state at a later time.

Another example where the buffer state does not form is shown in Figure 15.6b. In this case $\beta = 0.76$ so that the e_{uvw} state is unstable. Note that in this case, the transition region is more complicated than in Figure 15.6a because there are more signs of the failed attempt at formation of the e_{uvww} state; i.e., v (red) and u (black) appear to be trying to form the state, but they fail. However, the four points A, B, C, and D all travel

with the same speed, the transition region is unchanged in time, and the solution is a rigidly-propagating traveling wave.

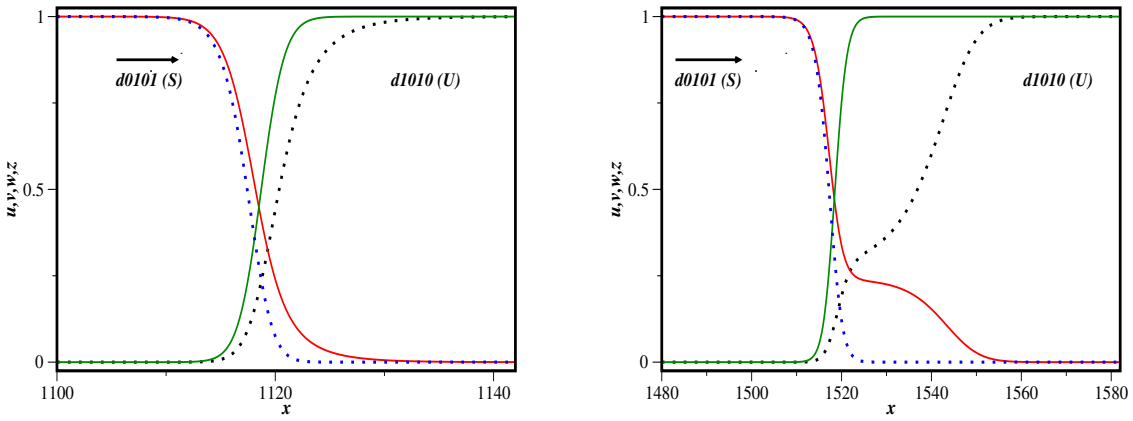

(a) (b)

Figure 15.6. (a) Traveling wave solution without e_{uvw} buffer state at $t = 2400$ ($\beta = 0.95$). (b) Traveling wave solution without e_{uvw} buffer state at $t = 1600$ ($\beta = 0.76$).

15.2.2. Speeds

For $\beta < 1$, there are two situations in which a stable state displaces an unstable state: (i) e_{vz} directly displaces e_{uw} (no buffer state forms) and (ii) e_{uvw} displaces e_{uw}. Application of the methodology discussed in Section 4.2.1 leads to the prediction (see Appendix B.4)

$$s = 2\sqrt{1-\beta}; \tag{15.1}$$

i.e., the estimate is the same in both cases (recall that the propagation speed of a pulled front depends only on the properties of the displaced state). The computed and estimated front speeds as a function of β are shown in Figure 15.7a. The buffer e_{uvw} state exists

for $0.77 < \beta < 0.95$ and in this regime, the solution is a dynamically-evolving wave, rather than a traveling wave. In general, the estimate agrees well with the computed speeds, though it fails near $\beta = 1$, since the front is not pulled in this regime. In order to confirm that the presence of the e_{vz} state did not impact the speed of the displacement of e_{uw} by e_{uvw}, additional computations were run without the e_{vz} state (i.e., the initial conditions involved just a small patch of the e_{uvw} state embedded in the e_{uw} state) in the regime where e_{uvw} is stable. In this case as well, the estimate agrees very well with the computed speeds (Figure 15.7b). The displacement of e_{uw} by e_{uvw} appears to be completely unaffected by the presence of a trailing e_{vz} state.

Finally, Figure 15.7c shows the front speed for $\beta > 0.95$ up to $\beta = 3$. In this case, the solution is a traveling wave and the front speed appears to be continuous as β passes through unity, where the e_{uw} state becomes stable (dashed vertical line in the figure). In two dimensions, speeds of displacement of an unstable state by an expanding circular patch show a clear dependence on the radius as discussed in Section 4.2.1.

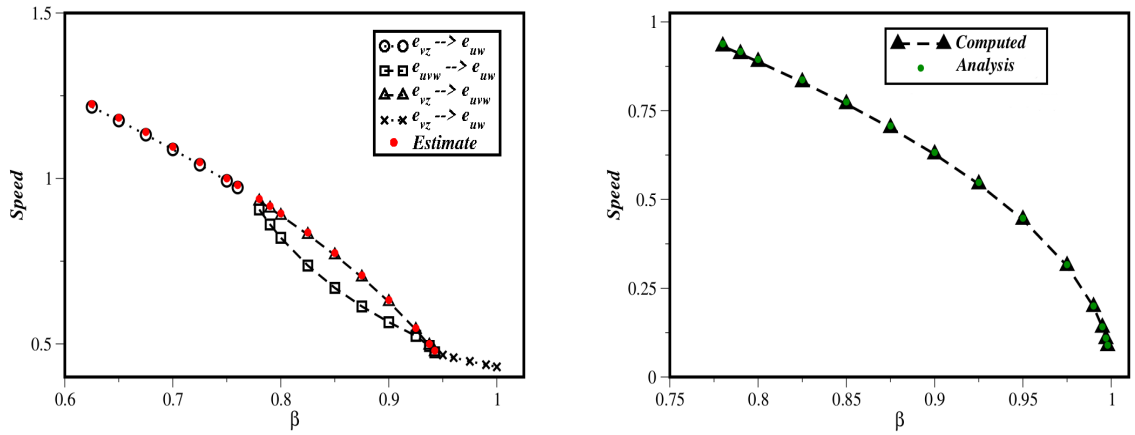

(a) (b)

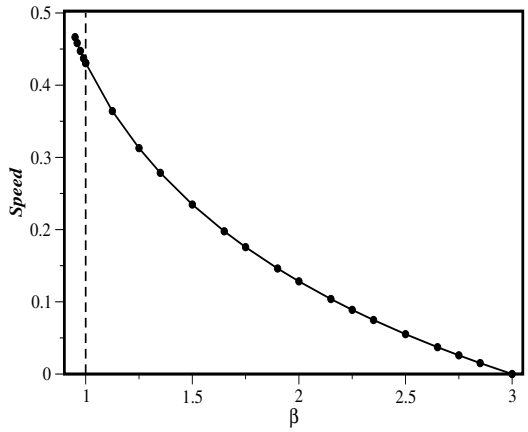

(c)

Figure 15.7. (a) Speeds associated with the displacement of the e_{uw} alliance state for $\beta < 1$. For those values of β where there are two such speeds, an expanding e_{uvw} state forms. (b) Speeds for the direct displacement of the e_{uw} state by the e_{uvw} state. (c) Speeds associated with the displacement of the e_{uw} alliance state for $\beta < \alpha = 3$. The retreating e_{uw} state is unstable to the left of the dashed vertical line and stable to the right.

CHAPTER 16

Exceptional Mobility

Note: Much of the content in this chapter was co-authored by A. Bayliss. Used with permission.

Here, the three-species system (3.6) is considered with all interaction coefficients equal, but with a difference in mobility for species v. Specifically,

$$\alpha = \beta = \gamma = 9, \quad u_* = v_* = w_* = 0.1, \quad d_w = 1, \quad d_v = d. \tag{16.1}$$

All computations described in this chapter were run on the domain $-L \leq x \leq L$, where $L = 360$, with initial conditions

$$u(0,x) = \left(1 + \varepsilon \cos\left(\frac{\pi x}{L}\right)\right) u_*, \tag{16.2a}$$

$$v(0,x) = \left(1 + \varepsilon \cos\left(\frac{\pi x}{L} + \frac{\pi}{2}\right)\right) v_*, \tag{16.2b}$$

$$w(0,x) = \left(1 + \varepsilon \cos\left(\frac{\pi x}{L} + \pi\right)\right) w_*, \tag{16.2c}$$

where $\varepsilon = 0.3$. Thus, the only variable is the diffusivity of species v (d). As before, the color scheme of black for u, red for v, and green for w is employed, with the species often referred to by these colors.

16.1. Single Patch Splitting

Consider the case $d = 0.9$. According to analysis of patch propagation in [**16**], for a three-patch array, the red/black interface should propagate with speed $2\sqrt{d} < 2$, while the black/green and green/red interfaces should propagate with speed 2. As a result, the black patch is expected to expand at the expense of the red patch, while the green patch remains constant in extent.

The species fractions $\bar{u}(t)$, $\bar{v}(t)$, and $\bar{w}(t)$ (refer to Section 8.3.1 for the definitions of these fractions) for this case are shown in Figure 16.1a. After a brief initial period during which the species self-segregate to form three patches (not shown in the figure), the expected behavior does occur for some time; however, it terminates when the red patch becomes sufficiently thin, at which point the analysis in [**16**] is no longer valid. Next, the red patch abruptly expands and the black patch abruptly contracts, which is collectively referred to as an "event." Following the event, the black patch again begins expanding at the expense of the red and the process repeats. A total of five events are depicted in Figure 16.1a. The events are due to patch splitting (see Section 8.3.4); specifically, red splits the black patch at each event. There is one splitting per cycle and the behavior is periodic with a period of approximately 7000 units of time.

Figure 16.1b is a blowup of Figure 16.1a around the first event. The spatial profile at point 1 ($t = 9800$) is shown in Figure 16.2a. At this time, the solution is a three-patch array with the black patch expanding at the expense of the red. The solution at point 2 ($t = 9873$) is shown in Figure 16.2b. Here, red has split the black patch via back-diffusion through the green. The previously large black patch is being split into two patches, labeled D and S in the figure. Patch D is doomed, as it will be surrounded by

red. Patch S will survive and ultimately expand. Note that the splitting is preceded by a slight weakening of the green patch (compare Figures 16.2a and 16.2b), allowing red to back-diffuse through green and effect the split.

At point 3 ($t = 9880$, Figure 16.2c), the split is complete. There are now five patches: the doomed and surviving black patches, the newly formed red patch (r in the figure), the original red patch (R), and the green patch. At this time, the red patch is expanding, despite the mobility disadvantage of species v.

At point 4 ($t = 10000$, Figure 16.3a), the doomed black patch D is on the verge of being eliminated. There are still two red patches, but they will merge upon elimination of D. This is in the final stages of red's expansion. At point 5 ($t = 10500$, Figure 16.3b), D has been eliminated and the red patches have merged, restoring the three-patch array. This is at the beginning of the expansion of the surviving black patch S. Finally, at point 6 ($t = 11500$, Figure 16.3c), the expansion of the black patch at the expense of the red is clearly visible as the cycle approaches completion.

16.2. Cyclic Patch Splitting

Consider the case $d = 0.88$. The species fractions are shown in Figure 16.4a. There is again an early transient during which the species self-segregate and form a patch array. There is then a period of time for which the patches propagate as expected (i.e., the black patches expand at the expense of the red). However, a transition to a periodic solution occurs around $t = 2500$ and the behavior persists as long as it was computed. The dynamics of the solution can best be ascertained by looking at the spatial behavior

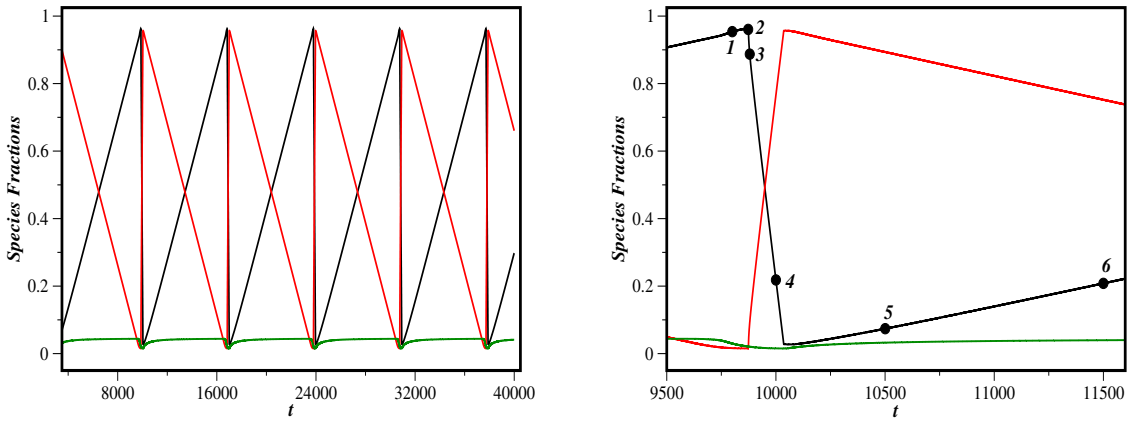

(a) (b)

Figure 16.1. (a) Species fractions with $d = 0.9$. (b) Blowup of species fractions around an event.

of the points marked on Figure 16.4b, which depicts the species fractions over roughly two periods.

At point 1 ($t = 3000$), red is dominant, followed by black, and then green. The spatial profiles are shown in Figure 16.5a. There are five patches, rather than three: two red, two black, and one green. This is generally the case in the regime $0.8 < d \leq 0.88$. The large black patch (labeled D in the figure) is doomed, as it is surrounded by its controlling species red (refer to the arrows in the figure signaling the direction of motion). Note that this is consistent with Figure 16.4b, since at point 1, the species fraction of red is increasing, while that of black is decreasing.

At point 2 ($t = 3020$), the doomed black patch (D) has shrunk considerably, as it is being consumed by its red neighbors (Figure 16.5b). At point 3 ($t = 3040$), D has been completely consumed and green has begun to split the (now wide) red patch (Figure

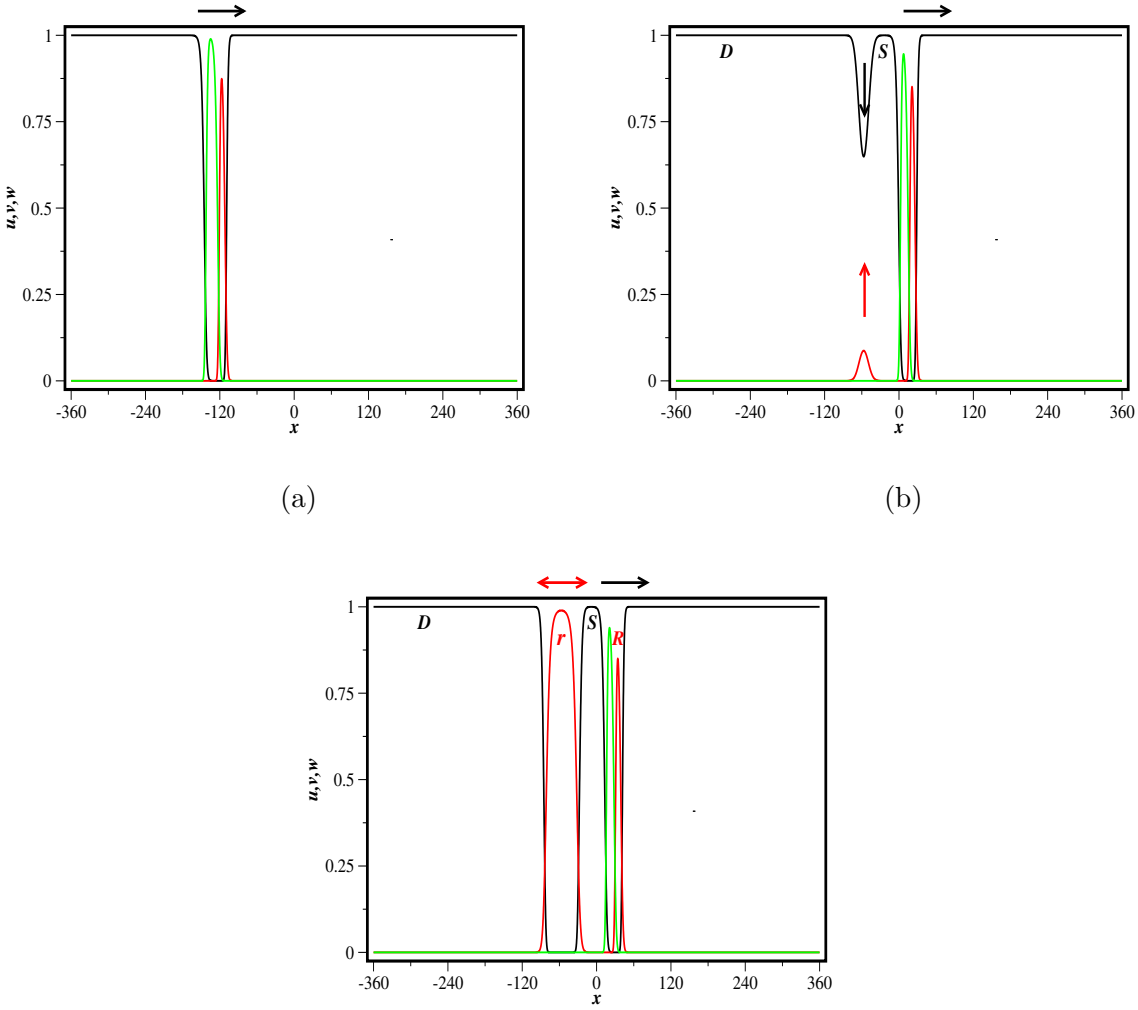

Figure 16.2. (a) Solution for $d = 0.9$ at $t = 9800$ (point 1 in Figure 16.1b). (b) $t = 9873$ (point 2). (c) $t = 9880$ (point 3).

16.5c). This is the first of three patch splitting events in a cycle. Shortly after, when red is split (point 4, Figure 16.5d), the five-patch array will be restored, this time with two red patches, two green patches, and one black patch. The red patch marked D in the

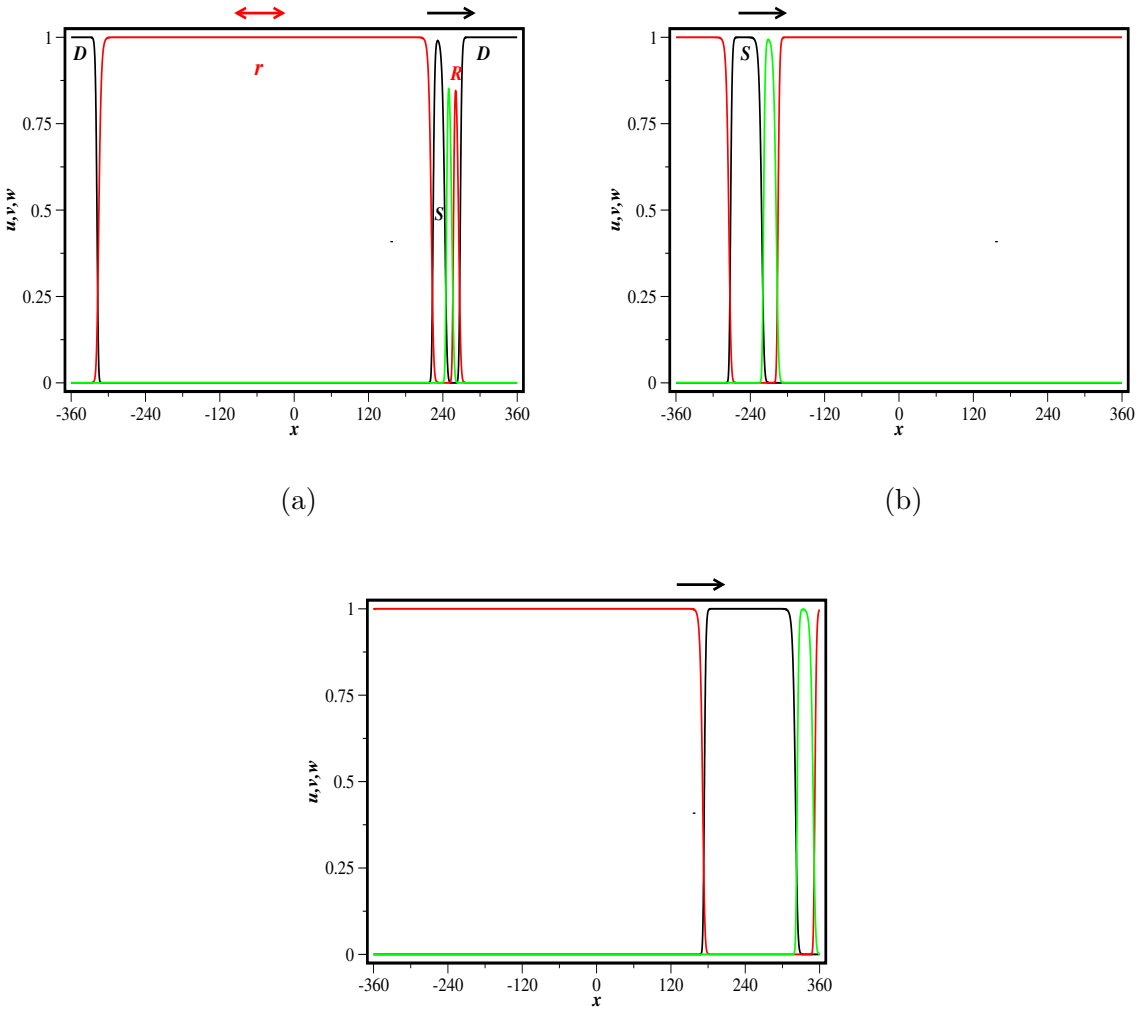

Figure 16.3. (a) Solution for $d = 0.9$ at $t = 10000$ (point 4 in Figure 16.1b). (b) $t = 10500$ (point 5). (c) $t = 11500$ (point 6).

figure is doomed, since it is surrounded by green neighbors. The species fraction of green will subsequently increase as it consumes the doomed red patch.

For $3050 \leq t \leq 3180$, the species fractions of both green and black are increasing. The fraction of green increases rapidly as green consumes the doomed red patch, while that of

black increases slowly as a result of its mobility advantage over red (see points 4 through 6 of Figure 16.4b). At point 6 ($t = 3190$), the black patch has broadened and black has begun to split the wide green patch (Figure 16.6a - second patch splitting event). Two green patches will be formed, one of which is doomed (green D). Thus, when the split is completed, there will be a short period of time for which there are seven patches. This is not the case when green splits a red patch (refer to Figure 16.5c) and it is likely due to the mobility bias leading to the expansion of black patches relative to the red. The slow growth of black (point B in Figure 16.6a), in turn, reduces the growth of the green patch it pursues (G). This delays the elimination of the doomed red patch (red D). Moreover, the fraction of red is slowly decaying due to its mobility disadvantage with respect to black.

At point 7 ($t = 3250$), the five-patch array has been restored, as the doomed red patch has been completely consumed. There is now explosive growth in black and rapid decay in green as black eliminates the doomed green patch. The splitting of a black patch by red, the third and final splitting event in the cycle, begins at point 8 ($t = 3310$). As can be seen in Figure 16.4b (around point 8), there are differences in the decline of black as compared to the declines of the other two species:

(1) Black begins its decline at a lower level than the other two species at a time when the amount of green is still considerable. Indeed, at this time, the doomed green patch (green D in Figure 16.6b) is still of considerable extent.

(2) In the early stages of black's decline, the decline is gradual. There is subsequently a rapid decline due to patch splitting by red.

These effects are likely also a result of the mobility bias of black over red. The black patch that has not been split (B in Figure 16.6b) is still expanding due to its mobility advantage over red. As a a result, the red patch (R) is squeezed into a small spatial region, enhancing its back-diffusion into the large black patch, thus accelerating the splitting of the black patch by red. Notice that the peaks of green and red between the black patches S and B are considerably lower than the other peaks.

At point 9 ($t = 3400$), the five-patch array has been restored. The fraction of black is rapidly declining as the doomed black patch is consumed by its red neighbors. The surviving black patch is labeled S in Figure 16.6c. When D is eliminated, red will be dominant, completing the cycle, as a red patch will then be split by green (Figure 16.6d). This process appears to be strictly periodic, having been run for many more cycles than what is shown here. The fact that the interval of black's dominance is smaller than the dominance interval for the other two species, as well as the fact that black's decline occurs at a lower level than that of the other two species, leads to the ostensibly advantaged species (black) being the least dominant of the three species (see Table 16.1). Similarly, the fact that red's peak occurs at a higher level (recall from Figures 16.5b and 16.5c that red is the only species that can eliminate its victim's doomed patch prior to being split) leads to red being the most dominant species on average, indicating survival and dominance of the weakest, as discussed in Chapter 11.

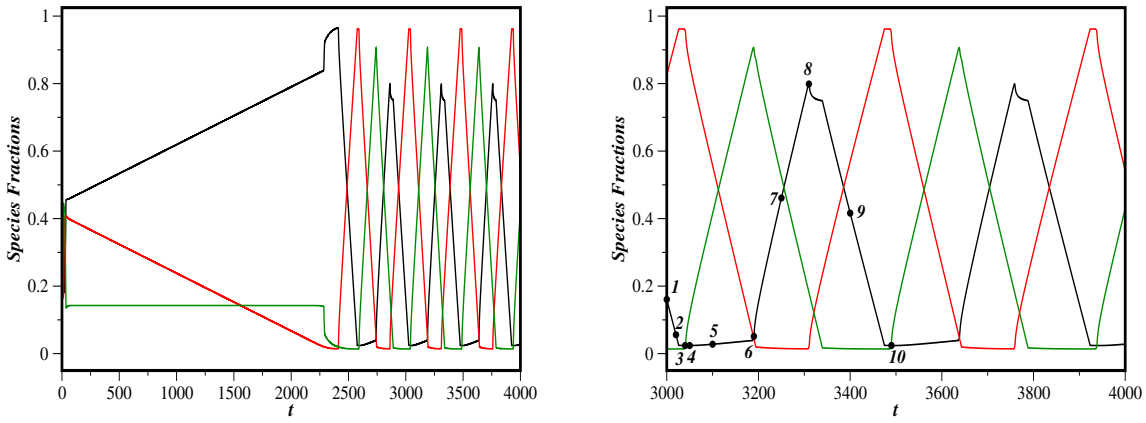

(a) (b)

Figure 16.4. (a) Species fractions with $d = 0.88$. (b) Species fractions over the interval $3000 \leq t \leq 4000$.

16.3. Increased Spatial Complexity

As d decreases, the spatiotemporal patterns become more complex, eventually leading to chaos (chaos has been found for $d = 0.7$, for example). For $d = 0.8$, the solution is ordered and the species fractions are periodic, although the spatial profiles are substantially more complex than for larger values of d.

The species fractions for the steady-state behavior in this case are shown in Figure 16.7a. The species fractions are periodic and the temporal profiles are relatively simple compared to those seen when $d = 0.88$. As for larger values of d, the species initially self-segregate and form an array of patches, with black patches expanding at the expense of the red ones (Figure 16.7b).

The dynamical behavior can be understood by considering the 7 points indicated in Figure 16.7a. Points 1 and 7 are intended to illustrate the periodicity of the solution

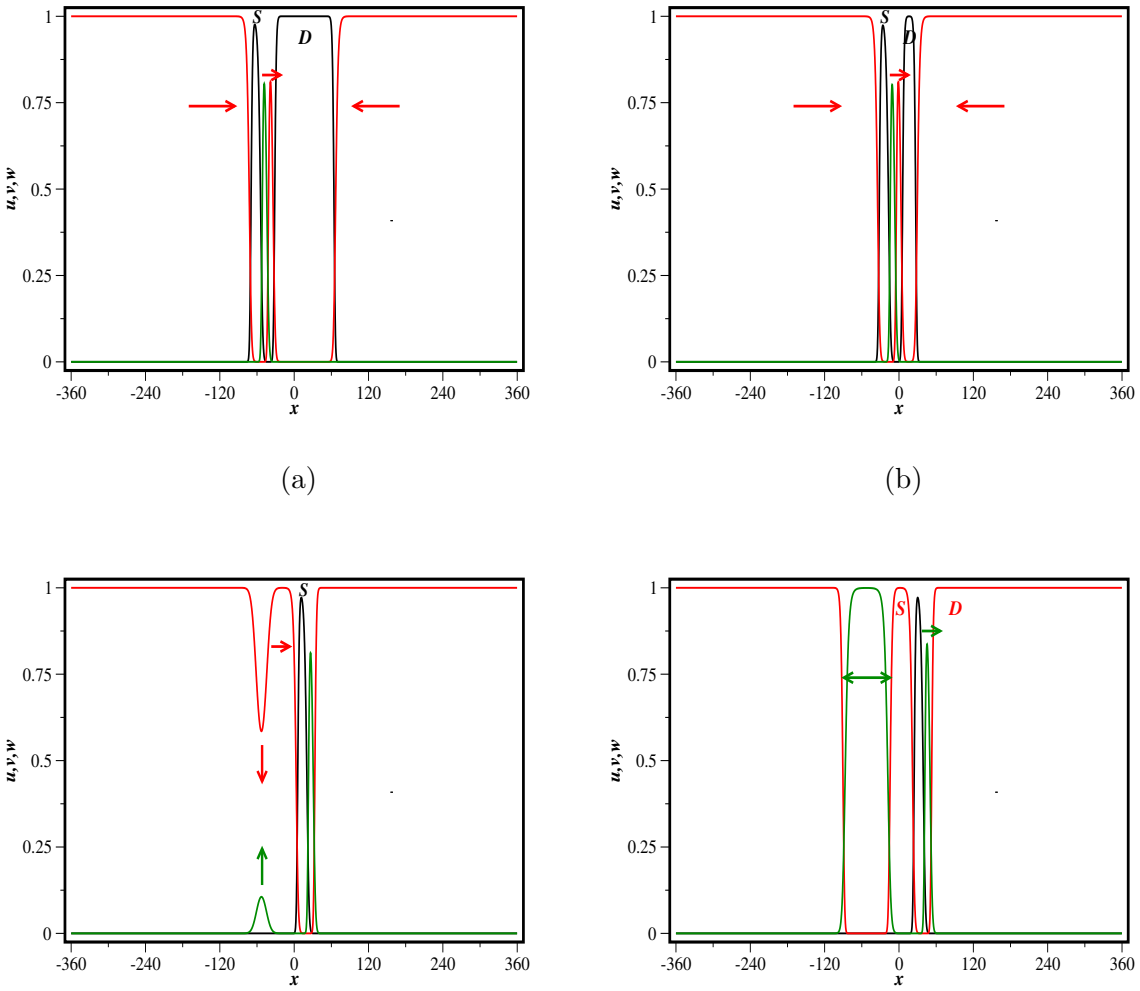

(a) (b)

(c) (d)

Figure 16.5. (a) Solution for $d = 0.88$ at $t = 3000$ (point 1 in Figure 16.4b). (b) $t = 3020$ (point 2). (c) $t = 3040$ (point 3). (d) $t = 3050$ (point 4).

(disregarding a phase shift in space). At point 1 ($t = 9763.5$), the fraction of red has reached a maximum. At this time, the solution consists of a nine-patch array, which is the general state of the solution outside of interruptions due to events. The nine-patch array does not adhere to the rock-paper-scissors order (e.g., a red patch followed by black

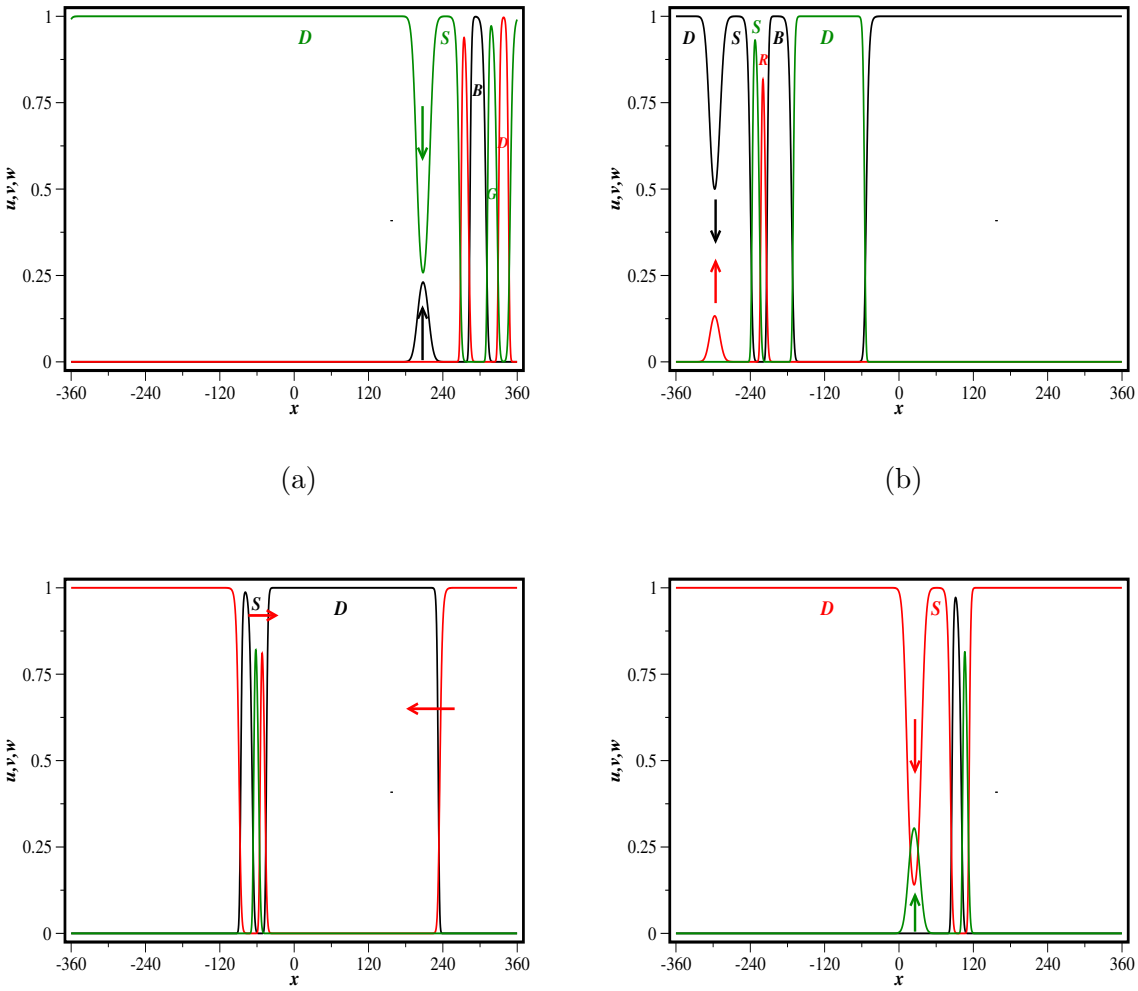

Figure 16.6. (a) Solution for $d = 0.88$ at $t = 3190$ (point 6 in Figure 16.4b). (b) $t = 3310$ (point 8). (c) $t = 3400$ (point 9). (d) $t = 3490$ (point 10).

followed by green, and son on), as shown in Figure 16.8a. Proceeding from left to right (and considering the periodicity of the domain), the fourth patch is black, rather than the expected green, causing the cyclic order to switch from green-black-red to black-red-green. As a result, the red patch labeled B in the figure is bi-directional, pushing in both

directions against its black neighbors. As a consequence, another red patch (labeled D in the figure) is doomed, since it is surrounded by two green neighbors.

The general situation is a nine-patch array with a dominant species (in terms of the species fractions) having both a bi-directional patch and a doomed patch. The specific preferred species switches from red to green to black due to brief events, where the bi-directional patch is split by its controlling species while the doomed patch is consumed.

At point 2 ($t = 9780$), red's time as the preferred species ends, as the former B patch is split by green (Figure 16.8b). In addition, the doomed red patch (D), while not yet consumed, is rapidly shrinking. This is the first of the three events that occur in each cycle. At point 3 ($t = 9830$), a nine-patch array has again been established, but with green as the dominant species (Figure 16.8c). A second event occurs around point 4 ($t = 9840$), where the green patch B is split by black, while green patch D is almost entirely consumed. At point 5 ($t = 9880$), a nine-patch array has once again been established, but this time with black as the dominant species. Black's time as the preferred species is terminated by the third event (point 6, $t = 9895$), in which black patch B is split by red, while the doomed patch D is on track to be eliminated (Figure 16.9a). The elimination of the doomed patch is delayed, relative to the first two events. This is a direct consequence of red's mobility disadvantage - it takes more time for red to eliminate the doomed black patch because red/black interfaces propagate more slowly than the other types of interfaces. Finally, at point 7 ($t = 9920.57$), the original nine-patch array has been restored, with red as the preferred species (Figure 16.9b). Comparison with Figure 16.8a shows the periodicity of the solution modulo a shift in space.

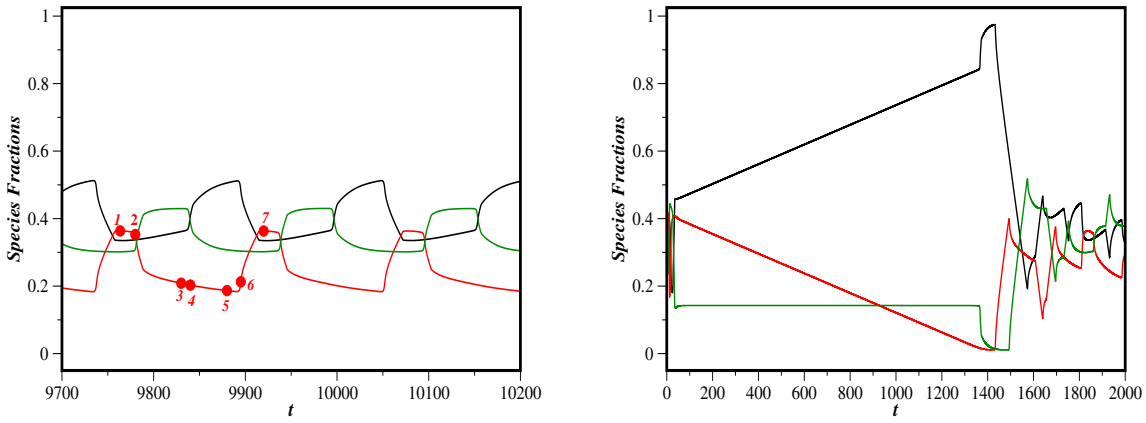

(a) (b)

Figure 16.7. (a) Species fractions with $d = 0.8$. (b) Species fractions over the interval $0 \leq t \leq 2000$.

16.4. Timescales and Dominance

In Table 16.1, the computed periods and temporal averages of the species fractions are tabulated for selected values of d. For simplicity, let U, V, and W denote the temporal averages of the species fractions over a cycle for u, v, and w, respectively, and let T denote the period of the cycle. The species fractions in the neighborhood of $d = 0.88$ clearly indicate the boundary between the regimes of single patch splitting and cyclic patch splitting.

Increasing d leads to longer periods. Black grows because of the difference in the speeds of red/black and black/green interfaces. As d increases, this difference decreases, and it takes longer for black patches to reach their maximum extents. While this is not surprising, increasing d (making red more mobile) leads to a more pronounced advantage of black over red. It may be that as red becomes more mobile, it becomes harder for red

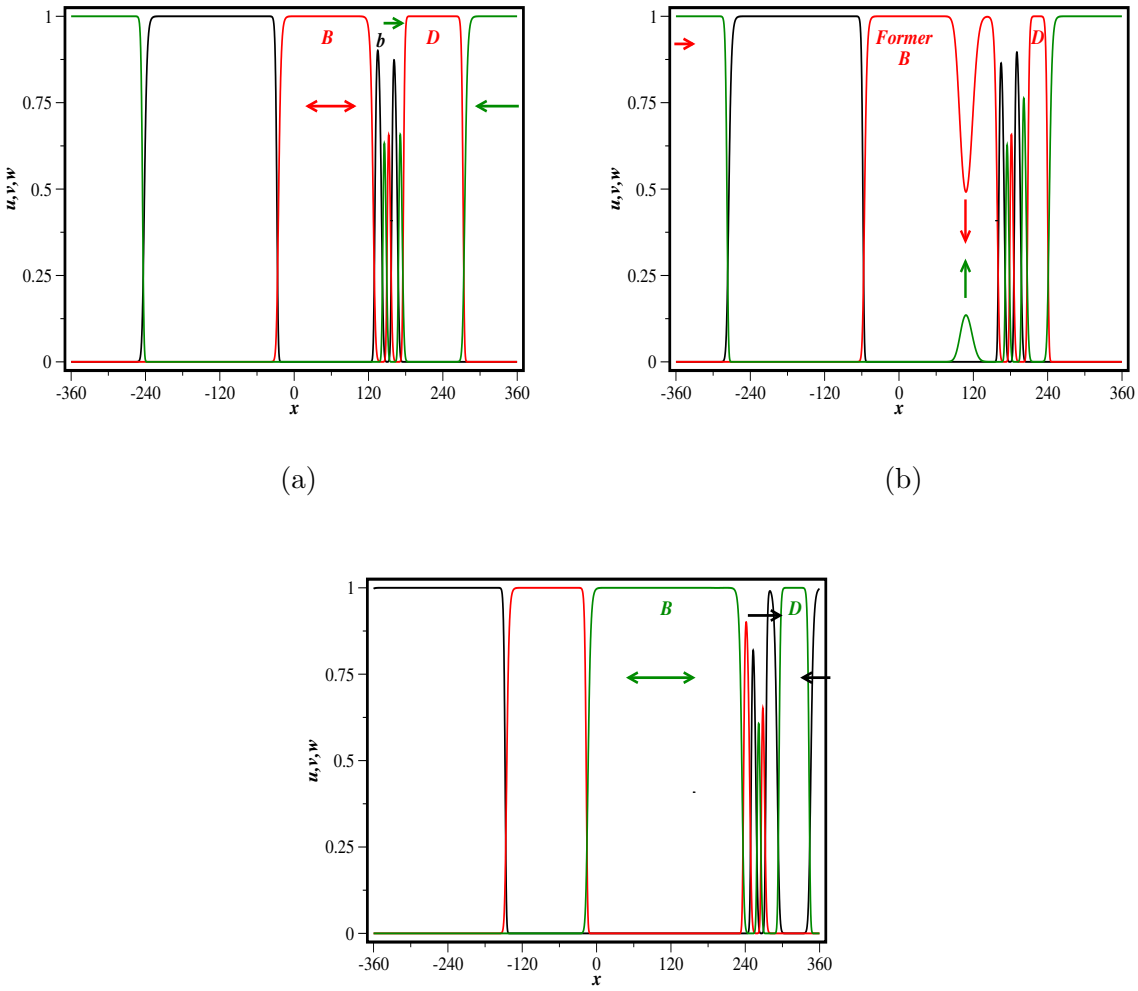

Figure 16.8. (a) Solution for $d = 0.88$ at $t = 9763.5$ (point 1 in Figure 16.7a). A nine-patch array is established with a bi-directional red patch. (b) $t = 9780$ (point 2). First event, where red is split by green. (c) $t = 9830$ (point 3). The nine-patch pattern has been re-established, but now with a bi-directional green patch.

to back-diffuse through green patches, since there is more red to be consumed within the green patch. Thus, splittings of black patches are delayed, leading to a greater advantage

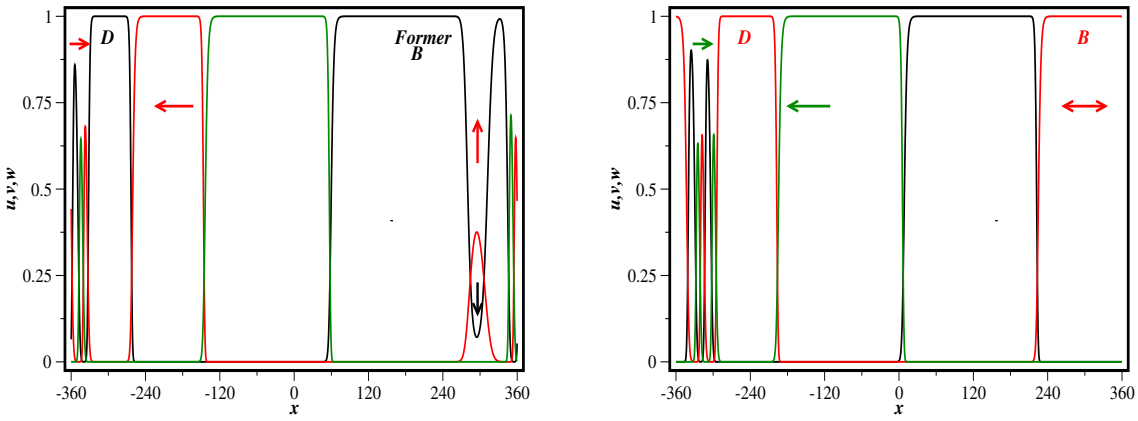

(a) (b)

Figure 16.9. (a) Solution for $d = 0.8$ at $t = 9895$ (point 6 in Figure 16.7a). Third event, where black is split by red. (b) $t = 9920.57$ (point 7). The nine-patch array has been re-established with a bi-directional red patch. The solution is the same as in Figure 16.8a except for a phase shift in space, demonstrating the periodicity of the species fractions.

of black in terms of temporal averages of the species fractions. For $0.98 \leq d < 1$, splitting does not occur at all - after black crests, the patch widths stabilize and the solution is an asymmetric traveling wave (i.e., a propagating three-patch array with the patches having differing, but constant, widths; see Section 8.3.2). To demonstrate this, Figure 16.10a shows the species fractions over a long interval for $d = 0.97$ (for which splitting occurs) and Figure 16.10b shows the species fractions for $d = 0.98$. In this second figure, the fraction of black initially increases and then levels off after the black patch reaches its maximum extent.

d	U	V	W	T
0.80	0.403	0.245	0.352	157
0.83	0.361	0.288	0.351	216
0.85	0.319	0.286	0.395	285
0.87	0.296	0.352	0.352	384
0.88	0.298	0.384	0.318	449
0.89	0.480	0.480	0.0393	6338
0.90	0.481	0.479	0.0400	6963
0.92	0.484	0.476	0.0406	8668
0.95	0.488	0.470	0.0420	13735
0.97	0.495	0.462	0.0430	22781
0.98	0.945	0.0275	0.0275	NA
0.99	0.935	0.0326	0.0326	NA
1.00	0.454	0.403	0.144	NA

Table 16.1. Periods and spatial averages as a function of d. Periods rounded to the nearest whole number. Temporal averages rounded to three significant figures.

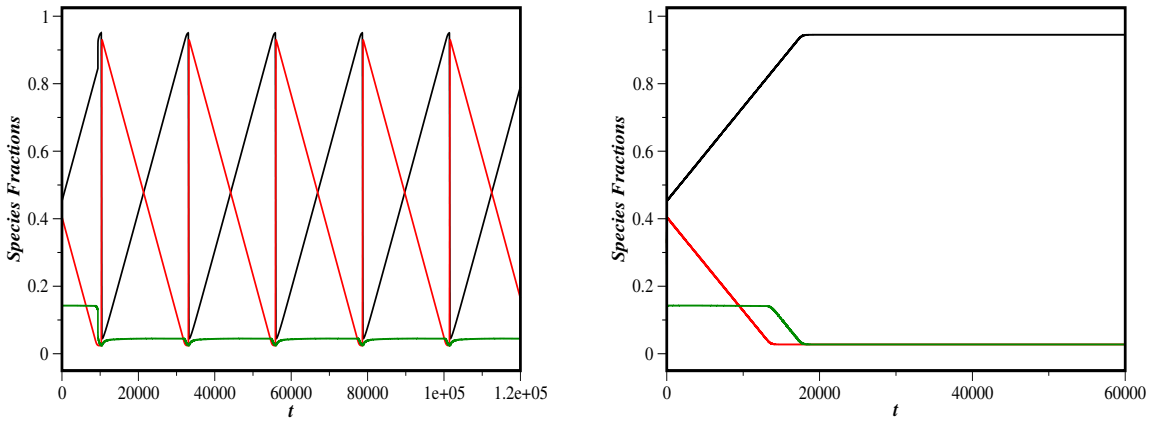

(a) (b)

Figure 16.10. (a) Species fractions for $d = 0.97$. (b) Species fractions for $d = 0.98$.

16.5. More Mobile Exceptional Species

If $d > 1$, then v is more mobile than the other two species. Consider the case $d = 1.1$. A three-patch array forms, at which point it should be expected that the red/black interface move with speed $2\sqrt{d} > 2$, while the black/green and green/red interfaces propagate with speed 2. Thus, the red patch should grow at the expense of the black, while the green patch should remain constant. Based on the results for $d < 1$, this should happen until the black patch is sufficiently thin, at which point some form of patch splitting (starting with green splitting red) should occur. The solution initially behaves as expected, as shown in Figure 16.11a. Red collapses around $t = 3200$, accompanied by explosive growth in green. However, in this case, there are no further splittings. The final steady-state solution is an asymmetric traveling wave with green dominant, followed by red and black. Even though red could be considered the most advantaged species and black the most disadvantaged, it is in fact green that is dominant, since there is no further patch splitting. Recall that the same problem on the domain $-60 \leq x \leq 60$ leads to a breather solution, in which the three patches periodically expand and contract, with green again the dominant species (see Section 11.1).

In order to see what happens, consider the points 1, 2, and 3 indicated in Figure 16.11a. Point 1 ($t = 3245$) is very close to the peak in the fraction of red. At this time, the splitting of the red patch by green has started (Figure 16.11b). Green splits the red patch into two patches, labeled S and D in the figure. Patch D is doomed, since it is surrounded by green, and S will survive at its shrunken level. At point 2 ($t = 3350$), red is nearly finished with its decline, while the green patch has expanded significantly. At point 3 ($t = 3450$), a three-patch array has again been established (Figure 16.11c). This array

propagates rigidly around the domain. It may be that it is too difficult for black to back-diffuse through the red patch to split the green patch, since red is so mobile compared to black; i.e., it could be that the more mobile red can inhibit the initial penetration of black into its patch.

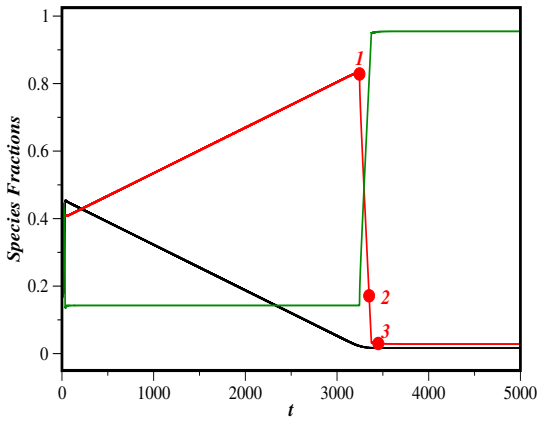

(a)

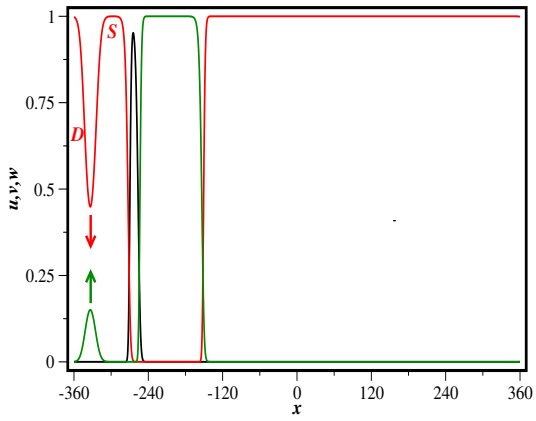

(b)

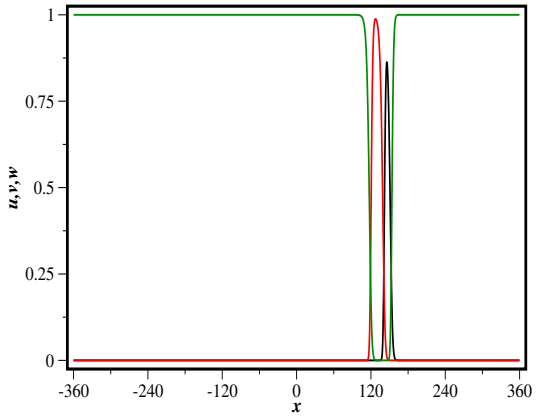

(c)

Figure 16.11. (a) Species fractions with $d = 1.1$. (b) Solution at $t = 3245$ (point 1 in the previous figure). The splitting of red by green has just initiated. (c) Solution at $t = 3450$ (point 3). The three-patch array has been restored and an asymmetric traveling wave has formed.

CHAPTER 17

Exceptionality in 2D: Expanding Coexistence Patch

In this chapter, the expansion of a disc of the coexistence state into an uninhabited region is considered for the three-species system (3.6) with species v an exceptional species. For all computations presented here, the domain is the square $[-60, 60] \times [-60, 60]$ with no-flux boundary conditions and the initial conditions are given by

$$u(0, r, \theta) = (1 - H_R(r))u_*, \tag{17.1a}$$

$$v(0, r, \theta) = (1 - H_R(r))v_*, \tag{17.1b}$$

$$w(0, r, \theta) = (1 - H_R(r))w_*, \tag{17.1c}$$

where u_*, v_*, and w_* are the components of the coexistence state c_{uvw} (see Section 3.2) and R is taken to be 10 (i.e., the initial patch of the coexistence state is a disc of radius 10, as shown in Figure 17.1). See Table 17.1 for the key to all 2D plots in this chapter (same as Table 10.1, but reproduced here for convenience). For all 1D plots, the usual color scheme of black for u, red for v, and green for w is employed.

Color	State
Black	Strong u Dominance
Dark Gray	Moderate u Dominance
Light Gray	Weak u Dominance
Dark Red	Strong v Dominance
Light Red	Moderate v Dominance
Orange	Weak v Dominance
Dark Green	Strong w Dominance
Light Green	Moderate w Dominance
Yellow	Weak w Dominance
White	Extinction
Magenta	Coexistence
Cyan	Other

Table 17.1. Color plot key. A species is considered to be strongly, moderately, or weakly dominant if its density is at least 0.6, 0.3, or 0.05 greater, respectively, than the densities of the other two species.

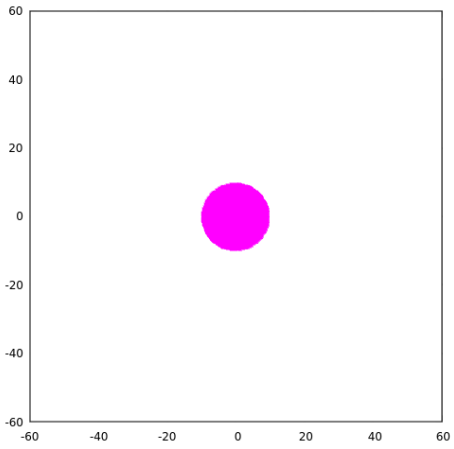

Figure 17.1. Initial conditions for all computations in this chapter. The purple disc is the coexistence state and the white region is uninhabited (see Table 17.1).

17.1. Exceptional Mobility

Consider first the case where all interaction coefficients are equal, but v is more diffusive than the other two species, as in the previous chapter. Specifically,

$$\alpha = \beta = \gamma = 4, \quad u_* = v_* = w_* = 0.2, \quad d_w = 1, \quad d_v = d. \tag{17.2}$$

In all of the computations that were run, for which d varied from 0.5 to 2, the solution approached the spatially-homogeneous heteroclinic cycle, regardless of whether $d < 1$ or $d > 1$. This also occurs when the domain is expanded to $[-360, 360] \times [-360, 360]$. The mechanism leading to this state is as follows (described for $d = 0.8$, but similar in the other cases):

(1) All three species expand outward, but u and w expand more quickly than v, due to the decreased mobility of v (Figure 17.3a). The difference in rate allows for the formation of rings dominated by a species.

(2) The species dominating the inner disc (e.g., u) is disrupted by its controlling species (v). This causes a black ring to propagate outward, while a new red inner disc is formed (the 2D analogue of patch splitting; see Figures 17.2a and 17.3b).

(3) The inner disc is next disrupted by the third species (w). A number of similar disruptions occur later on (with the disrupting species eventually traveling to the inner disc via back-diffusion; see, e.g., Figure 17.3c). After each disruption, the maximum extent of the inner disc increases (compare Figures 17.2a and 17.2b).

(4) At some point, the inner disc becomes so large that the disruptive species (e.g., v) does not travel to the center of the disc before growing substantially, creating a new black ring as before, but also creating a new red ring and leaving u temporarily in control of the inner disc (Figure 17.4a). The black inner disc, surrounded by a red ring, is overtaken by v.

(5) Subsequent patch splittings occur further outside the inner disc (Figure 17.4b). Eventually, since the domain is finite, there are no more splittings, and coarsening ensues (Figures 17.2c and 17.4c).

17.2. Exceptional Competition

Here, System (3.6) is considered with $d_v = d_w = 1$ and $\alpha = \gamma = 4$, with $\beta \neq 4$, so that v has a competitive advantage when $\beta < 4$ and a disadvantage when $\beta > 4$. For some values of β, the solution approaches the spatially-homogeneous heteroclinic cycle, as in the case of exceptional mobility (see Figure 17.5). For other values of β, spiral solutions are found (Figure 17.7). In both cases, the coexistence state initially expands to cover the domain. At this point, along the edges of the domain, the species densities are perturbed from their coexistence values, allowing for patches dominated by a single species to form (Figures 17.5a and 17.6a). In the first case (e.g., $\beta = 3.9$), coarsening decreases the spatial heterogeneity of the solution. In the second (e.g., $\beta = 3.3$), collisions of ringed structures lead to spiral structures, which appear to be stable (certainly persistent over ecologically relevant lengths of time). The time-average species fractions for the spiral solutions are qualitatively as expected (i.e., w is dominant overall, followed by v; see Section 11.2). It appears that in order to obtain a spiral solution, the difference between α and β cannot

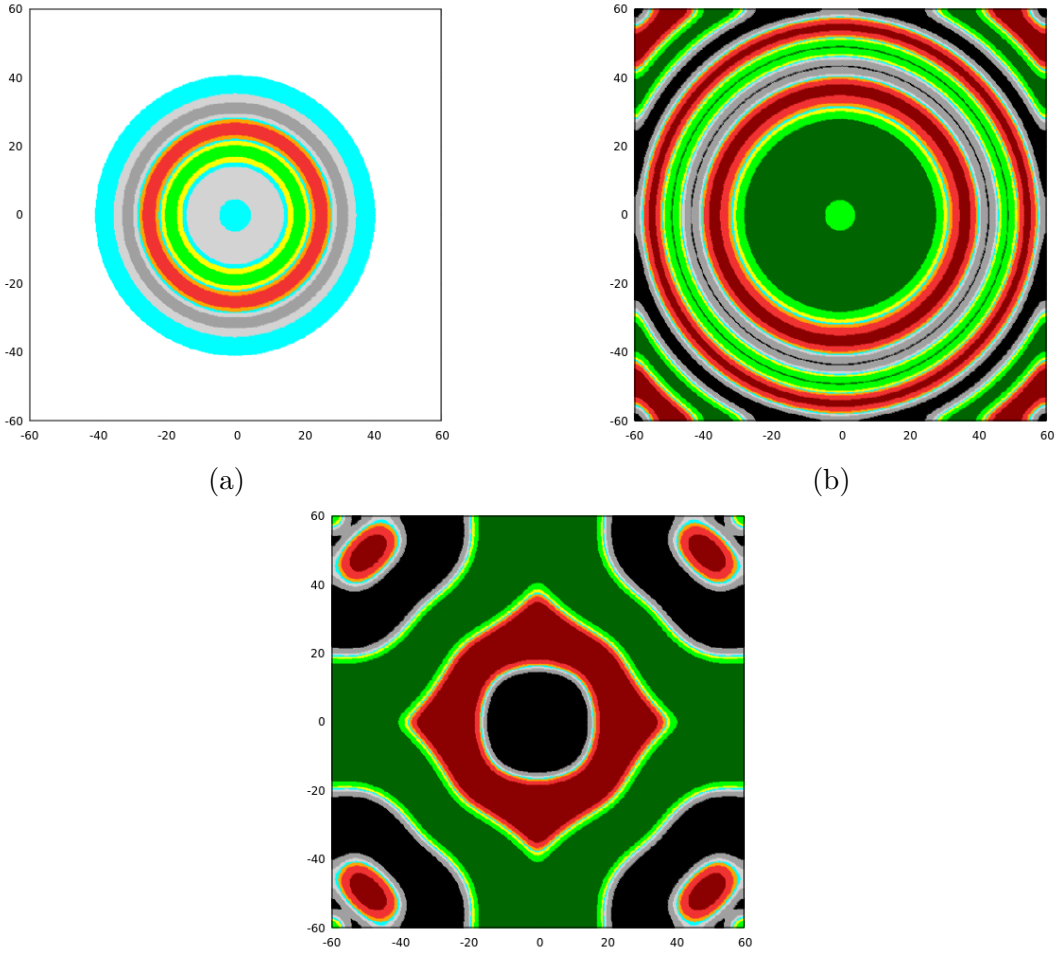

Figure 17.2. (a) Solution with $d = 0.8$ at $t = 15$. Formation of rings and first disruption of inner (gray) disc. (b) $t = 45$. (c) $t = 100$. Around the time, coarsening ensues.

be either too small or too large in magnitude, though further research is needed in this area.

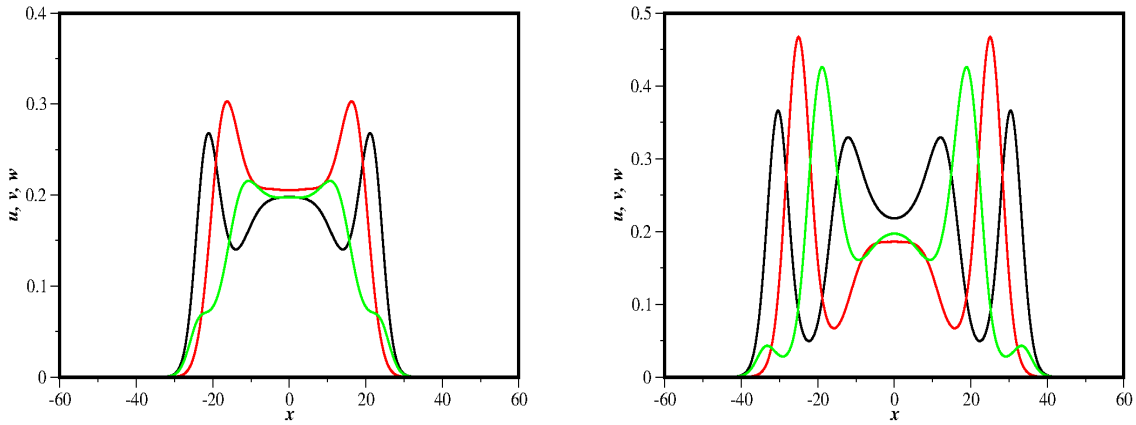

(a)

(b)

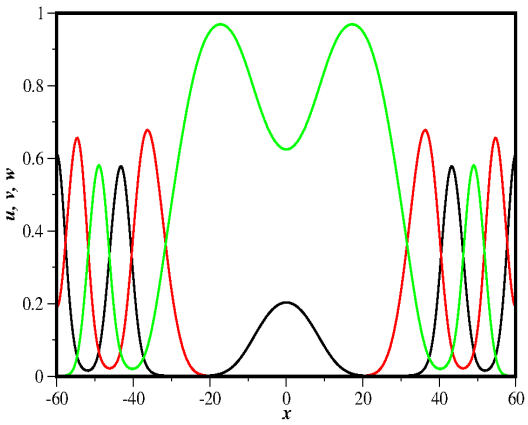

(c)

Figure 17.3. (a) Solution along x-axis with $d = 0.8$ showing the formation of rings ($t = 10$). (b) Disruption of inner disc by v ($t = 15$). (c) Disruption of inner disc by u following back-diffusion of u ($t = 45$).

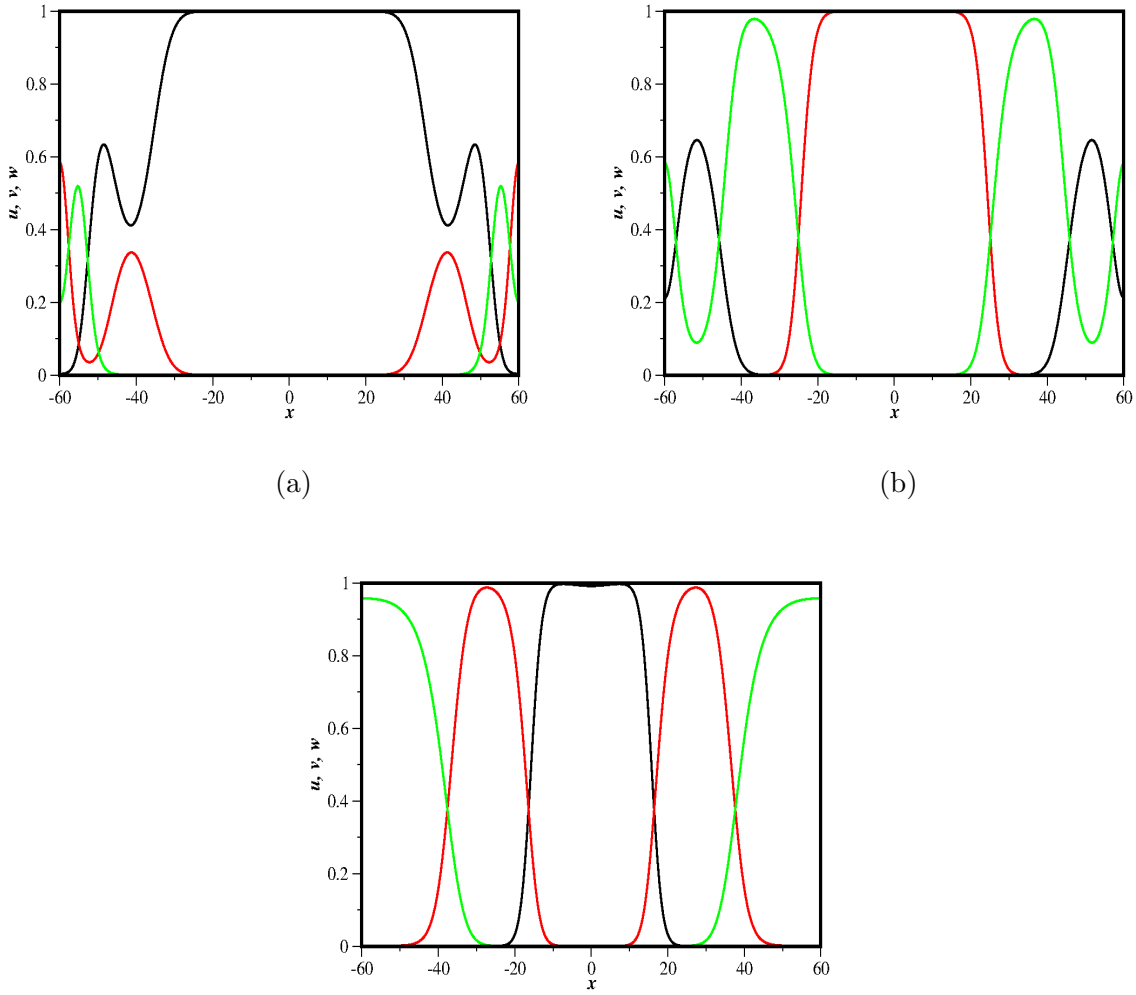

(a) (b)

(c)

Figure 17.4. (a) Solution along x-axis with $d = 0.8$ showing disruption away from the center of the inner disc by v ($t = 60$). (b) Disruption by u outside inner disc ($t = 75$). (c) Solution near the point where disruptions cease ($t = 100$).

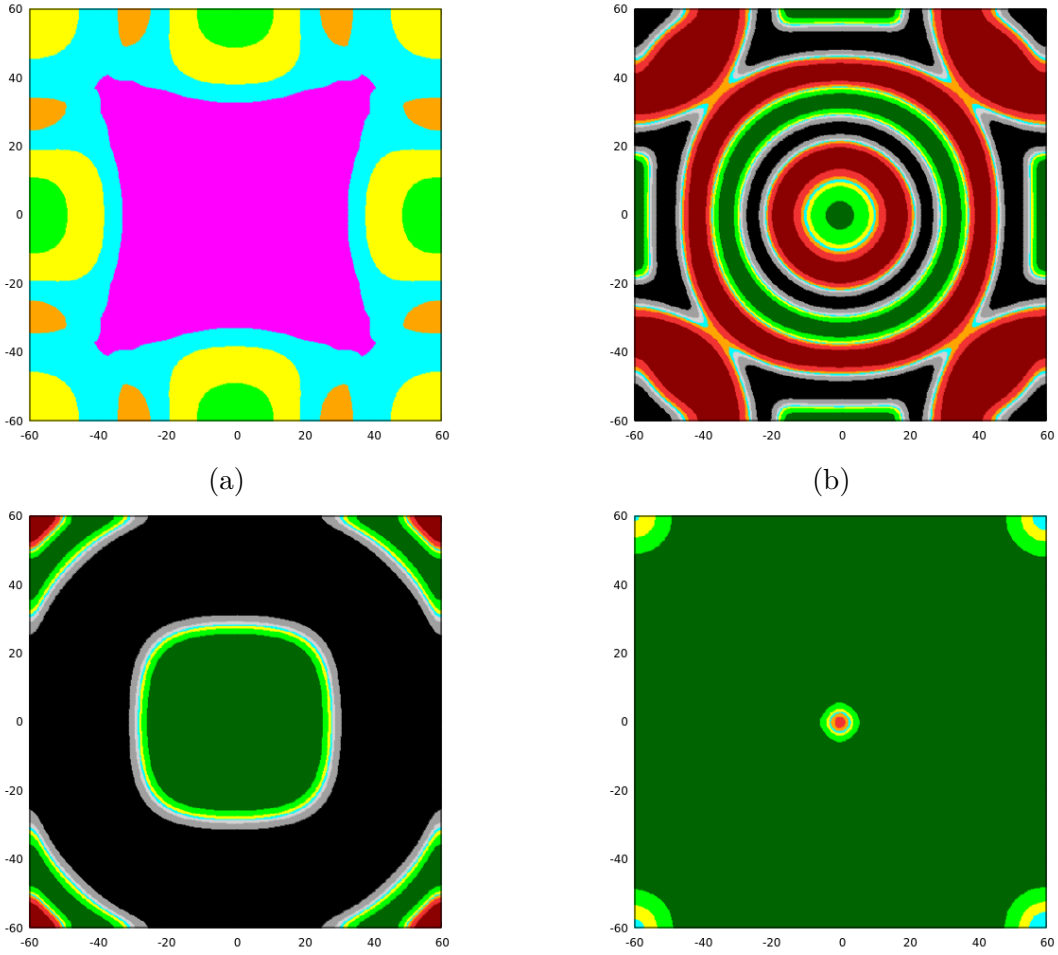

Figure 17.5. (a) Solution with $\beta = 3.9$ at $t = 100$. (b) $t = 150$. (c) $t = 200$. (d) $t = 250$, where the solution is approaching spatial homogeneity.

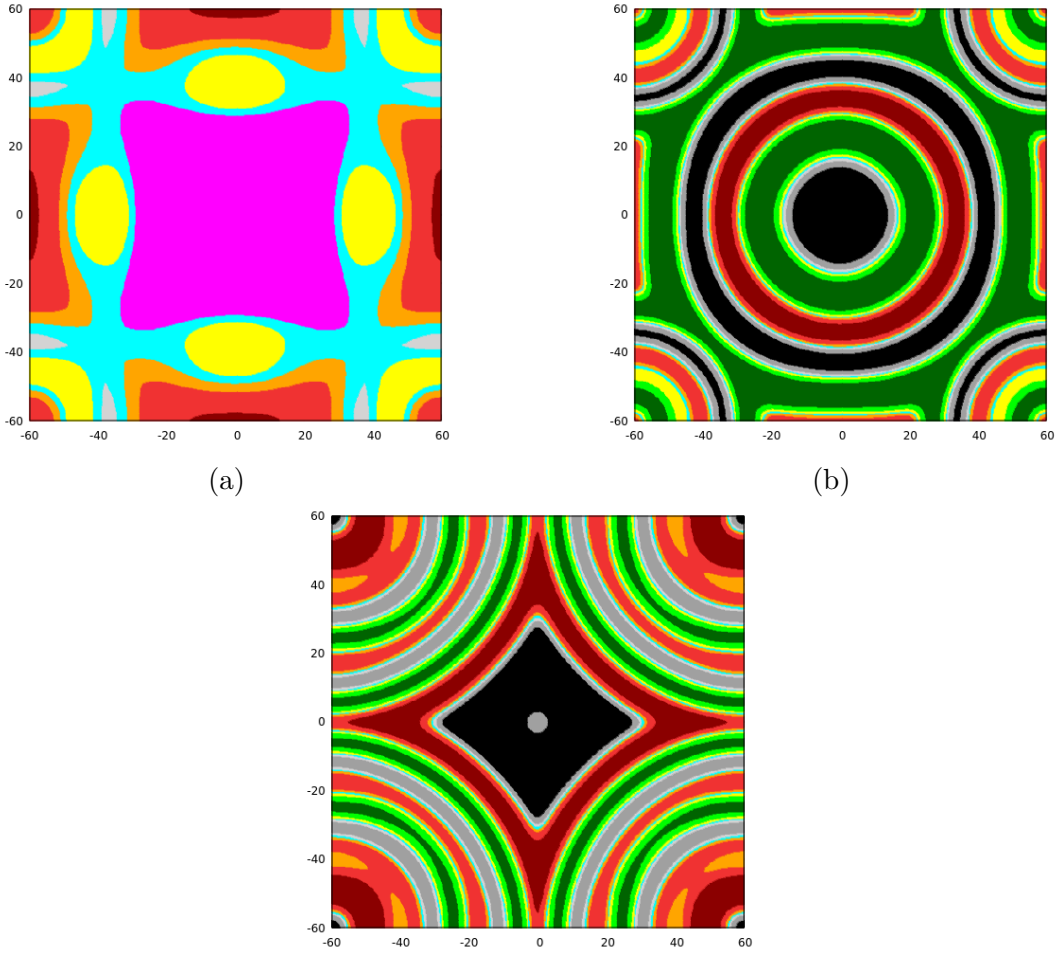

(a) (b)

(c)

Figure 17.6. (a) Solution with $\beta = 3.3$ (eventually a spiral solution) at $t = 100$. (b) $t = 150$. (c) $t = 200$.

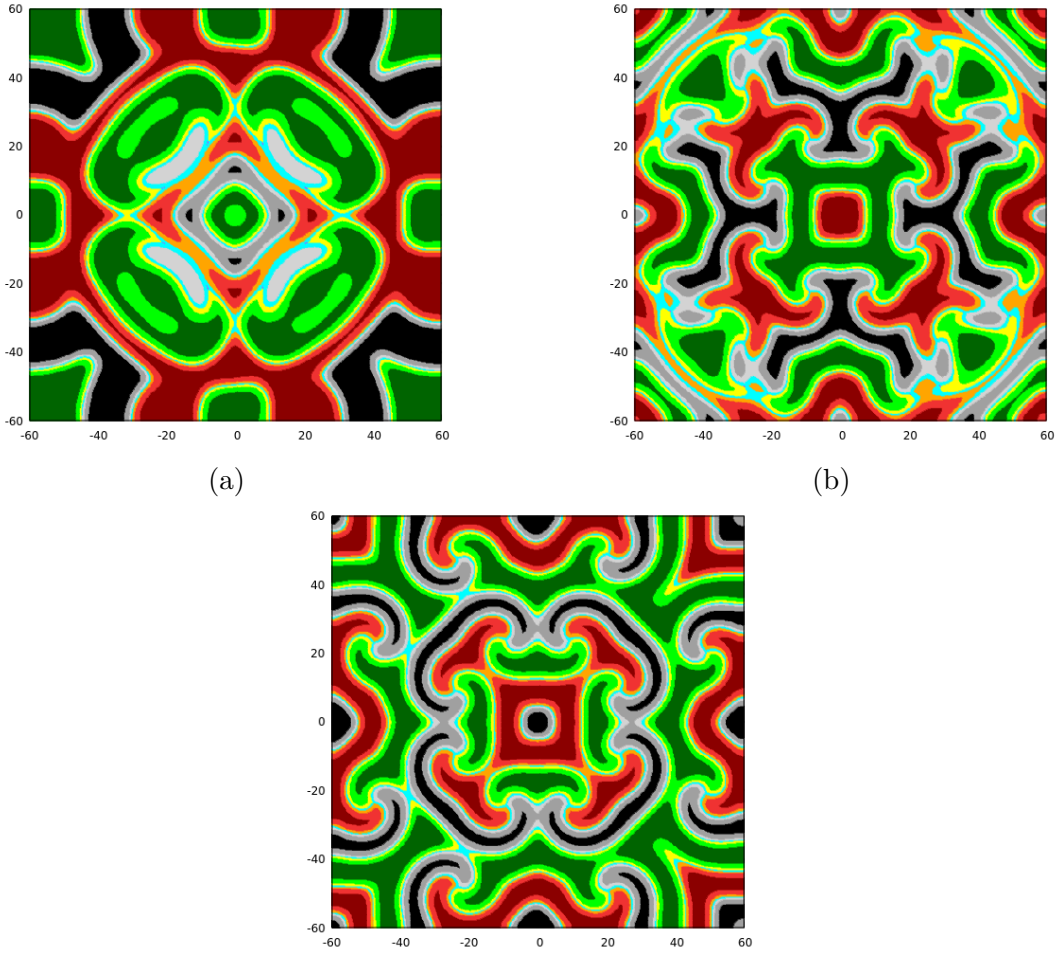

(a) (b)

(c)

Figure 17.7. (a) Solution with $\beta = 3.3$ at $t = 250$. (b) $t = 350$, where spiral structures are beginning to form. (c) $t = 600$, where clear, persistent spirals are present.

CHAPTER 18

Discussion and Conclusions

Cyclic ecosystems can be modeled by systems of reaction-diffusion partial differential equations. As demonstrated above, a number of interesting spatiotemporal patterns can arise in the solutions to these systems and the dominant species is not always obvious. Direct interspecies competition, mobility, and positioning all play a role in the dynamics of cyclic systems, even in a qualitative sense.

In two-species systems, one species can kill off the other, the species can coexist, or the species can exist in separate colonies. A disadvantage in mobility can be offset by a positional or direct competitive advantage, while a disadvantage in direct competition can be offset by a positional or mobility advantage and a positional disadvantage can be offset by a mobility or direct competitive advantage. On two-dimensional domains, positional advantages can be due to curvature in species-species interfaces. Parts of an interface with negative curvature (with respect to the direction of propagation) will travel more quickly than those with zero or positive curvature (Chapter 6).

In three-species systems, a number of solution types are possible. For symmetric systems (i.e., systems in which all species have identical properties) with strong interspecies competition (so that coexistence is unstable) and spatially-inhomogeneous initial conditions, chaotic solutions predominate when interspecies competition is relatively weak. In contrast, when interspecies competition is sufficiently strong, ordered solutions are generally found. Whether or not a solution to the PDE problem will be ordered can often

be predicted from the solution to the associated ODE problem with appropriate initial conditions (Chapter 9).

One-dimensional ordered states generally involve single-species patches propagating via diffusion. Such states can involve rigidly-propagating arrays of patches (traveling waves) or breathers, in which individual patches periodically expand and contract (modulated traveling waves). The patches in rigidly-propagating arrays can all have the same width (symmetric traveling waves, arising from symmetric or near-symmetric initial conditions) or not (pseudo asymmetric traveling waves). For symmetric traveling waves and breathers, each species is, on average, distributed equally throughout the domain. This is obviously not true for asymmetric patch traveling waves, in which a dominant species is determined by the initial conditions.

Chaotic solutions still exhibit some facets of order. Additional clusters of each species arise via patch splitting, which has been shown to be a mechanism for the development of the spatiotemporal chaos. Once generated, these clusters propagate according to the RPS relationships, with clusters of a species chasing clusters of its victim species. Furthermore, in at least some cases, the chaos is only transient. Coarsening occurs when a cluster is surrounded by controlling clusters and is subsequently eliminated from the system. In these cases, spatial heterogeneity can ultimately be lost, leading to a spatially-homogeneous heteroclinic cycle (Chapter 8).

Ordered states on two-dimensional domains generally contain spirals or fluid single-species patches chasing patches of their victim species. In particular, spirals are very prevalent when interspecies competition is strong. All ordered states in one and two

dimensions that have been found involve a large degree of self-segregation of the species (Chapter 10).

Although the parameters of the PDE systems were chosen to be in line with experimental ecosystems consisting of variants of *E. coli*, not all of the spatiotemporal patterns found in solutions to the two-dimensional PDE system have been observed experimentally. In particular, neither chaos nor spiral patterns have been reported in the ecological literature. This could be for a number of reasons:

(1) The deterministic models used here do not account for stochastic effects. The spiral solutions described here, however, are quite robust to additive noise (and chaotic solutions subjected to noise are generally still chaotic), so it is unlikely that this is a significant factor.

(2) The species involved in an ecosystem generally do not have identical properties, so a symmetric system of PDEs is unrealistic to some extent. While this is true, spirals and chaos can still occur when the symmetry of the system is broken (Chapter 11).

(3) The model only permits purely cyclic interspecies competition (i.e., some sources of competition are neglected). In a physical ecosystem, all species generally compete with each other to some extent. It could be argued that neglecting these small competition terms could lead to substantial qualitative differences in the dynamics. It turns out, however, that both chaos and spiral solutions are readily found in models that do consider these extra terms (see, e.g., [**37**]).

(4) It is difficult to see such detailed spatial patterns experimentally. For example, in the static plate experiment discussed in [**3**], the dominant species at various

spatial locations, rather than the relative concentrations of all the species, was determined. Thus, chaotic dynamics could not possibly be observed. Moreover, experiments may not be run long enough to see clear steady-state behavior. It should also be noted that the main goals of the ecological literature do not usually include pattern recognition.

(5) The strength of interspecies competition or initial conditions in experiments may not be conducive to these behaviors.

Nevertheless, many reported behaviors are captured by the model, including single-species patches chasing other patches, approaches to spatial homogeneity, cycles of dominance in spatially-homogeneous ecosystems, and speeds of propagation (including positional advantages). The model also predicts that the controlling species of an ostensibly dominant species in an asymmetric system is often the true overall dominant species, as observed in systems of *E. coli* [**58**] (Chapter 11).

The predominant feature of three- and four-species models with an exceptionally competitive (or uncompetitive) species is the prevalence of partial alliances (two-species alliances for three-species systems and three-species alliances for four-species systems) that exclude the most vulnerable species. These partial alliances transition to full coexistence when the system parameters are such that the most vulnerable species is strong enough to coexist with the others. The transition is via a transcritical bifurcation where the partial alliances lose stability to the appropriate coexistence state.

The exceptional species regime was studied in the context of the invasion problem, where a partial alliance displaces other (generally unstable) states such as single-species states. When the partial alliance states are unstable, the stable coexistence state forms

and displaces all unstable states (though perhaps not directly). Speeds associated with these displacements were computed and shown to agree with speeds expected for pulled fronts.

In many instances, the coexistence state does not directly displace other states; instead, a complex intermediate region forms between the advancing and retreating states. For three-species systems, the displacement is characterized by ripples of individual species being drawn out of the coexistence mixture. In this case, the solution is a non-monotone rigidly-propagating traveling wave. For four-species systems, there is also a complex interface between the advancing and retreating states, but in this case, intermediate buffer states can form. When this occurs, there may not be a traveling wave; rather, the buffer state will continually expand due to a mismatch between the speed of its leading edge and its trailing edge.

Solutions of the three- and four-species models in the regime where all species are strong competitors show very different behaviors. For the three-species model, the behavior is dominated by complex (possibly chaotic) dynamics (Chapters 7 - 10), whereas for the four-species model, the behavior is dominated by stable alliances of noncompeting species (see [**20**] and Section 6.1.3). In contrast, solution behaviors in the exceptional species regime show unity between the two models.

Additionally, one-dimensional three-species systems in which a species is exceptionally mobile can have a variety of types of solutions. Chaos can occur, as can steady-state patch splitting and asymmetric traveling waves. In general, as the exceptional diffusivity decreases from 1, the dynamics of the system become more complicated (Chapter 16).

In two dimensions with an initial disc of the coexistence state surrounded by uninhabited space, the presence of an exceptionally mobile species leads a spatially-homogeneous heteroclinic cycle. On the other hand, the presence of an exceptionally competitive or uncompetitive species often leads to a spatially-homogeneous heteroclinic cycle, but it can, in some parameter regimes, lead to a persistent spiral pattern (Chapter 17).

References

[1] Carrie Arnold. Biodiversity may thrive through games of rock-paper-scissors. *Quantamagazine*, 2020.

[2] J. E. Cronan. *Escherichia coli as an Experimental Organism*. John Wiley & Sons, Ltd, 2014.

[3] B. Kerr, M. A. Riley, M. W. Feldman, and B. J. M. Bohannan. Local dispersal promotes biodiversity in a real-life game of rock-paper-scissors. *Nature*, 418:171–173, 2002.

[4] B. C. Kirkup and M. A. Riley. Antibiotic-mediated antagonism leads to bacterial game of rock-paper-scissors in vivo. *Nature*, 428:412–414, 2004.

[5] M. F. Weber, G. Poxleitner, E. Hebisch, E. Frey, and M. Opitz. Chemical warfare and survival strategies in bacterial range expansions. *J. R. Soc. Interface*, 11(96):20140172, 2014.

[6] M. J. Liao, M. O. Din, L. Tsimring, and J. Hasty. Rock-paper-scissors: Engineered population dynamics increase genetic stability. *Science*, 365(6457):1045–1049, 2019.

[7] B. Sinervo and C. M. Lively. The rock-paper-scissors game and the evolution of alternative male strategies. *Nature*, 380:240–243, 1996.

[8] J. B. C. Jackson and L. E. O. Buss. Alleopathy and spatial competition among coral reef invertebrates. *Proc. Natl. Acad. Sci. U.S.A.*, 72:5160–5163, 1975.

[9] T. E. Thorhallsdottir. The dynamics of five grasses and white clover in a simulated mosaic sward. *J. Ecol.*, 78(4):909–923, 1990.

[10] E. J. P. Marshall. Interference between sown grasses and the growth of rhizome of *elymus repens* (couch grass). *Agric. Ecosyst. Environ.*, 33:11–22, 1990.

[11] R. M. May and W. J. Leonard. Nonlinear aspects of competition between three species. *SIAM J. Appl. Math.*, 29:243–253, 1975.

[12] B. Gibson, D. J. Wilson, E. Feil, and A. Eyre-Walker. The distribution of bacterial doubling times in the wild. *Proc. Biol. Sci.*, 285(1880):20180789, 2018.

[13] H. C. Berg and L. Turner. Chemotaxis of bacteria in glass capillary arrays. *Biophys J.*, 58(4):919–30, 1990.

[14] M. Wu, J. W. Roberts, S. Kim, D. L. Koch, and M. P. DeLisa. Collective bacterial dynamics revealed using a three-dimensional poplation-scale defocused particle tracking technique. *Appl. Environ. Microbiol.*, 72(7):4987–4994, 2006.

[15] O. A. Croze, G. P. Ferguson, M. E. Cates, and W. C. K. Poon. Migration of chemotactic bacteria in soft agar: role of gel concentration. *Biophys. J*, 101(3):525–534, 2011.

[16] A. Bayliss, A. A. Nepomnyashchy, and V. A. Volpert. Mathematical modeling of cyclic population dynamics. *Physica D*, 394:56–78, 2019.

[17] Z. Wang, A. Bayliss, and V. A. Volpert. Asymptotic analysis of the bistable Lotka-Volterra competition-diffusion system. *Applied Mathematics and Computation*, 432:127371, 2022.

[18] V. S. Afraimovich, M. I. Rabinovich, and P. Varona. Heteroclinic contours in neural ensembles and the winnerless competition principle. *Int. J. Bifurcat. Chaos*, 14(04):1195–1208, 2004.

[19] Y. A. Kuznetsov. *Elements of applied bifurcation theory*, volume 112 of *Applied Mathematical Sciences*. Springer Science & Business Media, 2013.

[20] A. Bayliss, A.A. Nepomnyashchy, and V. A. Volpert. Beyond rock–paper–scissors systems — deterministic models of cyclic ecological systems with more than three species. *Physica D*, 411:132585, 2020.

[21] P. K. Brazhnik and J. J. Tyson. On traveling wave solutions of Fisher's equation in two spatial dimensions. *SIAM J. Appl. Math.*, 60(2):371–391, 1999-2000.

[22] J. D. Murray. *Mathematical Biology*. New York: Springer, 3rd edition, 2002.

[23] V. Volpert and S. Petrovskii. Reaction-diffusion waves in biology. *Phys. Life Rev.*, 6(4):267–310, 2009.

[24] P. R. Buenzli and M. J. Simpson. Curvature dependences of wave propagation in reaction-diffusion models. *arXiv preprint arXiv:2112.00928v1*, 2021.

[25] J. J. Tyson and J. P. Keener. Singular perturbation theory of traveling waves in excitable media (a review). *Physica D*, 32:327–361, 1988.

[26] W. Van Saarloos. Front propagation into unstable states. *Physics reports*, 386:29–222, 2003.

[27] A. Bayliss and V. A. Volpert. Complex predator invasion waves in a Holling-Tanner model with nonlocal nonlocal prey interaction. *Physica D*, 346:37–58, 2017.

[28] J. W. Cooley and J. W. Tukey. An algorithm for the machine calculation of complex fourier series. *Math. Comput.*, 19:297–301, 1965.

[29] M. Frigo and S. Johnson. The design and implementation of FFTW3. *Proc. IEEE*, 93(2):216–231, 2005.

[30] A. Roman, D. Konrad, and M. Pleimling. Cyclic competition of four species: domins and interfaces. *J. Stat. Mech.*, page 07014, 2012.

[31] M. P. O. Loureiro, J. J. Arenzon, L. F. Cugliandolo, and A. Sicilia. Curvature-driven coarsening in the two-dimensional potts model. *Phys. Rev. E*, 81:021129, 2010.

[32] T. I. Stiadle, A. Bayliss, and V. A. Volpert. Order and disorder in a cyclically competitive ecological community. *SIAM J. Appl. Dyn. Syst.*, page (in press).

[33] R. Yang, W.-X. Wang, Y.-C. Lai, and C. Grebogi. Role of intraspecific competition in the coexistence of mobile populations in spatially extended ecosystems. *Chaos*, 20(2):023113, 2010.

[34] W.-Xu Wang, X. Ni, Y.-C. Lai, and C. Grebogi. Pattern formation, synchronization, and outbreak of biodiversity in cyclically competing games. *Phys. Rev. E*, 83:011917, 2011.

[35] T. Reichenbach, M. Mobilia, and E. Frey. Mobility promotes and jeopardizes biodiversity in rock–paper–scissors games. *Nature*, 448(7157):1046–1049, 2007.

[36] X. Ni, W.-X. Wang, Y.-C. Lai, and C. Grebogi. Cyclic competition of mobile species on continuous space: Pattern formation and coexistence. *Phys. Rev. E*, 82:066211, 2010.

[37] C. M. Postlethwaite and A. M. Rucklidge. Spirals and heteroclinic cycles in a spatially extended rock-paper-scissors model of cyclic dominance. *Europhys. Lett.*, 117(4):48006, 2017.

[38] C. M. Postlethwaite and A. M. Rucklidge. A trio of heteroclinic bifurcations arising from a model of spatially-extended rock-paper-scissors. *Nonlinearity*, 32(4):1375–1407, mar 2019.

[39] A. Cangiani, E. H. Georgoulis, A. Yu. Morozov, and O. J. Sutton. Revealing new dynamical patterns in a reaction-diffusion model with cyclic competition via a novel computational framework. *Proc. Royal Soc. A*, 474, 2018.

[40] L. Contento and M. Mimura. Complex pattern formation driven by the interaction of stable fronts in a competition-diffusion system. *J. Math. Biol.*, 80:303–342, 2020.

[41] S. Petrovskii, K. Kawasaki, F. Takasu, and N. Shigesada. Diffusive waves, dynamical stabilization and spatio-temporal chaos in a community of three competitive species. *Jpn. J. Ind. Appl. Math.*, 18(2):459–481, 2001.

[42] K. Manna, V. Volpert, and M. Banerjee. Pattern formation in a three-species cyclic competition model. *Bull. Math. Biol.*, 83(5):1–35, 2021.

[43] K. Orihashi and A. Yoji. Global aspects of turbulence induced by heteroclinic cycles in competitive diffusion Lotka-Volterra equation. *Physica D*, 240(23):1853–1862, 2011.

[44] S. Petrovskii and H. Li, B.-L.and Malchow. Quantification of the spatial aspect of chaotic dynamics in biological and chemical systems. *Bull. Math. Biol.*, 65(3):425–446, 2003.

[45] H. Malchow, S. V. Petrovskii, and E. Venturino. *Spatiotemporal patterns in ecology and epidemiology: theory, models, and simulation*. CRC Press, 2007.

[46] C. R. Hasan, H. M. Osinga, C. M. Postlethwaite, and A. M. Rucklidge. Spatiotemporal stability of periodic travelling waves in a heteroclinic-cycle model. *Nonlinearity*, 34(8):5576, 2021.

[47] F. H. Busse and K. E. Heikes. Convection in a rotating layer: a simple case of turbulence. *Science*, 208(4440):173–175, 1980.

[48] E. Stone and P. Holmes. Random perturbations of heteroclinic attractors. *SIAM J. Appl. Math.*, 50(3):726–743, 1990.

[49] E. Stone and D. Armbruster. Noise and O(1) amplitude effects on heteroclinic cycles. *Chaos*, 9(2):499–506, 1999.

[50] R. A. Edson, J. E. Bunder, T. W. Mattner, and A. J. Roberts. Lyapunov exponents of the Kuramoto–Sivashinsky PDE. *ANZIAM J.*, 61:270–285, 2019.

[51] J. P. Keener and J. J. Tyson. Spiral waves in the Belousov-Zhabotinskii reaction. *Physica. D*, 21(2):307–324, 1986.

[52] A. T. Winfree. Varieties of spiral wave behavior: An experimentalist's approach to the theory of excitable media. *Chaos*, 1(3):303–334, 1991.

[53] S. I. Ei, R. Ikota, and M Mimura. Segregating partition problem in competition-diffusion systems. *Interfaces Free Bound*, 1(1):57–80, 1999.

[54] C. R. Hasan, H. M. Osinga, C. M. Postlethwaite, and A. M. Rucklidge. Numerical continuation of spiral waves in heteroclinic networks of cyclic dominance. *arXiv preprint arXiv:2010.05224*, 2020.

[55] Y. Gong and D. J. Christini. Antispiral waves in reaction-diffusion systems. *Phys. Rev. Lett.*, 90(8):088302, 2003.

[56] B. Szczesny, M. Mobilia, and A. M. Rucklidge. When does cyclic dominance lead to stable spiral waves? *Europhys. Lett.*, 102(2):28012, 2013.

[57] M. Frean and E. R. Abraham. Rock-scissors-paper and the survival of the weakest. *Proc. Royal Soc. B*, 268(1474):1323–1327, 2001.

[58] M. J. Liao, A. Miano, C. B. Nguyen, L. Chao, and J. Hasty. Survival of the weakest in non-transitive asymmetric interactions among strains of *e. coli*. *Nat. Comm.*, 11, 2020.

[59] M. Perc, A. Szolnoki, and G. Szabó. Cyclic interactions with alliance-specific heterogeneous invasion rates. *Phys. Rev. E*, 75:052102, 2007.

[60] C. A. Glass and D. H. Glass. Social influence of competing groups and leaders in opinion dynamics. *Comput. Econ.*, 58:799–823, 2020.

[61] Karmeshu and R. K. Pathria. Stochastic evolution of competing social groups. *J. Math. Sociol.*, 7(1):47–58, 1980.

[62] M. C. Griebeler and R. C. Resende. A model of electoral alliances in highly fragmented party systems. *J. Theor. Politics*, 33(1):3–24, 2021.

[63] A. Szolnoki and Bazeia D. de Oliveira, B. F. Pattern formations driven by cyclic interactions: A brief review of recent developments. *EPL*, 131(6):68001, 2020.

[64] B. F. de Oliveira and A. Szolnoki. Competition among alliances of different sizes. *Chaos Solit. Fractals*, 157:111940, 2022.

[65] A. Szolnoki, M. Mobilia, L.-L. Jiang, B. Szczesny, A.M. Rucklidge, and M. Perc. Cyclic dominance in evolutionary games: a review. *J. R. Soc. Interface*, 11:0735, 2014.

[66] U. Dobramysl, M. Mobilia, M. Pleimling, and U. C. Täuber. Stochastic population dynamics in spatially extended predator-prey systems. *J. Phys. A*, 51:063001, 2018.

[67] J. Canosa. On a nonlinear diffusion equation describing population growth. *IBM J. Res. Dev.*, 17:307–313, 1973.

[68] M. A. Lewis, S. V. Petrovskii, and J. R. Potts. *The Mathematics Behind Biological Invasions*, volume 44 of *Interdisciplinary Applied Mathematics*. Springer, 2016.

[69] H. Malchow and S. V. Petrovskii. Dynamical stabilization of an unstable equilibrium in chemical and biological systems. *Math. Comput. Model.*, 36(3):307–319, 2002.

APPENDIX A

Stability of Coexistence State of Three-Species System

Using the relationships (3.11), the Jacobian matrix of System (3.7) evaluated at the point (u_*, v_*, w_*) simplifies to

$$J = \begin{pmatrix} -u_* & -\alpha u_* & 0 \\ 0 & -v_* & -\beta v_* \\ -\gamma w_* & 0 & -w_* \end{pmatrix}. \tag{A.1}$$

The characteristic polynomial of J is

$$P(\lambda) = -(\lambda^3 + (u_* + v_* + w_* - 1)\lambda^2 + (u_*v_* + u_*w_* + v_*w_*)\lambda + (1 - \alpha\beta\gamma)u_*v_*w_*, \tag{A.2}$$

which has a factor of $(\lambda + 1)$ and can thus be rewritten as

$$P(\lambda) = -(\lambda + 1)[\lambda^2 + (u_* + v_* + w_* - 1)\lambda + (\alpha\beta\gamma + 1)u_*v_*w_*]. \tag{A.3}$$

The remaining two eigenvalues λ_2 and λ_3 (recall that one eigenvalue is $\lambda_1 = -1$) can be found via the quadratic formula to be

$$\lambda_{2,3} = \frac{1}{2}\left(1 - u_* - v_* - w_* \pm \sqrt{(u_* + v_* + w_* - 1)^2 - 4(\alpha\beta\gamma + 1)u_*v_*w_*}\right). \tag{A.4}$$

Since $\alpha, \beta, \gamma, u_*, v_*, w_* > 0$, it is clear that

$$\sqrt{(u_* + v_* + w_* - 1)^2 - 4(\alpha\beta\gamma + 1)u_* v_* w_*} < \sqrt{(u_* + v_* + w_* - 1)^2} = |1 - u_* - v_* - w_*|, \tag{A.5}$$

so that $\lambda_2 < 0$ and $\lambda_3 < 0$ if and only if $u_* + v_* + w_* > 1$. Thus, the coexistence state is stable if and only if

$$u_* + v_* + w_* > 1. \tag{A.6}$$

APPENDIX B

Estimated Propagation Speeds of Pulled Fronts

Here, propagation speeds of pulled fronts are estimated via the method described in Section 4.2.1. In these cases, all diffusivities are assumed to be 1, so that the diagonal matrix D is just the identity matrix I.

B.1. Displacement of Unstable c_{uw} State by c_{uvw}

Let $\alpha < 1$ and $1 < \beta < \frac{1}{1-\alpha}$, so that the c_{uw} state is physical, but unstable, and the c_{uvw} state is physical and stable. The Jacobian matrix of System (12.1) evaluated for the c_{uw} state is

$$J = \begin{pmatrix} -1 & -\alpha & 0 \\ 0 & 1+\beta(\alpha-1) & 0 \\ \alpha(\alpha-1) & 0 & \alpha-1 \end{pmatrix}. \tag{B.1}$$

Thus, the matrix $k^2D + J$ has eigenvalues $k^2 - 1$, $k^2 + 1 + \beta(\alpha - 1)$, and $k^2 + \alpha - 1$. Of these, only the eigenvalue $k^2 + 1 + \beta(\alpha - 1)$ is always positive in the regime of interest. Thus, $\Lambda = k^2 + 1 + \beta(\alpha - 1)$ so that

$$\begin{aligned} s(k) &= \frac{\Lambda}{k} = k + \frac{1+\beta(\alpha-1)}{k} \\ \implies s'(k) &= 1 - \frac{1+\beta(\alpha-1)}{k^2}. \end{aligned} \tag{B.2}$$

Setting $s'(k) = 0$ and solving for k gives $k = \sqrt{1 + \beta(\alpha - 1)}$, so that the minimum speed is $s_{min} = 2\sqrt{1 + \beta(\alpha - 1)}$ (see Section 14.1). This is the speed that is expected for a sufficiently steep interface, as discussed in Section 4.2.1.

B.2. Displacement of Unstable e_{vwz} State by e_{uwz}

Let $\alpha < 1$ and $1 < \beta < \frac{1}{1-\alpha+\alpha^2}$, so that the e_{vwz} state is physical, but unstable, and the e_{uwz} state is physical and stable. The Jacobian matrix of System (12.2) evaluated for the e_{vwz} state is

$$J = \begin{pmatrix} (1-\alpha)(1+\alpha\beta) & 0 & 0 & 0 \\ 0 & \beta(1-\alpha)-1 & \beta((1-\alpha)\beta-1) & 0 \\ 0 & 0 & \alpha-1 & \alpha(\alpha-1) \\ -\alpha & 0 & 0 & -1 \end{pmatrix}. \tag{B.3}$$

Thus, the matrix k^2D+J has eigenvalues $k^2+(1-\alpha)(1+\alpha\beta)$, $k^2+\beta(1-\alpha)-1$, $k^2+\alpha-1$, and k^2-1. Of these, only the eigenvalue $k^2 + (1-\alpha)(1+\alpha\beta)$ is always positive in the regime of interest. Thus, $\Lambda = k^2 + (1-\alpha)(1+\alpha\beta)$ so that

$$s(k) = \frac{\Lambda}{k} = k + \frac{(1-\alpha)(1+\alpha\beta)}{k}. \tag{B.4}$$

The minimum of $s(k)$ occurs at $k = \sqrt{(1-\alpha)(1+\alpha\beta)}$, which gives $s_{min} = 2\sqrt{(1-\alpha)(1+\alpha\beta)}$ (see Section 15.1).

B.3. Displacement of Unstable e_{vz} State by e_{uwz}

Let $\alpha < 1$ and $1 < \beta < \frac{1}{1-\alpha+\alpha^2}$, so that the e_{vz} state is unstable and the e_{uwz} state is physical and stable. The Jacobian matrix of System (12.2) evaluated for the e_{vz} state is

$$J = \begin{pmatrix} 1-\alpha & 0 & 0 & 0 \\ 0 & -1 & -\beta & 0 \\ 0 & 0 & 1-\alpha & 0 \\ -\alpha & 0 & 0 & -1 \end{pmatrix}. \tag{B.5}$$

Thus, the matrix k^2D+J has eigenvalues $k^2+1-\alpha$ (repeated) and k^2-1 (also repeated). In the regime of interest, $k^2+1-\alpha$ is always positive. Thus, $\Lambda = k^2+1-\alpha$ so that

$$s(k) = \frac{\Lambda}{k} = k + \frac{1-\alpha}{k}. \tag{B.6}$$

The minimum of $s(k)$ occurs at $k = \sqrt{1-\alpha}$, which gives
$s_{min} = 2\sqrt{1-\alpha}$ (see Section 15.1).

B.4. Displacement of Unstable e_{uw} State

Let $\beta < 1$, so that the e_{uw} state is unstable. The Jacobian matrix of System (12.2) evaluated for the d_{uw} state is

$$J = \begin{pmatrix} -1 & -\alpha & 0 & 0 \\ 0 & 1-\beta & 0 & 0 \\ 0 & 0 & -1 & -\alpha \\ 0 & 0 & 0 & 1-\alpha \end{pmatrix}. \tag{B.7}$$

Thus, the matrix $k^2D + J$ has eigenvalues $k^2 - 1$ (repeated), $k^2 + 1 - \beta$, and $k^2 + 1 - \alpha$. In the regime of interest, $k^2 + 1 - \beta$ is always positive. Thus, $\Lambda = k^2 + 1 - \beta$ so that

$$s(k) = \frac{\Lambda}{k} = k + \frac{1-\beta}{k}. \tag{B.8}$$

The minimum of $s(k)$ occurs at $k = \sqrt{1-\beta}$, which gives $s_{min} = 2\sqrt{1-\beta}$, regardless of the displacing state (e.g., e_{uvw} or e_{vz}; see Section 15.1).

Vita

Thomas Isaac Stiadle was born in Ithaca, NY on June 20, 1996. He grew up in King Ferry, NY and graduated from Southern Cayuga High School in 2014. He attended Case Western Reserve University, from which he graduated *summa cum laude* with a B.S. in Chemistry and a B.S. in Mathematics in 2018. He subsequently enrolled at Northwestern University, where he earned an M.S. (2019) and a Ph.D. (2022) in Applied Mathematics.

Works:

M. Linetsky, K. S. Bondelid, S. Losovskiy, V. Gabyak, M. J. Rullo, T. I. Stiadle, V. Munjapara, P. Saxena, D. Ma, Y.-S. Cheng, A. M. Howes, E. Udeigwe, and R. G. Salomon. 4-Hydroxy-7-oxo-5-heptenoic acid lactone is a potent inducer of the complement pathway in human retinal pigmented epithelial cells. *Chem. Res. Toxicol.*, 31(8):666-679, 2018.

T. I. Stiadle, A. Bayliss, and V. A. Volpert. Order and disorder in a cyclically competitive ecological community. *SIAM J. Appl. Dyn. Syst.* (in press).

T. I. Stiadle, A. Bayliss, and V. A. Volpert. Cyclic ecological systems with an exceptional species. *Appl. Math. Comput.* (in review).